UNIVERSITY OF OKLAHOMA

GRADUATE COLLEGE

MODULATING LATTICE OXYGEN ACTIVITY OF $CA_2FE_{2-x}M_xO_5$ BROWNMILLERITE FOR PRODUCTION OF HIGH PURITY HYDROGEN FROM BIOMASS RESOURCES

A THESIS

SUBMITTED TO THE GRADUATE FACULTY

in partial fulfillment of the requirements for the

Degree of

MASTER OF SCIENCE

By

TENZIN DAWA
Norman, Oklahoma
2024

Downloaded from SHAREOK. Persistent Handle URL: https://hdl.handle.net/11244/340315

MODULATING LATTICE OXYGEN ACTIVITY OF $CA_2FE_{2-x}M_xO_5$ BROWNMILLERITE FOR PRODUCTION OF HIGH PURITY HYDROGEN FROM BIOMASS RESOURCES

A THESIS APPROVED FOR THE
MEWBOURNE SCHOOL OF PETROLEUM AND GEOLOGICAL ENGINEERING

BY THE COMMITTEE CONSISTING OF

Dr. Baharak Sajjadi, Chair

Dr. Deepak Devegowda

Dr. Catalin Teodoriu

© Copyright by TENZIN DAWA 2024
All Rights Reserved.

ACKNOWLEDGEMENTS

While the pursuit of knowledge offers its own intrinsic rewards, the opportunity to apply that knowledge and make a contribution is a true privilege. This thesis represents the culmination of a journey filled with both challenges and growth, and I am deeply grateful to the many who have supported me along the way.

First and foremost, my deepest gratitude goes to my parents, Pema Gyaltsen and Tenzin Chodon, and my brother, Tenzin Yingsel. To my dearest Ama and Pala, thank you for being the pillars of strength and my biggest cheerleaders. Your love, encouragement, and belief in me have fueled my determination every step of the way. I am incredibly fortunate to have a supportive extended family in both the US and India. Their belief in me and their encouragement to pursue this journey have been a constant source of strength.

On the academic front, I am indebted to my advisor, Dr. Baharak Sajjadi for providing me with the opportunity to work on this project. Under Dr. Sajjadi's mentorship, I've received invaluable guidance and discovered an inspiring role model to follow in my own academic journey. I would also like to express my sincere thanks to my committee members, Dr. Deepak Devegowda and Dr. Catalin Teodoriu. Their insightful comments and suggestions have significantly strengthened the quality of this thesis.

Finally, I would like to express my sincere gratitude to Ms. Katie Shapiro, Mr. Gary Stowe, Dr. Ahmed Ramadan and Judge Keith Thomas, for their invaluable support during the past two years.

To all of you, my deepest thanks. This thesis would not have been possible without your unwavering support.

TABLE OF CONTENT

ACKNOWLEDGEMENTS iv
LIST OF TABLES vi
LIST OF FIGURES vi
ABSTRACT viii
CHAPTER 1: INTRODUCTION 1
1.1 Background 1
1.2 Problem statement 4
1.3 Objectives 5
1.4 Outline of thesis 6
CHAPTER 2: LITERATURE REVIEW 7
Perovskite Structures 13
Double Perovskites 14
Perovskite Synthesis 16
Perovskites in Chemical Looping (CL) Technologies 17
Perovskites in Chemical Looping Combustion (CLC) 19
Perovskites in Chemical Looping Reforming (CLR) 27
Perovskites in Chemical Looping Gasification (CLG) 46
CHAPTER 3: METHODOLOGY 53
CHAPTER 4: RESULTS AND DISCUSSIONS 62
4.1 Physical properties 62
4.2 CLG without steam 68
4.3 CLG with steam 77
4.3.1 Effect of temperature on chemical looping gasification 79
4.3.2 Effect of oxygen carrier on chemical looping gasification 80
4.4 Biochar asphalt mix 86
CHAPTER 6: CONCLUSIONS 90
References 91
Appendix A: 102

LIST OF TABLES

Table 1. Perovskite Structures for Chemical Looping Combustion..... 24
Table 2. Perovskite Structures for Chemical Looping Steam and Dry Methane Reforming..... 36
Table 3. Perovskite Structures for Chemical Looping Gasification..... 50
Table 4: Proximate and ultimate analysis of biomass (Miscanthus) composition. 54
Table 5:Ash composition of biomass (Miscanthus) samples. 54
Table 6. Calibration Standard Compositions 60
Table 7: Extracted spectrum weight % for each element by SEM. 63
Table 8: Mixing Protocols considered for binder mix 87

LIST OF FIGURES

Figure 1: The 3D crystal structure of perovskite structure ABX_3. Reprinted with permission from (Luo & Daoud, 2014). Copyright 2023 American Chemical Society..... 14
Figure 2: Synthesis Methods used for Perovskite Synthesis..... 17
Figure 3: An oxygen carrier particle can be reduced by H_2 and reoxidized by O_2. (Zeng et al., 2018) 18
Figure 4**:** a) Chemical Looping Combustion (CLC), b) Chemical Looping Reforming (CLR), c) Chemical Looping Gasification (CLG), d) Chemical Looping Air Separation (CLAS), e) Chemical Looping Dehydrogenation (CLDH), f) Chemical Looping Epoxidation (CLEPOX), g) Chemical Looping Oxygen Uncoupling (CLOU 19
Figure 5: Reaction mechanism diagram of 3DOM double perovskite-type La2NiCoO6 catalysts for soot combustion (Mei et al., 2020). 21
Figure 6: Matching oxygen migration rate with the surface reaction rate to reach high selectivity of syngas in CLRM. Reproduced from Ref. (H.-X. Zhang et al., 2022). 27
Figure 7: Reaction mechanism model for CLG over Mn/Ca2Fe2O5 OCs. Reproduced from Ref. (Liu et al., 2023)..... 48
Figure 8: a) Miscanthus biomass, b) dried and ground biomass, c) sieved biomass to the desired particle size, d) produced biochar (sieved for the second time to achieve the desired particle size) 53
Figure 9: Synthesis of oxygen carrier via sol-gel process. 56
Figure 10: Experimental setup for investigating biomass conversion processes: pyrolysis and gasification. 58
Figure 11: Schematic diagram of fixed bed catalytic biomass refinery system. (1) N_2 cylinder; (3) heating tape temperature controller; (4) Heating tape; (5) HPLC syringe pump 0.1 – 10 ml/min; (6) fixed bed furnace and quartz tubular reactor; (7) temperature controller of furnace; (8) bio-oil collector; (9) biomass sample; (10) sample stopper; (11) gas wash bottle; (12)

membrane filter; (13) gas bags; (14) Argon cylinder; (15) Gas chromatograph, Shimadzu; (16) split/spitless injection port; (17) Thermal conductivity detector; (18) Computer with Lab solution software; (19) online thermal sensor. 59
Figure 12: Schematic of the gas sampling setup. 60
Figure 13: Bio-oil (left) and biochar (right) collected during the biomass conversion process. . 61
Figure 14: SEM-EDS images of a) $Ca_2Fe_2O_5$, b) $Ca_2Fe_{1.9}Co_{0.1}O_5$, c) $Ca_2Fe_{1.9}Cu_{0.1}O_5$, d) $Ca_2Fe_{1.9}Ni_{0.1}O_5$. 64
Figure 15: TEM-EDS images of fresh a) $Ca_2Fe_2O_5$, b) $Ca_2Fe_{1.9}Co_{0.1}O_5$, c) $Ca_2Fe_{1.9}Cu_{0.1}O_5$, d) $Ca_2Fe_{1.9}Ni_{0.1}O_5$. 66
Figure 16: XRD images of fresh a) $Ca_2Fe_2O_5$, b) $Ca_2Fe_{1.9}Co_{0.1}O_5$, c) $Ca_2Fe_{1.9}Cu_{0.1}O_5$, d) $Ca_2Fe_{1.9}Ni_{0.1}O_5$. 67
Figure 17: FTIR spectra of oxygen carriers 68
Figure 18: Effect of doping $Ca_2Fe_2O_5$ with Cu, Co and Ni on gas composition and production during pyrolysis. 73
Figure 19: Gas composition and total gas production during pyrolysis stage at different temperatures. 75
Figure 20: Syngas concentration and yields from miscanthus pyrolysis using pure biomass, $Ca_2Fe_2O_5$, $Ca_2Fe_{1.9}Cu_{0.1}O_5$, $Ca_2Fe_{1.9}Co_{0.1}O_5$, and $Ca_2Fe_{1.9}Ni_{0.1}O_5$. 77
Figure 21: H_2 Production During Gasification Trials at Different Temperatures and Water Injection Rates 78
Figure 22: Effect of doping $Ca_2Fe_2O_5$ with Cu, Co and Ni on gas composition and production during gasification. 82
Figure 23: Gas composition and total gas production during gasification stage at different temperatures. 84
Figure 24: Syngas concentration and yields from miscanthus gasification using pure biomass, $Ca_2Fe_2O_5$, $Ca_2Fe_{1.9}Cu_{0.1}O_5$, $Ca_2Fe_{1.9}Co_{0.1}O_5$, and $Ca_2Fe_{1.9}Ni_{0.1}O_5$. 86

ABSTRACT

Chemical looping (CL) technology offers a promising avenue for producing high-purity hydrogen with inherent CO_2 separation. A critical challenge lies in identifying oxygen carriers with high performance and sustained activity across multiple redox cycles. This study investigates the influence of metal doping (Co, Cu, Ni) on the performance of brownmillerite-structured $Ca_2Fe_2O_5$ for biomass gasification and hydrogen production. Carriers were synthesized via a citric acid-assisted sol-gel method and tested in a fixed-bed reactor under atmospheric conditions. The study systematically examined the effects of temperature, water injection rate (steam/biomass ratio), and catalysts on biomass conversion. An optimal water injection rate of 0.1 mL/min with Ni-doped $Ca_2Fe_2O_5$catalyst significantly enhanced hydrogen yield by 82.4% compared to the undoped carrier. Increasing temperature consistently improved H_2 yield throughout the gasification process. Notably, doping with Ni and Co significantly increased H_2 yield from 27.82 g/mol biomass (undoped) to 33.15 g/mol biomass (Ni) and 32.05 g/mol biomass (Co), respectively. Furthermore, this research explored the valuable application of adding biochar to the asphalt mixture. The results revealed that incorporating biochar significantly improved the asphalt's performance against rutting and cracking, offering a promising and sustainable approach to enhance pavement longevity.

CHAPTER 1: INTRODUCTION

1.1 Background

The term "chemical looping combustion" (CLC) was initially coined to describe the concept of chemical looping. This innovative approach gained prominence primarily in the fields of power generation and CO_2 capture. The key advantage of CLC lies in the spatial separation of fuels and air during the reaction processes. This unique characteristic enhances its effectiveness in achieving efficient combustion and facilitating the capture of CO_2 (Li et al., 2020). Over the past two decades, chemical looping (CL) technology has been applied beyond just power generation and CO_2 capture. Compared to alternative CO_2 capture technologies, the advantage of adopting CL technologies is the inherent CO_2 capture without the energy cost for separation processes (Abuelgasim et al., 2021). Just like combustion of fossil fuels (Sharma, 2019), chemical looping combustion of solid biomass has the unique potential to generate energy with negative carbon emissions while entailing an energy penalty compared to traditional combustion that is lower than that of the competing carbon capture technologies (Coppola & Scala, 2021). It is important to highlight that the utilization of biomass as a fuel does not contribute to an increase in the overall atmospheric CO_2 inventory. When combined with carbon capture and storage (CCS) technology, the entire system can achieve a carbon-negative status. Through a synchronized reaction, the technology harnesses the inherent advantages of CL to produce syngas and generate hydrogen by utilizing water as a reactant (Yin et al., 2020). This method has gained significant popularity as the direct conversion of methane is difficult, leading to high consumption of energy. Syngas can further be processed into value-added products such as chemical feedstocks or liquid fuels, which have the potential to replace petroleum. The second product, hydrogen, is one of the most

promising energy carriers because of its high net calorific value of up to 121 MJ/kg (Ma et al., 2017).

Biomass chemical looping gasification (BCLG) utilizes two interconnected reactors that hold a metal oxide (M_xO_y) that acts as an oxygen carrier. This carrier transfers oxygen and heat from an air reactor (AR) to a fuel reactor (FR) without directly mixing the gases. In the FR, biomass is fed and breaks down into volatile compounds, tars, and char. These components react with a gasifying agent (like water vapor or carbon dioxide) and the oxygen carrier. This reaction produces a syngas mixture containing carbon dioxide, hydrogen, carbon monoxide, methane, and some heavier hydrocarbons. During this process, the oxygen carrier loses oxygen and becomes M_xO_{y-1}. The reduced carrier then travels to the AR where it's re-oxidized with air, preparing it for another cycle (Oscar Condori et al., 2021). Additionally, biochar carried over with the carrier is also combusted in the AR. The heat released from these exothermic reactions in the AR is carried back to the FR by the oxygen carrier, providing the energy needed for the endothermic gasification reactions (O. Condori et al., 2021).

BCLG prioritizes syngas (primarily H_2 and CO) production via enhanced partial oxidation (equation 1) compared to CLC. Additionally, steam or CO_2 can be introduced into the fuel reactor to promote steam reforming (equation 2) and CO_2 reforming (equation 3), further enhancing syngas yield.

$$C_nH_{2m}O_p + (n - p)M_xO_y \rightarrow nCO + mH_2 + (n - p)M_xO_{y-1} \quad \text{(Equation 1)}$$

$$C_nH_{2m}O_p + (n - p)H_2O \rightarrow nCO + (m + n - p)H_2 \quad \text{(Equation 2)}$$

$$C_nH_{2m} + nCO_2 \rightarrow 2nCO + mH_2 \quad \text{(Equation 3)}$$

It's important to note that reactions 1 and 2 are highly endothermic, requiring external heat input to the fuel reactor. Despite this, BCLG boasts several advantages. First, it eliminates the need for direct air-fuel mixing. Second, BCLG offers a cost-effective approach to generate heat necessary for converting methane (CH_4) to hydrogen (H_2), eliminating the need for expensive oxygen production (X. Zhao et al., 2017). Finally, BCLG leverages a unique benefit when utilizing biomass compared to coal: the inorganic components in biomass ash act as effective gasification catalysts.

Perovskites are a class of materials with the general formula ABO_3, where A and B are cations. They are known for their unique crystal structure, which gives them a variety of desirable properties, including high reactivity, good stability, and ease of synthesis (Cao, Luo, Xing, et al., 2022). These properties make perovskites well-suited for use as oxygen carriers in CL technology. There are several advantages to using perovskites as oxygen carriers in CL technology. First, perovskites are highly reactive, which means that they can quickly transfer oxygen to fuels. This is important for achieving high efficiency in chemical looping reactions. Second, perovskites are stable under a wide range of conditions, including high temperatures and pressures. This makes them well-suited for use in industrial applications. Third, perovskites are relatively easy to synthesize, which makes them a cost-effective option for oxygen carriers. The properties of perovskites can be tailored to optimize their performance for specific applications. For example, the composition of a perovskite can be changed to alter its oxygen-carrying capacity or its reactivity. Additionally, the surface of a perovskite can be modified to improve its stability or its catalytic activity.

Ca-based perovskites have been extensively studied for their potential as oxygen carriers and catalysts in biomass gasification processes (Dawa & Sajjadi, 2024). These materials offer several

advantages over traditional catalysts, including high oxygen-carrying capacity, good stability, and catalytic activity. Several studies have demonstrated the effectiveness of Ca-based perovskites in promoting biomass gasification reactions. Liu et al. found that $CaMn_{0.6}Fe_{0.4}O_3$ can simultaneously act as both an oxygen carrier and a catalyst, leading to increased H_2/CO production and lower energy consumption compared to gasification without a catalyst (C. Liu et al., 2018). The enhanced performance of $CaMn_{0.6}Fe_{0.4}O_3$ is attributed to the increased d-spacing caused by Mn-doping, which promotes the formation of high-charge Mn ions and facilitates oxygen-ion migration and oxygen activation (Liu et al., 2023). $CaFe_2O_4$ and $Ca_2Fe_2O_5$ have been shown to achieve gasification efficiencies of 89.21% and 92.49%, respectively (Zhang et al., 2017). Sun et al. further investigated the performance of three calcium ferrite catalysts (CaO-$Ca_2Fe_2O_5$, $Ca_2Fe_2O_5$, and $CaFe_2O_4$) for gasifying pine wood and found that $Ca_2Fe_2O_5$ exhibited superior H_2-rich syngas yields (Sun et al., 2018). This superior performance is attributed to $Ca_2Fe_2O_5$'s continuous promoting mechanism and remarkable redox durability. Liu et al. elucidated the reaction pathway for Mn/$Ca_2Fe_2O_5$ perovskites in chemical looping gasification (CLG) of biogas residue (Liu et al., 2023). The proposed pathway involves oxygen uncoupling, CO_2 catalytic conversion, regeneration of oxygen uncoupling vacancy, and ultimately recoverable oxygen uncoupling. However, $Ca_2Fe_2O_5$ faces challenges such as Fe_3C formation, carbon deposition, weak oxygen release, and easy sintering. These challenges can be addressed by doping $Ca_2Fe_2O_5$ with other elements to enhance its oxygen-carrying capacity and catalytic activity. There have been relatively few studies conducted on using modified $Ca_2Fe_2O_5$ in CL applications and further research is needed to optimize the performance of $Ca_2Fe_2O_5$ and make it a viable option for large-scale CLG applications.

1.2 Problem statement

BCLG is a promising technology for producing clean syngas and hydrogen from biomass with inherent CO_2 capture. However, achieving optimal performance in BCLG relies heavily on the oxygen carrier material. While $Ca_2Fe_2O_5$ perovskites demonstrate potential as oxygen carriers, limitations such as weak oxygen release, carbon deposition, and sintering hinder their large-scale application.

This research aims to address these limitations by investigating the effects of Co, Ni, and Cu doping on the performance of $Ca_2Fe_2O_5$ in BCLG. The specific objectives are to:

1. Evaluate the impact of Co, Ni, and Cu doping on the reactivity of $Ca_2Fe_2O_5$ with biomass and its influence on syngas production.
2. Identify the optimal doping strategy to enhance the oxygen-carrying capacity and catalytic activity of $Ca_2Fe_2O_5$ for improved BCLG performance.
3. Investigate the influence of operating conditions (temperature and water injection rate) on gasification efficiency and product yields.

1.3 Objectives

To improve the performance of $Ca_2Fe_2O_5$ oxygen carriers in CLG, three metals – Co, Ni, and Cu – were selected for doping optimization. The reactivity of the doped OCs with biomass and their gas production performance were evaluated using fixed-bed experiments. In addition, their redox properties were investigated using characterization techniques such as X-ray diffraction (XRD), scanning electron microscopy (SEM), Brunauer-Emmett-Teller (BET) analysis, and hydrogen temperature-programmed reduction (H_2-TPR). This study aims to (1) investigate the feasibility of utilizing a $Ca_2Fe_2O_5$-based brownmillerite structure for high-purity hydrogen production through the CLG process, (ii) develop and characterize $Ca_2Fe_2O_5$ doped with Co, Ni, and Cu to

assess how dopant type and concentration impact reactivity with biomass, syngas production, and hydrogen enrichment, (iii) investigate the influence of key operating parameters, including temperature and water injection rate to maximize product yields, focusing particularly on the production of high-purity hydrogen and (iv) evaluate how biochar affects asphalt's behavior at high temperatures in bio-asphalt mixtures.

1.4 Outline of thesis

Chapter 1: Introduction

This chapter introduces the concept of Biomass Chemical Looping Gasification (BCLG) and its potential for clean syngas and hydrogen production with inherent CO_2 capture. We briefly highlight the challenges associated with oxygen carriers in chemical looping, while also outlining the advantages of both the chemical looping process and the use of perovskite structures. Additionally, we review previous research conducted on Ca-based perovskites for biomass gasification and highlight the key objectives of our work.

Chapter 2: Literature Review

This section delves into a comprehensive review of over 100 research papers exploring the utilization of perovskite structures within various chemical looping technologies. The analysis focuses specifically on the recent advancements and findings related to the application of perovskites as oxygen carriers or catalysts in these processes.

Chapter 3: Methodology

This section details the experimental approach employed in this study, encompassing:

1. Biomass Preparation: Selection, drying, and grinding of the chosen biomass feedstock.

2. Catalyst Synthesis: Synthesis of perovskite catalysts with characterization using appropriate techniques to confirm their structure and properties.
3. Experimental Setup: Description of the BCLG reactor configuration, including details on gas flow rates, temperature control, and GC used.
4. Experimental Procedure: Outline of the steps involved in BCLG experiments, including loading of biomass and catalyst, operating conditions (temperature, gas flow, water injection), and gas/solid product sampling procedures.
5. Analysis of Results: Description of the analytical techniques employed to characterize the gas and solid products obtained, including gas composition analysis and hydrogen yield determination.

Chapter 4: Results and Discussion

This section presents the key findings from the BCLG experiments. We discuss the composition and concentration of gases produced during the process, focusing on the comparison between pyrolysis and gasification results. Additionally, we analyze the influence of temperature and dopant type on hydrogen enrichment in the syngas product.

Furthermore, we present the optimal mixing protocol for incorporating biochar into asphalt mixtures. This section also investigates the impact of biochar particle size and production temperature on the high-temperature properties of the resulting binder blends.

CHAPTER 2: LITERATURE REVIEW

In 1897, Franz Bergmann was recognized for applying a chemical looping principle to convert hydrocarbons and calcium oxide into calcium carbide using manganese oxides. His pioneering

work in this field marked an early application of the chemical looping concept (Bergmann, 1897). Some batch experiments were carried out in the 1900s. However, the process could not be consistently operated as the technologies were only implemented at the pilot scale and not successfully scaled up for commercial use. This was primarily due to various factors such as low reactant conversions, high capital costs, and the deterioration of the looping carriers (Fan, 2017). During the 1990s, E. I. DuPont de Nemours and Company (DuPont) achieved a significant milestone by successfully commercializing chemical looping technology for the production of maleic anhydride from n-butane. Their groundbreaking approach involved the utilization of a vanadium pyrophosphate catalyst encapsulated in a silica shell. This chemical looping process was implemented in a circulating fluidized bed (CFB) configuration, marking DuPont as the first major industrial corporation to bring this technology to market (Patience & Bockrath, 2010). The emergence of the 21st century marked a notable period characterized by the global development and operation of numerous chemical looping units. This trend of ongoing interest and active construction of demonstration units signifies the growing significance and relevance of chemical looping systems in various industrial applications. Such developments underscore the potential and promise of chemical looping as a valuable technology for the industry.

The term "chemical looping combustion" was initially coined to describe the concept of chemical looping. This innovative approach gained prominence primarily in the fields of power generation and CO_2 capture. The key advantage of chemical looping lies in the spatial separation of fuels and air during the reaction processes. This unique characteristic enhances its effectiveness in achieving efficient combustion and facilitating the capture of CO_2 (Li et al., 2020). Over the past two decades, chemical looping technology has been applied beyond just power generation and CO_2 capture. Applications include chemical looping steam methane reforming, biomass decomposition,

ammonia synthesis, full oxidation, partial oxidation, selective oxidation, super dry reforming, dry reforming, desulfurization, and thermochemical CO_2 and H_2O splitting. Additionally, chemical looping processes have been utilized for converting fossil fuels into both power and chemicals, while simultaneously capturing CO_2 in-situ. Notably, these applications demonstrate good integration of process heat, further enhancing their efficiency (Li et al., 2017). Compared to alternative CO_2 capture technologies, the advantage of adopting CL technologies is the inherent CO_2 capture without the energy cost for separation processes (Abuelgasim et al., 2021). Just like combustion of fossil fuels, chemical looping combustion of solid biomass has the unique potential to generate energy with negative carbon emissions while entailing an energy penalty compared to traditional combustion that is lower than that of the competing carbon capture technologies (Coppola & Scala, 2021). It is important to highlight that the utilization of biomass as a fuel does not contribute to an increase in the overall atmospheric CO_2 inventory. When combined with carbon capture and storage (CCS) technology, the entire system can achieve a carbon-negative status. CL technologies find another significant application in reforming processes. Methane, a key component of natural gas and biogas, can be effectively converted into high-quality syngas . A novel technology known as chemical looping steam methane reforming (CLSMR) has emerged to facilitate this methane reforming process while simultaneously generating hydrogen from water. CLSMR represents an innovative approach where chemical looping principles are utilized to enable the efficient conversion of methane into syngas. Through a synchronized reaction, the technology harnesses the inherent advantages of CL to produce syngas and generate hydrogen by utilizing water as a reactant (Yin et al., 2020). This method has gained significant popularity as the direct conversion of methane is difficult, leading to high consumption of energy. Syngas can further be processed into value-added products such as chemical feedstocks or liquid fuels, which

have the potential to replace petroleum. The second product, hydrogen, is one of the most promising energy carriers because of its high net calorific value of up to 121 MJ/kg (Ma et al., 2017). On the other hand, chemical looping dry reforming of methane (CLDRM) is a potential alternative to the traditional steam reforming process, which can produce syngas with a [H_2]/[CO] ratio equal to 2 during the reduction step (Adanez et al., 2012), (García-García & Metcalfe, 2021). From an environmental point of view, CLDRM is a novel application since two greenhouse gas molecules (methane and carbon dioxide) are converted into valuable products (hydrogen and carbon monoxide). Aside from reforming, thermochemical water splitting is another promising technique for efficiently producing green hydrogen at scale using thermal energy (Ozcan et al., 2023). While the current hydrogen market heavily relies on fossil-fuel-based platforms, the thermochemical water-splitting systems based on the reduction-oxidation (redox) looping reactions have a significant potential to contribute to the sustainable production of green hydrogen at scale. It is a process in which pure H_2 is produced with capturing relatively pure CO_2 (i.e., separate H_2 and CO_2 streams). CL can also be used for the removal of catalyst deactivating agents such as sulfur (desulfurization). Fossils and most renewable fuels contain significant amounts of sulfur contaminants (mainly in the form of H_2S), which can react with metals and metal oxides to form the corresponding metal sulfides and can thus impact the performance of carrier materials used in CL technologies (Jerndal et al., 2006). Metal sulfides often have lower melting points compared to the corresponding metals or metal oxides. As a result, the operating temperature of a combustion process is influenced by this characteristic. However, the challenges posed by sulfidation can be mitigated by employing desulfurized fuels or periodically regenerating the carrier material through oxidation with air (Solunke & Veser, 2011). This regeneration process effectively removes physically and/or chemically bound sulfur from the carrier material, which is

an inherent feature of CLC (chemical looping combustion) processes. In CLC, the carrier material, in its reduced state, is cyclically transferred to the oxidizer, where it undergoes re-oxidation using oxygen from the air. Therefore, if the carrier material becomes sulfurized during the reduction phase, it will be subsequently regenerated in the oxidizer during the next cycle. Consequently, if the carrier material has a strong affinity for sulfur compounds, CLC has the potential to facilitate the desulfurization of the fuel-side effluent. By leveraging the fundamental principles of CLC, such as periodic regeneration and the affinity of carrier materials for sulfur species, the process can effectively address sulfidation concerns and enable the desulfurization of fuel-side effluents. Furthermore, CL technologies exhibit potential for the production of various chemicals, including ethene and ammonia. One notable application is chemical looping oxidative dehydrogenation (CLODH) of ethane, which offers advantages in terms of avoiding air separation and explosion concerns. This process utilizes the lattice oxygen present in the catalysts to facilitate the oxidation of ethane, resulting in the production of ethene. Subsequently, the reduced redox catalysts are efficiently regenerated through exposure to air. This approach showcases the capacity of CL technologies to enable a safer and more streamlined oxidative dehydrogenation process for the production of ethene, while ensuring the efficient recovery and reuse of catalysts through periodic regeneration (García-García & Metcalfe, 2021). CL technologies also offer several advantages over the conventional Haber-Bosch process when it comes to ammonia production. These benefits include lower energy consumption, reduced greenhouse gas emissions, and decreased capital costs. By leveraging CL technologies, the efficiency of ammonia production can be significantly improved by minimizing the energy requirements for gas separation and purification processes. The overall cost reduction is primarily achieved by decreasing the plant cost associated with the reforming unit and CO_2 separation. Consequently, the utilization of CL technologies yields a

negative cost for CO_2 avoidance, typically ranging from -$1 to -$5 per ton of CO_2, depending on factors such as the cost of oxygen carriers and chemical looping reactors. These advantages position chemical looping as a promising and economically viable alternative for ammonia production, with the potential to not only enhance process efficiency but also contribute to sustainability goals by reducing both energy consumption and greenhouse gas emissions.

In all the aforementioned CL applications, perovskites can be used as oxygen carriers in the absence of air to promote reactions between oxygen and fuels. Perovskites can be reduced by the fuel to form a metal oxide and release oxygen, which can then react with the fuel to produce carbon dioxide and water. The reduced metal oxide can then be re-oxidized in a separate step, regenerating the perovskite, and releasing the captured carbon dioxide in a concentrated form that can be easily captured and stored. Therefore, they undergo macroscopic redox cycles of reduction and oxidation reaction cycles with significant loss and gain of surface and lattice oxygen. Due to their excellence in redox reaction, reducibility, ionic electronic properties, and high thermal stability, these materials have been widely studied (Cao, Luo, Xing, et al., 2022). The use of perovskites as oxygen carriers in chemical looping technology offers several advantages over other materials, including high reactivity, good stability, and ease of synthesis. Additionally, perovskites can be tailored to optimize their properties for specific applications, such as high-temperature or low-temperature reactions reactors.

This review will provide a systematic and comprehensive summary of recent studies exploring perovskite structures and their applications in chemical looping. This review seeks to investigate the performance of those perovskite structures in different chemical looping processes, highlighting their unique properties, reactivity, and stability. This review also aims to evaluate the diverse applications and capabilities of perovskites in various chemical looping technologies

where perovskites have demonstrated their effectiveness, including combustion, steam and dry reforming and gasification.

Perovskite Structures

Perovskites, a vast family of compounds, possess structures that are closely related to $CaTiO_3$. The initial discovery of these structures can be attributed to Lev Perovski in 1792 (Cheng & Lin, 2010). However, their detailed description was first provided by Wenk and Bulakh in 1926, and later on published in 1945 (Szuromi & Grocholski, 2017). Due to their high stability and versatility to accommodate various cations into their structures, perovskites and perovskite-derived structures represent some of the most important geological compounds (Zhu et al., 2018). Perovskites exhibit a common structure known as ABX_3, wherein 'A' and 'B' represent cations of differing sizes, and 'X' represents an anion that forms bonds with both cations. The crystal structure of ABX_3 perovskite is depicted in Figure 1, showcasing the arrangement and configuration of the A, B, and X atoms within the perovskite lattice. The A-site typically consists of divalent base alkaline, alkaline-earth, or rare-earth metal elements with larger ionic radii, while the B-site comprises transition metal elements with smaller ionic radii. X is commonly oxygen or other larger ions like halides, sulfides, and nitrides. The 'A' atoms are larger than the 'B' atoms (Ono et al., 2017), and both can be substituted by any metal or semimetal from the periodic table. The atomic arrangements in perovskite structures were first described for the mineral perovskite calcium titanate as “sub- metallic to metallic luster cube like-structure with deficient cleavage and hard tenacity, colorless streak or colors include orange, black, brown, yellow and gray” (Whitfield et al., 2016). In a perovskite cubic unit cell, A cations are 12-fold coordinated and sit in corners of the cube at corner position (0, 0, 0) while X atoms are at the face center of the cubic lattice at position (1⁄2, 1⁄2, 0) but tetravalent B cations lie within the octahedral, occupying the body center

position (1⁄2, 1⁄2, 1⁄2) (Assirey, 2019). The structure is pictured as a three-dimensional network of regular corner linked BO_6 octahedral (Tan et al., 2014).

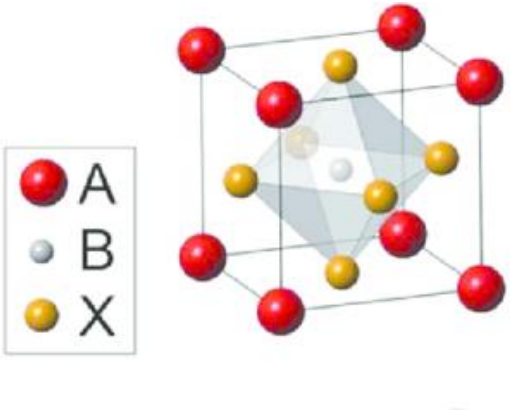

Figure 1: The 3D crystal structure of perovskite structure ABX_3. Reprinted with permission from (Luo & Daoud, 2014). Copyright 2023 American Chemical Society.

Double Perovskites

Double perovskites are the perovskites with the A or B site occupied by two different types of cations, giving the formulas of $A'A''B_2O_6$ (double A-site) or $A_2BB'O_6$ (double B-site). The A-sites of double A-sites are characterized by valences of +1 or +2, typically encompassing elements from the first or second group of the periodic table, such as K, Ba, Sr, and others. Conversely, the B and B' sites predominantly exhibit variable oxidation states (+3, +4, +5, +6) combined stoichiometrically (Basavarajappa & Chakraborty, 2022). The double B-sites are perovskites where two different B cations occupy the center of the cube resulting in a ratio of $r_A/(r_{B1} + r_{B2})$ or $(r_{A1} + r_{A2})/r_B$ different from 1. Examples include Sr_2FeMoO_6 and Ba_2YMoO_6 (Vries et al., 2010) where two different B cations occupy the center of the perovskite cube. These structures have been widely investigated because they have high oxygen surface exchange kinetics and fast oxygen ion diffusion rates, and good mixed ionic and electronic conductivity at elevated temperature (Y. Cao et al., 2021). These structures also hold a more orderly structure arrangement, thereby preventing

lattice distortion and improving cycling stability. Compared with simple perovskite, A and B-site double perovskite with more substitution sites provide more opportunities to regulate the crystal structure, electronic and ionic defects, and therefore enhance the electrochemical performance (King & Woodward, 2010).

Since A-site cations usually act as an electron donor to the [BO_6] framework and the physical properties of ABO_3 perovskites are highly dependent on B-site cations, double perovskites usually indicate double B-site perovskites (Yin et al., 2019). The crystal structure of a double perovskite $A_2B'B''O_6$ is determined by the arrangement of B′ and B″ cations in the B sublattice. For the 1:1 B-site ordered perovskite, the B- and B′-site elements behave very differently in chemical valence. The B-site cation is occupied by low valence cations (Fe, Co, Ni, Mg, and so forth), while the B′-site cation usually has high valence, such as Nb, Mo, and W, and so forth. They are ordered in the configuration of -[B-O-B′-O-B]- along three axes, forming a B-site rock-salt like structure (Figure 5b). The three main kinds of B-cation sublattice include random, rock salt and layered structures. These arrangements are determined by the charge difference (ΔQ) between B′ and B″. Based on the existing double perovskites, the random order dominates when $\Delta Q = 1$, but the rock-salt order dominates when $\Delta Q > 2$. Since $\Delta Q \geq 2$ in most of the double perovskites, the rock-salt order accounts for the majority of double perovskites.

In the case of A-site ordered double perovskite $AA'B_2O_6$, A is generally a lanthanide element (Pr, Nd, Sm, Gd, and so forth) with a smaller ionic radius while the A′ is usually a large cation, such as the alkaline earth metal Ba. Due to the great difference in ionic radii between A and A′ cations, A-site double perovskite tends to form an A-site layered structure with a stacking sequence of -[AO_δ]-[BO_2]-[A′O]-[BO_2]-[AO_δ]- along the *c* axis. The ordering in A-site double perovskite could be partial in whole lattice, depending on the difference in cation valence. The oxygen in the [AO_δ]

layer can be fully occupied, half-occupied, or even completely removed, depending on differences in the size of the A and A′ cation and/or environment atmosphere. The high content of oxygen vacancies in the [AO_{δ}] layer provides rapid migration channels for oxygen ions, therefore, the $AA'B_2O_6$ perovskite demonstrates unique oxygen surface exchange and migration properties (M. Zhang et al., 2022).

Perovskite Synthesis

Perovskite synthesis methods have advanced rapidly since their first development using the simple ceramic method in the 1970s. The main goal of this progress has been to improve the poor textural properties of perovskites, which are important for catalytic applications where surface area is key (Royer et al., 2014). This has led to the development of more efficient synthesis routes, such as the sol-gel method, solid-state reaction, Pechini and modified Pechini techniques, wet impregnation method and spray drying method (Figure 2). Perovskites synthesized through these

methods have been utilized by various researchers for applications in CL technologies.

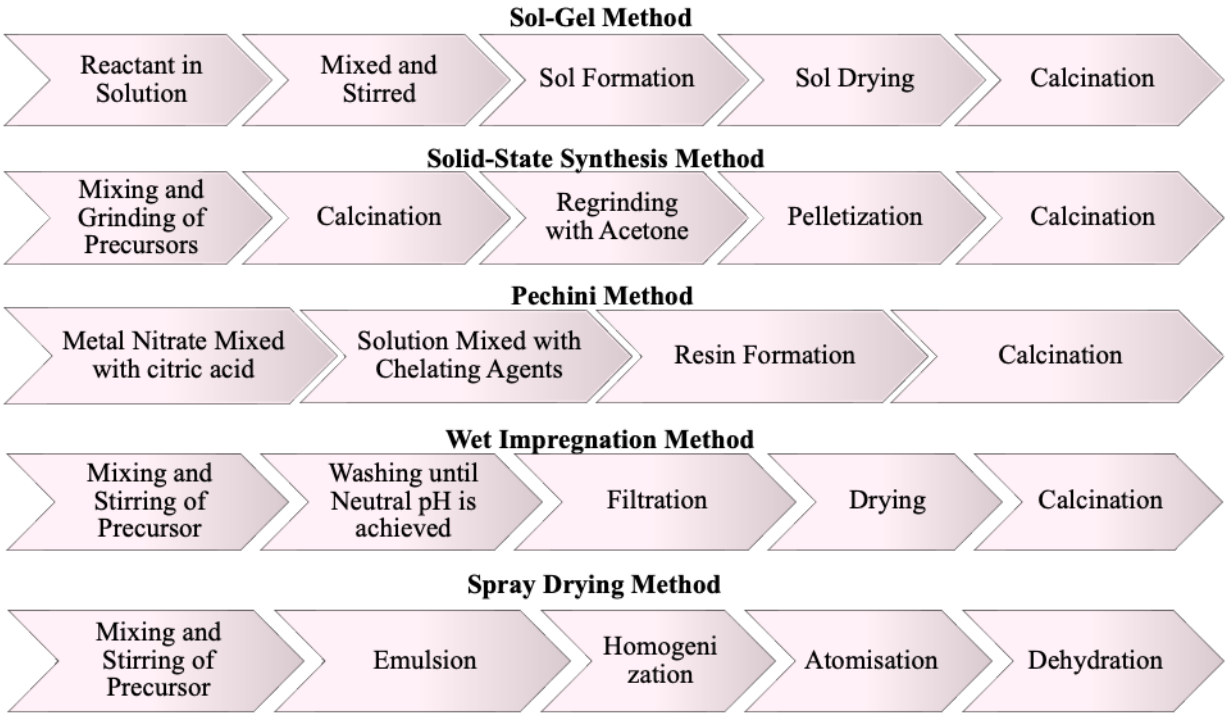

Figure 2: Synthesis Methods used for Perovskite Synthesis

Perovskites in Chemical Looping (CL) Technologies

Chemical looping represents an important category of technologies, which can be deployed for direct combustion, used in reforming applications, gasification, oxygen uncoupling, air separation, oxidative dehydrogenation, and epoxidation. In this kind of system, oxygen is added to the fuel gas via a solid carrier so that it may later be released as a pure CO_2 stream that is suited for consumption, or more likely sequestration or storage. The solid is then regenerated in a reactor using an oxygen source (e.g. air, steam or carbon dioxide), so that the technology effectively achieves oxygen separation from the oxygen source without the use of a costly cryogenic process or membrane technology (Anthony & Symonds, 2022). Cycles of gas-solid reactions make up a chemical looping process, and the performance of the oxygen carriers is crucial to its efficient

functioning. The total process in a typical chemical looping system may be thought of as burning and partial oxidation/reforming of the fuels, which calls for certain oxygen carrier qualities in order to correctly manage the product selectivity (Zheng et al., 2022).

One of the major issues with the chemical looping principle is the selection of suitable oxygen carrier (OC) material (Figure 3). Oxygen carriers (metal oxides or perovskites) are applied for the chemical looping process in place of air to offer oxygen for fuel combustion. These oxygen carrier particles consist of reducible MO_x compounds with three key functions: generating oxygen ions or vacancies and electrons or holes, facilitating their diffusion in the bulk phase, and providing active sites for surface reactions (Zeng et al., 2018). Because of a variety of factors, including thermal activity, cost, availability, environmental, and safety concerns, it is difficult to classify suitable candidates as OC in the chemical looping (CL) process. Some characteristics of an efficient oxygen carrier include high surface areas and low transport resistances between the external atmosphere, intraparticle pores and particle surface.

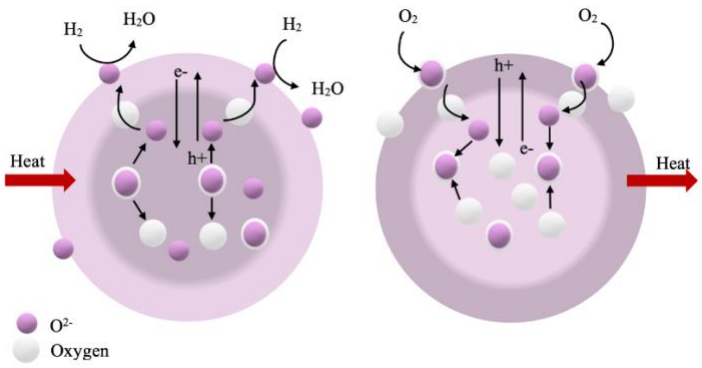

Figure 3: An oxygen carrier particle can be reduced by H_2 and reoxidized by O_2. (Zeng et al., 2018)

In the subsequent sections, we will explore various chemical looping technologies (Figure 4) described in the literature and examine how different perovskite structures have been utilized in recent times to enhance process efficiency, along with their underlying mechanisms.

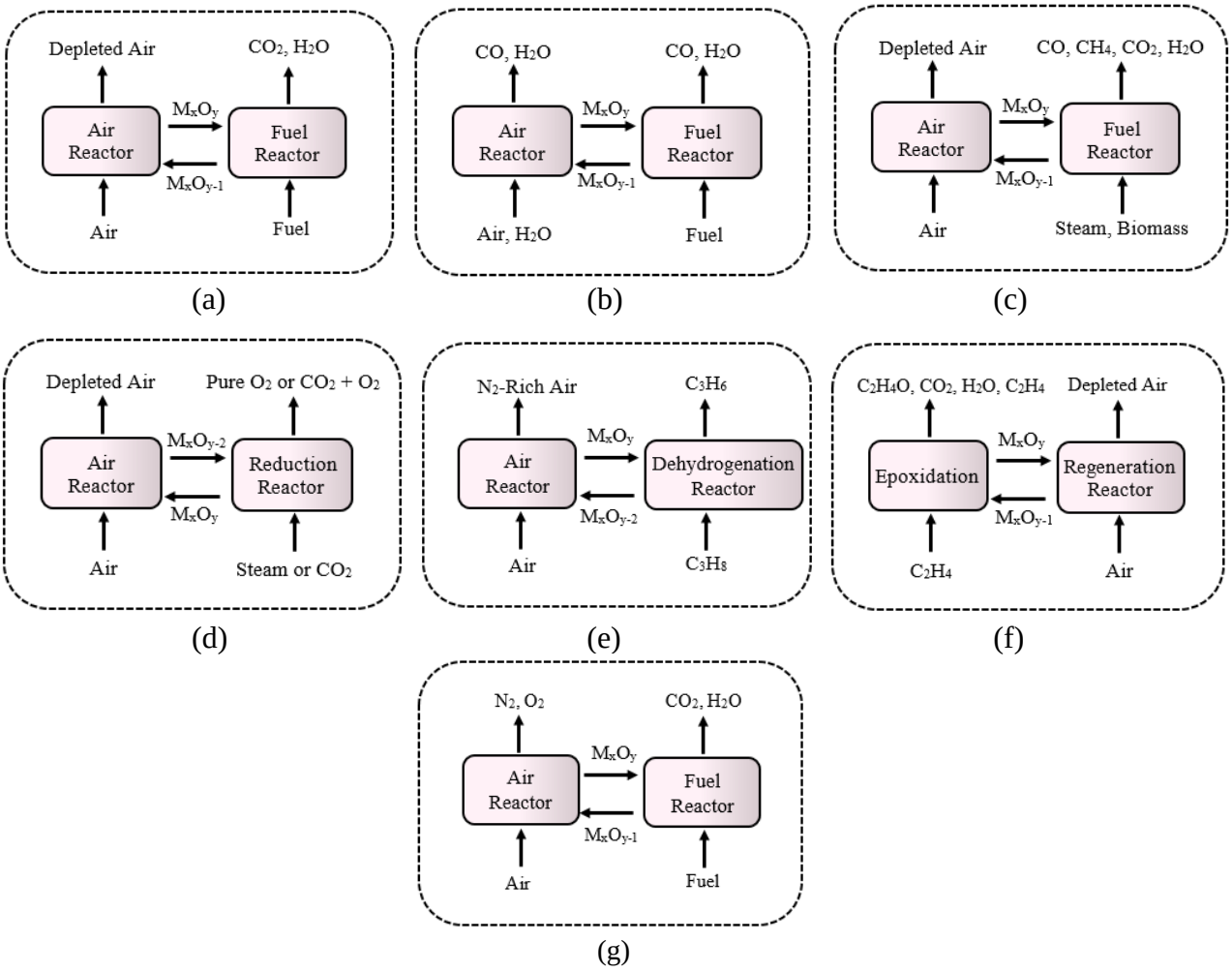

Figure 4: a) Chemical Looping Combustion (CLC), b) Chemical Looping Reforming (CLR), c) Chemical Looping Gasification (CLG), d) Chemical Looping Air Separation (CLAS), e) Chemical Looping Dehydrogenation (CLDH), f) Chemical Looping Epoxidation (CLEPOX), g) Chemical Looping Oxygen Uncoupling (CLOU

Perovskites in Chemical Looping Combustion (CLC)

Table 1 presents a comprehensive list of perovskite structures that have been utilized in chemical looping combustion (CLC), along with their respective reaction parameters and main findings. In recent years, Ca-based perovskites have gained much attention for scale up of CLC processes. Ca-

Mn based perovskites can facilitate fuel combustion as they release gaseous oxygen. They are made of cheap materials and suitable candidates for CLC. Abad et al. (Cabello et al., 2021) explored the use of $CaMn_{0.775}Ti_{0.125}Mg_{0.1}O_{2.9-\delta}$, the first and only oxygen carrier prepared at ton-scale, which exhibits promising features for the CLC scale-up.
In-situ activation of perovskite via air heating resulted in a remarkable performance enhancement: oxygen release rate increased by up to 50%, carbon monoxide production decreased by up to 70%, and the temperature requirement for CLC decreased by up to 100 degrees Celsius (Cabello et al., 2021). Källén, et al investigated the use of $CaMn_{0.9}Mg_{0.1}O_{3-\delta}$ as oxygen carrier for CLC of natural gas. $CaMn_{0.9}Mg_{0.1}O_{3-\delta}$ was able to reversibly store and release oxygen at high temperatures and convert natural gas to CO_2 and H_2O with high efficiency. Minimal formation of fines was estimated at below 0.01%, suggesting that the particles have the potential for a significantly extended lifespan (Källén et al., 2013). Pachler et al. (Pachler et al., 2019) focused on examining the impact of sulfuric fuel impurities on CLC using a 120 kWth pilot unit comprising interconnected circulating fluidized beds. In the investigation, $CaMn_{0.775}Mg_{0.1}Ti_{0.125}O_{3-\delta}$ was used as an oxygen carrier and natural gas was employed as fuel. It was found that the presence of sulfur in the fuel feed negatively affects the general fuel conversion performance of the perovskite oxygen carrier, and it gets captured by the perovskite oxygen carrier as crystalline phases of MgS. Also, regeneration of the perovskite after switching off the sulfur feed was not possible. Further research is needed to develop strategies for mitigating the effects of sulfur on CLC performance.
There have been various reports on the ability of La-based perovskites to facilitate CLC. The ability to tune their properties, such as electronic and ionic conductivity and catalytic activity, by controlling their elemental composition, makes them especially attractive (Readman et al., 2005). Readman et al. (Readman et al., 2005) studied the feasibility of $La_{1-x}Sr_xCo_{1-y}Fe_yO_{3-\delta}$ perovskites

by investigating their structural properties under both oxidative and reductive atmospheres. These structures had the redox properties required for CLC. Jiang et al. (Jiang et al., 2018) combined thermal cycle with solar-heat driven chemical-looping combustion (S-CLC) to investigate the properties of $LaCu_xNi_{1-x}O_3$. They found that x = 0.1 is the ideal copper substitution and more than 46% of these structures reduced in 5 minutes and no carbon deposition was observed.

Mei, et al. (Mei et al., 2020) synthesized double perovskite-type $La_2NiB'O_6$ (B' = Mn, Fe, Co, Cu) catalysts with a three-dimensional ordered macroporous (3DOM) structure using the colloidal crystal template method. The 3DOM structure enhanced the contact efficiency between soot and the catalyst. The arrangement of $[NiO_6]$ and $[B'O_6]$ octahedrons in $La_2NiB'O_6$ created coordination unsaturated B-site ions. The 3DOM $La_2NiB'O_6$catalysts exhibited excellent catalytic performance for soot combustion in simulated exhaust, with their performance depending on the synergistic effect of binary Ni and B'-site ions. Among the catalysts, the La_2NiCoO_6 catalyst showed greatest level of catalytic activity for soot combustion, with a maximum soot combustion rate of 98.2%. The mechanism proposed (Figure 5) suggests that the synergistic effect of Ni and B' ions enhances the crucial step of NO oxidation to NO_2. They also suggest that the key step in the elimination of soot by the La_2NiCoO_6 catalyst involves the oxidation of NO to NO_2 by surface active oxygen species. These 3DOM catalysts, as non-noble metal nanocatalysts, showed promising potential for practical applications in catalytic diesel soot elimination.

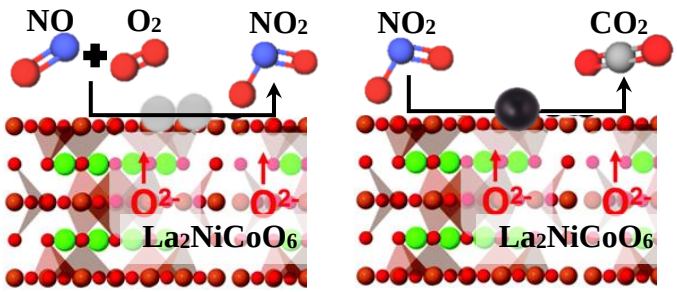

Figure 5: Reaction mechanism diagram of 3DOM double perovskite-type La2NiCoO6 catalysts for soot combustion (Mei et al., 2020).

Fang, et al. (Fang et al., 2018) synthesized $La_{1-x}K_xFeO_{3-\delta}$ nanotubes using electrospinning and calcination techniques for efficient soot oxidation. The addition of a certain amount of K^+ ions into the inhibited crystallite growth during high-temperature calcination, which further prevented the destruction of the macro/mesoporous tubular structure and increased contact between soot particles and active sites. It also resulted in a higher density of oxygen vacancies, enhancing the redox abilities of the catalyst. However, excessive K^+ doping caused the collapse of the macro/mesoporous tubular structure, which negatively affected the catalytic performance. They found that $La_{0.8}K_{0.2}FeO_{3-\delta}$ nanotubes exhibited the best performance for soot removal.

Cui. et al. (Cui et al., 2020) explored A-site disubstituted lanthanides and discovered that the right amount of K^+ doping might lessen the catalyst's tendency to sinter, decrease the thermal stability of the catalyst, speed up the coal's burning, and enhance the catalytic effect. The catalyst with the greatest combustion reaction rate was $La_{0.66}Sr_{0.2}K_{0.14}MnO_3$, which also caused significant changes in the catalyst's specific surface area and particle size. Substituting Sr^{2+} and K^+ with La^{3+} in the A-site of $LaMnO_3$ resulted in expansion of the unit cell and an increase in particle size. Introducing K^+ doping reduced the thermal stability of coal and increased the combustion rate. The incorporation of K^+ cations in the A-site led to enhanced activity of adjacent O^{2-} anions on the dodecahedron sites and increased vacancies in these sites. Oxygen vacancies located on the catalyst surface facilitated greater O_2 adsorption, resulting in a higher combustion rate for coal.

Sarshar and Kaliaguine (Sarshar & Kaliaguine, 2013) explored the reduction reaction of two OC, a perovskite material ($LaMnO_3$) and the same perovskite covered with a silica shell ($LaMnO_3$@ SiO_2). The silica shell was found to protect the perovskite from sintering under high-temperature CLC conditions. However, the activation energies determined for the reduction of $LaMnO_3$ and

$LaMnO_3$@ SiO_2 were 23 and 57 kJ/mol respectively, indicating the increased difficulty of reducing the perovskite phase.

In the United States, coal-fired power plants are the largest source of Hg emissions to the atmosphere. The Environmental Protection Agency (EPA) estimates that coal-fired power plants emit about 49% of all Hg emissions in the United States. Yanget al. (J. Yang et al., 2023) state that the perovskite $La_{0.8}Ce_{0.2}MnO_3$ has a high efficiency for Hg^0 capture. It was able to remove 99.9% of Hg^0 from coal combustion flue gas at 250 °C. The pellets were also able to be reused for up to 10 cycles without significant loss of efficiency. The high efficiency of the perovskite was attributed to its large surface area, which allows it to adsorb more Hg^0 molecules. $La_{0.8}Ce_{0.2}MnO_3$ could withstand the harsh conditions of coal combustion flue gas, such as high temperatures and acidic environment. This makes it a promising material for Hg^0 capture from coal combustion flue gas.

Ksepko(Ksepko, 2018) studied the effect of Cu^{2+} doping on the B site in the $Sr(Fe_{1-x}Cu_x)O_{3-\delta}$ on the oxygen transport capacity. At 600 °C, the highest oxygen capacity of 4.01 wt% was observed for $Sr(Fe_{0.67}Cu_{0.33})O_3$, indicating a synergistic effect between Fe and Cu. Additionally, all OCs were capable of releasing oxygen at temperatures as low as 600 °C, and their oxygen capacities increased with temperature, reaching 3.8, 4.22, and 4.86 wt% at 800 °C for $Sr(Fe_{0.9}Cu_{0.1})O_3$, $SrFeO_3$, and $Sr(Fe_{0.67}Cu_{0.33})O_3$, respectively. The materials exhibited high temperature stability, with melting temperatures well above 1200 °C and no signs of agglomeration, enabling their use over multiple redox cycles. Kwonget al. (Kwong et al., 2022) investigated the combustion of biomass char in fluidized beds containing $SrFeO_{3-\delta}$ and compared its performance to other oxygen carriers. They found that released gaseous O_2 at all temperatures studied. At 1168 K, the uncoupling reaction from SFO ($SrFeO_3$) lasted approximately 30 seconds based on numerical simulations.

Table 1. Perovskite Structures for Chemical Looping Combustion

Catalyst information	Support	Reaction parameters	Results	Main findings/conditions	Ref
La Based Perovskites					
$La_{1-y}Ca_yCu_xNi_{1-x}O_3$ x = 0, 0.1, 0.2, 0.3, 0.5 y = 0, 0.1, 0.5, 0.9 SM: combustion Calcination: 900 °C, 6 h		F: CH_4 CH_4: OC = 5:1 $\dot{Q}$: 20 mL min^{-1} T: 200 – 600 °C	η($X(CH_4)$: 90% R_O: 1.5 wt% C: > 8 cycles	Ca^{2+} can facilitate the element dispersion on the bulk, leading to high surface areas. $La_{0.1}Ca_{0.9}Cu_{0.1}Ni_{0.9}O_3$ showed satisfying coke resistance and regenerability. Promising OC for low-temperature CLC processes.	(Jiang et al., 2020)
$LaNi_{1-x}Co_xO_3$ (x = 0.0; 0.2; 0.5; 1.0) SM: citrate method Calcination: 330 °C, 2 h, 800 °C, 4h, 1000 °C, 2 h		F: CH_4 T: 700 – 850 °C $\dot{Q}$: 20 mL min^{-1}	Total amount of oxygen desorbed (mol O_2 mg^{-1}): $LaNiO_3$ 8.76×10^{-7} $LaNi_{0.8}Co_{0.2}O_3$ 6.71×10^{-7} $LaNi_{0.5}Co_{0.5}O_3$ 3.38×10^{-7} $LaCoO_3$ 1.48×10^{-7}	Nickel substitution for cobalt reduced active oxygen, decreasing catalyst activity for methane combustion. Cobalt insertion enhanced catalyst re-oxidation & reduced coke deposition. $LaNi_{0.5}Co_{0.5}O_3$ lead to a complete reduction in less time. The proposed order of catalytic oxidation activity: $LaNiO_3$ > $LaNi_{0.8}Co_{0.2}O_3$ > $LaNi_{0.5}Co_{0.5}O_3$ > $LaCoO_3$	(de Santana Santos et al., 2021)
$La_2NiB'O_6$ B'= Mn, Fe, Co, Cu SM: colloidal crystal template Calcination: 600 °C, 4 h		soot combustion 5 % O_2, 0.2 % NO, 5 % H_2O in Ar, 50 mL min^{-1}	highest catalytic activity achieved for La_2NiCoO_6: 98.2%	the synergistic effect between binary Ni and B' site elements plays a crucial role in enhancing the reduction properties of the catalyst	(Mei et al., 2020)
$LaMnO_3$ SM: reactive grinding Calcination: 600 °C, 24 h, 550 °C, 6 h	SiO_2	methane combustion T: 600 – 680°C Fluidized bed reactor 20% O_2 in He	E_a ($LaMnO_3$): 23 kJ/mol E_a($LaMnO_3$@ SiO_2): 57 kJ/mol	the reduction of Mn^{3+} into Mn^{2+} in $LaMnO_3$@mSiO_2 was more difficult compared to $LaMnO_3$	(Sarshar & Kaliaguine, 2013)
$La_{1-x}K_xFeO_{3-\delta}$ SM: electrospinning & sol-gel Calcination: 700 °C, 2 h		soot combustion 200 mg catalyst with 50 mg soot at 320 °C for 100 min with a 150 ml min^{-1} gas flow of 20% O_2	X(soot): 13%	nanotubes with 20% K^+ doping show the best activity for soot catalytic oxidation	(Fang et al., 2018)
Ca Based Perovskites					
$CaMn_{0.9}Mg_{0.1}O_{3-\delta}$		Methane combustion 500-Wth continuous CLC	for test 9 with ϕ = 3.4: power (Wth) = 1015	Reducing fuel concentration improved combustion efficiency.	(Cabello et al., 2014)

SM: spray drying method Calcination: 1573 K, 4 h PS: +100 μm to +300 μm	T (air reactor): 1223 K T (fuel reactor): 1173 K Reducing gas: 15 vol % CH4	ϕ (oxygen carrier-to-fuel ratio)	Higher ϕ required for near 100% combustion efficiency.	
$CaMn_{0.775}Ti_{0.125}Mg_{0.1}O_{2.9-\delta}$ SM: spray drying method Calcination: 1608 K, 4 h PS: 125 to 200 μm	$\bar{Q}$: 25 L/h reduction stage: 15 vol% CH_4 + 20 vol% H_2O (N_2 balance)	CH_4 conversion 77.6 ± 4% R_O: 8.4-9.0 wt%	Under CLC unit activation conditions, solid requirement for full CH_4 combustion reduced to 160 kg/MWth. Oxygen transport capacity slightly decreased during activation.	(Abad et al., 2020)
C14: $CaMn_{0.9}Mg_{0.1}O_{3-\delta}$ C28: $CaMn_{0.775}Mg_{0.1}Ti_{0.125}O_{3-\delta}$ SM: VITO via spray drying followed by calcination PS: C14: 135 μm, C28: 151 μm	Sweet natural gas dual circulating fluidized bed reactor 120 kWth pilot plant T: 800 °C to 960 °C	Fuel power specific FR inventory mspec,FR: 360 kg/MW (C14) and 320 kg/MW (C28)	Both, C14 and C28 can release about 10 % of the total available oxygen The oxidation state of the OC is linked with oxygen partial pressure in the AR	(Mayer et al., 2018)
$CaMn_{0.9}Mg_{0.1}O_{3-\delta}$ SM: spray drying Calcination: 1300 °C, 4 h	Natural gas Fluidized bed reactors F_{ar} = 200 L_N/min, F_{fr} = 9−12 L_N/min (6.6−8.8 kW), and T_{fr} = 935−955 °C	Real Set-up Y_{CO2}: 0.98 - 1	no inclination towards agglomeration or attrition, while also releasing oxygen at significant levels (exceeding 3% in oxygen concentration)	(Källén et al., 2013)
$CaMn_{0.775}Mg_{0.1}Ti_{0.125}O_{2.9-\delta}$ SM: spray drying Calcination: 1335 °C, 4 h	methane 0.5 kWth CLC unit 15 vol% CH_4 + 20 vol% H_2O (N_2 to balance) T = 900 °C	$R_{OC,t}$ = 0.091 X_r = 0.53	exhibited significant promise in enhancing combustion efficiency at low ϕ values (ϕ < 2) operating at moderate solids circulation rates and maintaining oxygen carrier-to-fuel ratio values, a relatively low attrition rate could be sustained	(Cabello et al., 2021)
$CaMn_{0.775}Mg_{0.1}Ti_{0.125}O_{3-\delta}$ SM: spray drying & calcination	sulfurous fuel (H_2S: 100 – 300 ppmv) dual circulation fluidized bed 120 kWth CLC pilot plant T: 950 °C	X_{CH4}: 98.38 Y_{CO2}: 96.46	continuous long-term operation is not feasible in the presence of substantial quantities of H_2S	(Pachler et al., 2019)
Sr Based Perovskites				
$Sr(Fe_{1-x}Cu_x)O_{3-\delta}$ x = 0, 0.1, 0.33	gaseous fuel T: 600–800 °C Rdn: 3% H_2/Ar	Oxygen capacity @ 600°C highest for $Sr(Fe_{0.67}Cu_{0.33})O_3$: 4.01 wt%	exhibited high temperature stability, with melting temperatures well above 1200 °C and no signs of agglomeration	(Ksepko, 2018)

SM: mechanical mixing calcination method Calcination: 2*(950 °C, 24 h)	Oxdn: 20% O_2/N_2			
$SrFeO_{3-\delta}$ SM: solid-state synthesis method Calcination: 4*(1273 K, 3 h)	Biomass Char Fluidized bed Oxdn: air	oxygen release time: 70 s	Released O_2 at all investigated temperatures Low oxygen capacity per unit mass	(Kwong et al., 2022)
Fe Based Perovskites				
$FeTiO_3$ supplied by Titania A/S W: 15 g PS: 125–180 μm	T: 970 °C $\bar{Q}$ methane or syngas (50% CO, 50% H_2) = 450 mL_n/min flow of 5% O_2 in nitrogen 1000 mL_n/min	Ro: 5.0%	high conversion of CO and moderate conversion of CH_4 showed no tendency of decreased reactivity after 37 cycles or 3 days of experiments.	(Leion et al., 2008)

SM: synthesis method, W: weight of sample, PS: particle size, T: temperature, $\bar{Q}$: Flow Rate, R_O: Oxygen Transfer Capacity, C: Cyclic Stability, η: efficiency, X: Conversion, F: feed

Perovskites in Chemical Looping Reforming (CLR)

Table 2 summarizes the perovskite structures for chemical looping steam and dry methane reforming. The classification in the table is based on the A site and the discussion below follows the same order of the structures provided in Table 2.

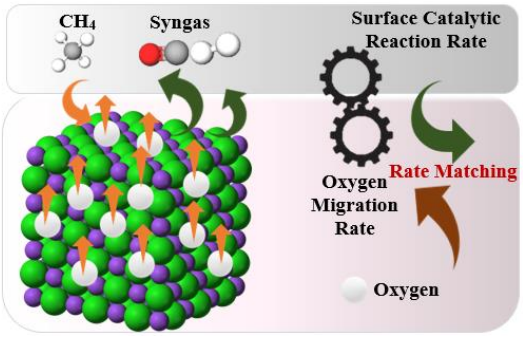

Figure 6: Matching oxygen migration rate with the surface reaction rate to reach high selectivity of syngas in CLRM. Reproduced from Ref. (H.-X. Zhang et al., 2022).

$LaFeO_3$-based structures and the corresponding A and/or B sites substituted, have demonstrated remarkable catalytic activity and exceptional selectivity towards CO/H_2 in CLMR processes. Dai et al (Dai et al., 2016) investigated the reduction kinetics of $LaFeO_3$ oxygen carrier by chemical looping methane reforming and reported the apparent activation energy of about 151 kJ/mol, and the pre-exponential factor of about 4.53×10^4 s^{-1}. He et al, (Zhao et al., 2014) compared the macroporous and nano-$LaFeO_3$ perovskite and reported that the former had a more stable reactivity of methane oxidation and better resistance to carbon formation, which was partially attributed to the higher surface area. It has also been found two kinds of oxygen species to exist on the macroporous $LaFeO_3$ perovskites: surface adsorbed oxygen and bulk lattice oxygen. The highly reactive surface oxygen played a crucial role in completely oxidizing methane to CO_2 and H_2O, while the bulk lattice oxygen primarily facilitated the partial oxidation of methane to H_2 and CO (He, Zhao, et al., 2013), (Shen et al., 2016). $LaFeO_3$ perovskite can also be used for ethane reforming via CLDR, where the main products are syngas, with a few by-products including C_2H_4,

CO and CH_4. Due to its lower C–H bond energy (414 kJ/mol) compared to methane (435 kJ/mol), ethane can be easily activated, allowing for a lower reaction temperature (approximately 100 ◦C lower) to be employed (Ma et al., 2023).

Studies have indicated that the introduction of CeO_2 nanoparticles (2–3 nm) onto macroporous $LaFeO_3$ enhances the generation of oxygen vacancies, resulting in notable improvements in reducibility, oxygen mobility, and resistance to carbon formation (Zheng et al., 2017). On the other hand, the lattice oxygen of $LaFeO_3$ can further be activated by surface modification of NiO, which results in the methane conversion and product selectivity (X. Li et al., 2022). The doping of basic metals such as Ca and Mg has obvious effects on the reactivity of $LaFeO_3$ oxide. The doping of CaO/MgO with $LaFeO_3$ favored the transformation from lattice oxygen into chemisorbed oxygen and formation of oxygen vacancy (Zhao, He, et al., 2016b).

By using DFT calculations, Zhu et al. (Yang et al., 2022) discovered four active ensembles on $LaFeO_{3-\delta}$ including Fe-O_5(ferryl O), Fe-O_5, Fe-O_4(Vo), and Fe-$O_3$$(Vo)_2$, which leads to the reduction of the oxygen carrier in three stages at different active sites with varied Fe coordination environments. At stage(I), the total combustion of methane dominates the overall kinetics on the catalyst surface where Fe is likely to have a Fe-O_5 or a Fe-O_5(ferryl O) coordination environment. At stage(II) which is the major part of the reaction, the Fe-O_4(Vo) ensemble involving an oxygen vacancy is predicted to lead to fully selective methane conversion to CO. At stage(III), carbon deposition would take place at the Fe-$O_3$$(Vo)_2$, leading to the initial stage of deactivation of the catalyst.

Regarding B-site substitution, the use of Co in LaFeO3 for CL-SMR to produce syngas and hydrogen has been widely studied. He et al. (Zhao et al., 2019) observed that the substitution of Co metal does not significantly alter the crystal structure of the double perovskite. However, it

does introduce a certain degree of Fe/Co disorder, leading to the generation of oxygen vacancies and/or higher oxidation states of the metal cations. On the other hand, Zhao et al. (K. Zhao, Y. Shen, et al., 2017) studied the double perovskite oxide LSFCO ($LaSrFeCoO_6$) and observed that its structure and chemical composition return to their original state after steam and air oxidation. However, they noted that Co ions cannot integrate into the double perovskite structure and instead form CoO solely through individual steam oxidation. The synergistic interaction of surface metal ions, specifically (Fe^{4+}/Fe^{5+}-O^{2-}-Co^{2+}) and (Fe^{3+}-O^{2-}-Co^{3+}), has a beneficial impact on methane dissociation. In terms of SRM, the incorporation of Co metal enhances hydrogen production capacity and improves resistance against carbon formation. The deep reduced metals (Fe^{2+} and Co^0) combining with the abundant oxygen vacancies provided enough active sites for the breakage of HO bond of H_2O. The oxygen vacancies were neutralized immediately by the O atom, and the two H atoms combined together to form amounts of H_2. These results suggested that, the positive roles displayed by the synergistic effects between multi-metals in double perovskite structure could effectively promote the partial oxidation of methane and steam splitting (K. Zhao, A. Zheng, et al., 2017). The synergistic effects between Co and Fe in double perovskite $LaSrFe_{2-x}Co_xO_6$ promoted the CH_4 conversion from 50% to ~70% (Zhao et al., 2019). After exposure to CH_4 atmosphere, Zhao et al (Zhao, Shen, et al., 2016) observed the reduction of Fe^{3+} to Fe^{2+}/Fe^0 and the reduction of Co^{3+} to Co^{2+}/Co^0, while La^{3+} and Sr^{2+} maintained their valence states as La_2O_3 and SrO, respectively. As a result, the authors concluded that the La^{3+} and Sr^{2+} ions in A-site did not take part in reaction, but the B-site metals played the key reductive properties role. Similar synergistic interactions has also been reported by other researchers as well (K. Zhao, L. Li, et al., 2017), (Zhao, He, et al., 2016a). In the steam dissociation stage, the combined presence of deeply reduced metals (Fe^{2+} and Co^0) and abundant oxygen vacancies provides active sites for breaking

the H-O bond in H_2O. The oxygen vacancies are quickly neutralized by O atoms, while the combination of two H atoms produces significant amounts of H2. These results highlight the positive synergistic effects of multi-metals in the double perovskite structure, promoting methane partial oxidation and steam splitting.

In terms of A-site substitution, Sr has shown an excellent performance for CLRM (Sastre et al., 2019). LSF perovskites show great potential for advancing sustainable syngas production through alternative cycles of methane partial oxidation and CO_2 splitting. The addition of Sr^{2+} improves the oxygen storage capacity of perovskite materials. This enhancement is attributed to the facilitated reduction of Fe^{4+} to Fe^{3+} in the doped perovskites, leading to improved redox performance. On the other hand, the introduction of Sr^{2+} balances the electronic asymmetry through the oxidation of a portion of Fe^{3+} to Fe^{4+} and/or the formation of oxygen vacancies (He, Li, et al., 2013). The majority of authors (Sastre et al., 2019), (He et al., 2019), (He, Li, et al., 2013) have reported that the optimal $x < 0.5\text{-}0.7$ in $La_{1-x}Sr_xFeO_3$ gives the maximum O_{la}/O_{ad} (O_{la} and O_{ad} stand for lattice oxygen and adsorbed oxygen species, respectively. Coronado et al. (He et al., 2019) found that perovskites with $x \leq 0.3$ Sr exhibited the best results, with syngas yields 3-6 times higher compared to others. Additionally, the selectivity for hydrogen production increased with higher Sr^{2+} content, attributed to the contribution of methane decomposition and the reverse Bourdouard reaction aiding in carbon removal during CO_2 splitting. Cerium is another viable option for substituting the A-site in catalysts. The Ce^{3+}/Ce^{4+} redox pair is recognized for its ability to facilitate H_2O splitting and enhance catalyst durability in this process. Several studies have explored the combination of La and Ce with Fe oxide as redox catalysts for chemical looping methane reforming. Consequently, $La_{1-x}Ce_xFeO_3$ catalysts have demonstrated exceptional stability and superior performance in syngas and hydrogen production (Zhao, Zhang, et al., 2022).

In a series of studies, the activity of $LaMnO_3$ has been explored for SRM (Yang et al., 2021; Yin et al., 2022; Yin et al., 2021a, 2021b; Zheng et al., 2021) as well as DRM (Nalbandian et al., 2011). Substitution of A-site in $LaMnO_3$ with Sr increased the oxygen vacancies which facilitated the migration of oxygen anion in the bulk of the oxygen carrier particles and substitution of B-site with cobalt provided surface active sites to accelerate the activation of methane on the surface (Yin et al., 2022).

Shen et al. (Yin et al., 2021a) studied Al doping in $LaMnO_{3+\delta}$ perovskites. Al substitution increased surface-active sites and improved crystal structure symmetry, facilitating methane activation and oxygen vacancy formation. The CO_2 yield decreased with higher Al doping due to reduced Mn^{4+} and surface absorbed oxygen. Al cations stabilized the crystal structure, preventing perovskite damage. $LaMn_{1-x}Al_xO_{3+\delta}$ ($x \leq 0.5$) showed no carbon formation and achieved prolonged partial oxidation, producing high-quality syngas with an H_2/CO ratio of 2 and pure hydrogen. However, $LaMn_{0.3}Al_{0.7}O_{3+\delta}$ experienced carbon deposition. In another work, the same authors investigated the doping of other metals and reported the improvement with the order of Ni > Co > Fe, due to the addition of active sites and the formation of oxygen vacancies (Yin et al., 2021b). Substitution of A-site with Cu was investigated by Zheng et al. (Zheng et al., 2021), where the authors noted smaller crystal size and cell volume, and better reducibility of $La_{1-x}MnCu_xO_3$ compared with the pure $LaMnO_3$. Moreover, the syngas productivity of $La_{1-x}MnCu_xO_3$ (2.79–5.20 mmol/g) increased gradually with the Cu content in the methane partial oxidation stage. Substitution of A-sites with Fe resulted in a better structural properties, higher surface area and porosity and exhibited a better reactivity and thermal stability, compared to B-site substitution (Yang et al., 2021).

Cu and Mn have also been used for A site modification (Nazari et al., 2023) for SRM, which has been exhibited high sustainability, high X_{CH4}, high Y_{H2}, and low produced carbon content.

Doping Ni provides an effective approach for controlling the surface lattice oxygen vacancies and lattice oxygen migration rate in perovskite oxides. Zheng et al, (Zhao, Fang, et al., 2022) developed A series of novel $CeO_2/La_{0.9}Sr_{0.1}Fe_{1-x}Ni_xO_3$ composite oxide carriers with varying doping ratios of Ni. The authors found that regulation of oxygen vacancies and lattice oxygen in $CeO_2/La_{0.9}Sr_{0.1}Fe_{1-x}Ni_xO_3$ prevents excessive reduction of surface metal ions within the perovskite oxides and the consequent formation of carbon deposits during CL-SRM. Enhanced resistance against coke formation and improved reactivity of CH_4 through Ni doping has also been confirmed by other researcher as well (Oh et al., 2023). Ni doping with $LaAlO_3$ was also found as an effective strategy for DRM (Qi et al., 2022).

Unlike the perovskites discussed earlier in this section, which have primarily been employed for SRM, the $LaNiO_3$ perovskite family has predominantly found application in dry reforming of methane (DRM). The crucial aspect of constructing a dry reforming system revolves around the development of a catalyst with excellent resistance to carbon deposition. Additionally, the catalyst should effectively provide reaction energy to the reactive zone, considering the high endothermic nature of dry reforming. On the other hand, a significant drawback is nickel's propensity to induce carbon formation, leading to catalytic deactivation. Yang et al., (Yang et al., 2015) found that the incorporation of iron into the perovskite structure exhibits robust resistance to carbon deposition. Among the different perovskite catalysts ($La_{0.9}M_{0.1}Ni_{0.5}Fe_{0.5}O_3$, M = Sr, Ca) the authors prepared, the $La_{0.9}Ca_{0.1}Ni_{0.5}Fe_{0.5}O_3$ catalyst displayed the highest level of catalytic performance and superior carbon resistance. To further mitigate carbon deposition, Firoozi et al. (Shahnazi & Firoozi, 2021) explored the incorporation of manganese (Mn) by substituting it into the B-site of $LaNiO_3$ catalysts. This Mn substitution proved highly effective in reducing carbon deposition, leading to a transformation from whisker-like structures to an amorphous form. The observed change was

attributed to the reversible transformation between Mn^{4+} and Mn^{3+}, which resulted in enhanced oxygen mobility within the catalyst.

Brackmann (Bertoldi et al., 2022) investigated the impact of partial substitution of La^{3+} by Ce^{4+} and Sr^{2+} in $LaNiO_3$ (LN). LCN ($La_{1.8}Ca_{0.2}NiO_4$) catalyst showed primary phases of $LaNiO_3$ crystalline structures, while LN catalyst exhibited La_2NiO_4 spinel structure and LSN ($La_{0.95}Sr_{0.05}NiO_3$) catalyst had segregated phases of single oxides. Despite structural differences, LN and LSN achieved methane conversions similar to LCN catalyst (75%). However, LCN catalyst demonstrated the highest CO_2 conversion (32%), compared to LN (21.9%) and LSN (17.1%).

Doping Ni^{2+} at the B sites of other perovskite oxides improves oxygen carrier activity, though it typically leads to methane cracking and carbon deposition. Xian et al (F. Wang et al., 2023) synthesized a series of Ni and Co doped $CeO_2/La_2Ni_{2-x}Co_xO_6$ double perovskite and reported that doping Ni ions increases composite oxygen carrier reactivity with CH_4, while Co and Ni adjustments align lattice oxygen migration and methane activation rates. The authors enhanced the syngas selectivity by tuning the Co/Ni doping ratio. Co-doping of Ni with other metals (e.g. Fe (Zhao, Zhang, et al., 2022) or Ce (Zhao, Zhang, et al., 2022)) has been reported in other research works as well to enhance the methane partial oxidation while suppressing carbon deposition.

Luo et al. (Cao et al., 2023) studied the effects of different preparation methods sol-gel, co-precipitation, hydro-thermal, and solid-state methods) on La_2NiO_4 for DRM. The findings revealed that the sol-gel method resulted in the highest CH_4 and CO_2 conversion rates (91.4% and 91.5% respectively) and exhibited the highest carbon resistance in DRM due to its enhanced microstructure, higher reducibility, and increased basicity. The lowest performance was observed in the sample prepared using the solid-state method, primarily due to the limited presence of

reduced amorphous NiO and the poor reducibility of the perovskite phase. In another work, Lee et al (Lim et al., 2017) investigated the transition of Fe_2O_3–NiO oxides to single $NiFe_2O_4$ and concluded that the transition of mixed oxides to single $NiFe_2O_4$ enhanced syngas yields.

Wang et al, (Wang et al., 2013) synthesized a series of $LaNiO_3$ perovskite catalysts supported on different meso-porous silica (SBA-15, MCM-41 and SiO_2). $LaNiO_3$/MCM-41 displayed the most notable initial catalytic activity attributed to its small Ni particle size. On the other hand, $LaNiO_3$/SBA-15 outperformed the other catalysts in terms of long-term stability. This was attributed to the strong anchoring effect that restricted the migration of nickel clusters.

As per the A-site classification represented in Table 2, $BaCoO_3$ families have also been used mainly for SRM. Just like the previously mentioned structures, sol-gel was found the best method for synthesizing $BaCoO_3$ (Ding et al., 2023). However, it is hard to drive any conclusion due to the limited number of works on this structure. It seems an A-site modification (such as Sr-substitution) is required to enhance the amounts of syngas and hydrogen, and to bring the H_2/CO ratio of syngas closed to the ideal value (D. Cao et al., 2021; Ding et al., 2023; Ding et al., 2019).

$Ca_2Fe_2O_5$ has also been mainly used for CH_4 conversion and CO_2 splitting (CLDRM). Fan et al (Shah et al., 2021) achieved >99% methane conversion with ~98% syngas selectivity and 2:1 H_2:CO ratio using MgO-supported calcium ferrite. The lattice oxygen in the brownmillerite structure of $Ca_2Fe_2O_5$ acts as efficient active sites for CO and H_2 production. Oxygen vacancies significantly reduce energy barriers for C-H cleavage and CO formation, enhancing reactivity and selectivity.

Ce-Zr oxides were used by Chen et al. (Chen et al., 2023) to improve methane conversion and the selectivity of H_2/CO of $Ca_2Fe_2O_5$. However, the reactivity displayed a declining trend with increasing recycling time. In their next work, the authors investigated the lattice oxygen migration

of $Ca_2Fe_2O_5/Zr_{0.5}Ce_{0.5}O_2$ by controlling the reduction and oxidation time. They found that, the complete reoxidation of the reduced structure (40 min) occurred more rapidly than the complete reduction process (160 min). Ce and Sr based perovskites have also been used for DRM in a limited number of works. Chen et al (Chen et al., 2020) demonstrated a high redox performance of a chlorine-doped $SrFeO_{3-\delta}$-CaO nanocomposite in methane-assisted CO_2 splitting. Doping with chlorine promoted methane cracking in the CH_4-POx (partial oxidation of methane) step and improved methane and CO_2 conversions. However, chlorine also increased coke formation, leading to a 3.4-fold increase in coke selectivity during CH_4-POx. Ce-based perovskite in the work by Garcia et al was used as a support for iron oxide. The authors demonstrated the evolution of Fe and Ce oxide, from $Fe_2O_3@CeO_{2-\delta}$ at t=0 sec, to $Fe_3O_4@CeFeO_3$ at t=100 sec and to $Fe@CeFeO_3$. Compared to the mixed oxides of the Ce and Fe ($Fe_2O_3@CeO_{2-\delta}$), $Fe_3O_4@CeFeO_3$ reached a higher hydrogen and carbon monoxide yields. The high carbon deposition potential of metallic Fe^0 limits the enhancement of methane-to-syngas selectivity in chemical looping technology. However, Wang et al (Q. Yang et al., 2023) found that in-situ formation of $CeFe_xAl_{1-x}O_3$ over ceria-hexaaluminate improved carbon resistance. As a result, the recycled ceria-hexaaluminate achieved a high CH_4 conversion rate of approximately 90%, with syngas yield enhancements of 105% and 72% compared to CeO_2-Fe_2O_3-Al_2O_3 oxide and Fe-hexaaluminate, respectively.

Table 2. Perovskite Structures for Chemical Looping Steam and Dry Methane Reforming

Catalyst information	Support	Reaction parameters (vol%)	results	H_2 product	Main findings/conditions	Ref
La Based Perovskites						
$LaFeO_3$ SM: Sol-Gel Calcination: 850 °C, 12 h	CeO_2, ZrO_2 Al_2O_3, SiO_2	Steam Reforming T: 950 °C (CH_4: 50%)	Se (CO): 95%	H_2:CO ratio: 2	The A-site element affected gas production, whereas the B-site element influenced the H2/CO ratio of syngas. CeO_2 not only serves as a source of lattice oxygen for syngas production but also enhanced H_2 production in the RS stage.	(Cao, Luo, Wu, et al., 2022)
$LaFeO_3$ SM: Sol-Gel Calcination: 1173 K for 10 h		Reforming T: 900 °C (CH_4: 11%, O_2:11%)	X(CH_4): 65% Se (CO): 92%		Three models, namely the power–law relation, the shrinking core model, and the nucleation and nuclei growth model, were evaluated to predict the kinetic of CLRM using $LaFeO_3$.	(Dai et al., 2016)
$LaFeO_3$ SM: polystyrene colloidal crystal templating Calcination: 500 °C , 3h, 850 °C, 6 h		Steam Reforming T: 850 °C (CH_4: 40%)	X:(CH_4): 50% Se (CO): 100% Se (H_2): ~80%	H_2:CO ratio: 5-7	Macroporous -$LaFeO_3$ exhibited a better performance for SRM than the nano one.	(Zhao et al., 2014)
$LaFe_{0.7}Co_{0.3}O_3$ SM: polystyrene colloidal crystal templating Calcination: 500, 800, 850 °C		Partial Oxidation T: 850 °C (CH_4: 40%)	X:(CH_4): 91%	H_2:CO ratio: 2	The surface oxygen contributed to the complete oxidization of methane to CO_2 and H_2O The bulk lattice oxygen tended towards partial methane oxidation to H_2 and CO	(He, Zhao, et al., 2013)
$LaFeO_3$ SM: Sol-Gel Calcination: 1000 °C, 12 h		Dry Reforming T: 725-825 °C	@ 775 °C Se (CO): 50% X(C_2H_6): 75% C deposition: 25%	H_2:CO ratio: 1.4	At T<800 C, the conversion of ethane is low, but oxidative dehydrogenation produces ethylene. T >800 C lead to C deposition, so that CO selectivity first increases and then decreases as the T rises.	(Ma et al., 2023)
$LaFeO_3$ SM: modified emulsifier-free emulsion polymerization technique Calcination: 600 °C, 2 h	CeO_2	T: 800 °C (CH_4: 5%)	X(CH_4): 72%	H_2:CO ratio: 10	The coexistence of Ce^{3+} and Fe^{2+} irons induces abundant oxygen vacancies on the mixed oxides	(Zheng et al., 2017)
$LaFeO_3$ enhanced by NiO SM: wet impregnation Calcination: 800 °C, 2 h		Partial Oxidation T: 600-800 °C (CH_4: 40%)	X:(CH_4): 95.2% Se (CO): 82.1%	H_2:CO ratio: 2.5	The lattice oxygen were carriers by surface modification of NiO.	(X. Li et al., 2022)

				The methane conversion and product selectivity mainly depend on the Ni loading.	
$LaFeO_3$ (LF) $LaFeO_3$-CaO (LF-Ca) $LaFeO_3$-MgO (LF-Mg) SM: co-precipitation Calcination: 400 °C, 2 h, 850 °C, 2 h	Steam Reforming T: 850 °C (CH_4: 40%)	X:(CH_4): 93% Se (CO): 100% Se (H_2): 95%	H_2:CO (LF): 7 H_2:CO (LF-Ca): 4 H_2:CO (LF-Mg): 5.5	The addition of CaO/MgO promotes the conversion of lattice oxygen into chemisorbed oxygen and facilitates the formation of oxygen vacancies. LF-CaO sample shows high electron density, enhancing resistance to carbon deposition.	(Zhao, He, et al., 2016b)
$LaFeO_3$ SM: Combustion Calcination: 1173 K for 10 h	Partial Oxidation (CH_4: 45%, O_2: 25%)	X:(CH_4):70-80% Se (CO): 80-90%	NA	Active ensembles on $LaFeO_{3-\delta}$ including Fe-O_5, Fe-O_5, Fe-O_4(Vo), and Fe-O_3(Vo)$_2$, which leads to a 3-step reduction, combustion, conversion and C deposition.	(Yang et al., 2022)
$LaFe_{0.7}Co_{0.3}O_3$ SM: Micro-emulsion Calcination: 500-900 °C, 6 h	Steam Reforming T: 850 °C (CH_4: 40%)	X:(CH_4): 80% Se (CO): 98% Se (H2): 45%	H_2:CO ratio: 2	The sample calcined at 500°C exhibited a surface area of 19.82 m^2/g. The sample calcined at 900°C collapsed and the specific surface a rea reduced to 4.48 m^2/g.	(Shen et al., 2016)
$La_{0.6}Sr_{0.4}FeO_3$ SM: gel formation Calcination: 1400 °C, 4 h	Dry Reforming T: 900 °C (CH_4: 5%, CO_2: 15%)	Se (syngas): 90% Reduction degree: fluidized bed = 72% fixed bed = 50%	H_2:CO ratio: 2 0.6 Nm^3 of syngas per kg of catalyst	C deposition does not deactivate OC Reduction times decrease with T, while oxidation times show a non-monotonic trend. Fluidized-bed tests improved CH4 decomposition control and conversion rates. Fluidized bed tests showed up to 9%w inventory loss due to particle attrition.	(Padula et al., 2022)
$La_{1-x}Sr_xFeO_3$ x: 0; 0.1; 0.3; 0.5; 0.7; 0.9; 1 SM: Modified Pechini Calcination: 1100 °C, 10 h	Steam Reforming T: 850 °C (CH_4: 5%)	$La_{0.9}Sr_{0.1}FeO_3$ X:(CH_4): 85%		The addition of Sr^{2+} improves the oxygen storage capacity of perovskite materials.	(Sastre et al., 2019)
$La_{1-x}Sr_xFeO_3$ x : 0.0, 0.1, 0.3, 0.5, 0.7, 0.9, 1 SM: Combustion Calcination: 500 °C, 3 h 900 °C, 6 h	Steam Reforming T: 850 °C (CH_4: 40%)	X:(CH_4): 80%	H_2:CO ratio: 2	$x \leq 0.3$ Sr exhibited the best results, with syngas yields 3-6 times higher compared to others. The selectivity for hydrogen production increased with higher Sr2+	(He et al., 2019)
$La_{1-x}Sr_xFeO_3$ Calcination: 800-900 °C, 3 h	Steam Reforming T: 800 °C (CH_4: 40%)	X:(CH_4): 80%	X:0.1, H_2:CO ratio: 5	Sr substitution can inhibit methane decomposition in methane reaction.	(He, Li, et al., 2013)

					An optimal range of the degree of Sr substitution is x = 0.3–0.5	
$La_{0.9}Sr_{0.1}FeO_3$ SM: Pechini Calcination: 1100 °C, 10 h	– YSZ	Dry Reforming T: 850 °C (CH_4: 5%, O_2: 5%)	X:(CH_4):30%	H_2:CO ratio: 10 H_2:CO ratio: 2	LSF/YSZ shows significantly better activity, with peak production rates of CO, and H_2. But, the activity of LSF/YSZ materials per cycle is lower than that of unmodified LSF.	(Sastre et al., 2022)
$LaSrFeCoO_6$ Calcination: 1000 °C, 6 h SM: Microemulsion		Steam Reforming T: 400 °C (CH_4:40%, H_2O:0.4%)	Se (H2): 50% X(CH_4): 80%	H_2:CO ratio: 2	Oxidation route (e.g. steam or air) is particularly important. After the oxidation with steam, the Co ion cannot incorporate into the double perovskite structure. The original structure was recovered when the sample oxidized by steam was further oxidized by air.	(K. Zhao, Y. Shen, et al., 2017)
$LaSrFe_{2-x}Co_xO_6$ SM: Microemulsion Calcination: 1000 °C, 6 h		Steam Reforming T: 850 °C (CH_4: 5%)	x:0.2 X:(CH_4): 80% Se (CO): 50% Se (H_2): 55%	H_2:CO ratio: 2	An optimal range of the degree of Co substitution is x = 0.4–0.6 The substitutions of metal Co promoted the CH4 conversion from 50% to ~70%.	(Zhao et al., 2019)
$La_{1.6}Sr_{0.4}FeCoO_6$ SM: Micro-emulsion Calcination: 1000 °C, 6 h		Steam Reforming T: 850 °C (CH_4: 5%)		H_2:CO ratio: 2	The presence of multiple metals concurrently enhances oxygen diffusion. Lattice oxygen migrates from the bulk towards the boundary to participate in the reaction. • The reduced metals within active sites gradually move towards the bulk.	(K. Zhao, A. Zheng, et al., 2017)
$LaSrFeCoO_6$ SM: SG, SSM, ME, Alloy Calcination: 1000 °C, 6 h		Steam Reforming T: 850 °C (CH_4: 40%)	X-SSM(CH_4): 50% X-AA(CH_4): 75% X-SG(CH_4): 75% X-ME(CH_4): 80%	H_2:CO-SSM: 2 H_2:CO-AA: 4 H_2:CO-SG: 3 H_2:CO-ME: 2.5	The reduction of Co^{3+} to Co^{2+} and Co^0, occurred at lower temperatures. The reduction of Fe^{3+} to Fe^{2+} and the partial reduction of Fe^{2+} to Fe^0 took place at higher temperatures.	(Zhao, Shen, et al., 2016)
$La_{1-x}Sr_xFeCoO_6$ (x = 0, 0.2, 0.4, 0.6, 0.8, 1.0) SM: Micro-emulsion Calcination: 500 °C, 2 h 900 °C, 6 h		Steam Reforming T: 850 °C (CH_4: 40%)	$La_{1.6}Sr_{0.4}FeCo$ X:(CH_4): 94% Se (CO): 40% Se (H_2): 40%	H_2:CO ratio: 2.5	Synergistic interactions between Fe^{4+}/Fe^{5+} and Co^{3+}, enhanced the reducibility of oxygen carriers. $La_{0.6}Sr_{0.4}FeCoO_6$ showed superior oxygen transport ability, thermal stability, and hydrogen generation capacity among samples with varying Sr substitution.	(K. Zhao, L. Li, et al., 2017)
$LaFe_{1-x}Co_xO_3$ SM: combustion Calcination: 900 °C, 6 h		Steam Reforming T: 850 °C (CH_4: 40%)	X:(CH_4): 90% Se (CO): 45% Se (H_2): 50%	H_2:CO ratio: 2.5	The optimal degree of Co substitution for achieving optimal oxygen-donation ability, resistance to carbon formation,	(Zhao, He, et al., 2016a)

				and hydrogen generation capacity is x = 0.3.	
$La_{1-x}Ce_xFeO_3$ (x = 0, 0.5, 1) SM: Pechini Calcination: 900 °C, 4 h	Steam Reforming	X:(CH_4): 80% Se (CO): 75% Se (H_2): 90%		Substituting Ce^{3+} at the A site enhanced the surface reactivity during the H_2O splitting process. $La_{0.5}Ce_{0.5}FeO_3$ demonstrated rapid oxygen restoration kinetics during the re-oxidation step.	(Zhao, Zhang, et al., 2022)
$La_{1-x}Sr_xMn_{1-y}Co_yO_{3+\delta}$ Co: 0.4–0.5, Sr: 0.2–0.4 SM: Sol-Gel Calcination: 350 °C, 2 h, 850 °C, 2 h	Steam Reforming T: 900 °C	$La_{0.8}Sr_{0.2}Mn_{0.5}Co_{0.5}O_{3+\delta}$ X(CH_4): 70% Se (CO): 90%	H_2:CO ratio: 3.2	The inclusion of cobalt introduced active sites on the surface, promoting the activation of methane. Sr doping increased the presence of oxygen vacancies, facilitating the migration of oxygen anions within the bulk of the oxygen carrier particles.	(Yin et al., 2022)
Al doped $LaMnO_{3+\delta}$ $x \leq 0.5$ SM: Sol-Gel Calcination: 850 °C, 2 h	Steam Reforming T: 850 °C (CH_4: 5%)	Se (CO): 87%	H_2:CO ratio: 3.5	Doping with Al enhances selective oxygen release. $LaMn_{1-x}Al_xO_{3+\delta}$ ($x \leq 0.5$) exhibits high resistance to carbon deposition. $LaMn_{1-x}Al_xO_{3+\delta}$ ($x \leq 0.5$) enables prolonged partial oxidation.	(Yin et al., 2021a)
$LaMn_{1-x}B_xO_{3+\delta}$ (B = Fe, CO and Ni) SM: Sol-Gel Calcination: 850 °C, 2 h	Steam Reforming T: 850 °C (CH_4: 5%)	$LaMn_{1-x}Co_xO_{3+\delta}$ Se (CO): 85%	H_2:CO ratio: 8	Fe, Co, and Ni in $LaMnO_{3+\delta}$ enhanced the migration of oxygen ion. Fe, Co, and Ni doping increased yields of syngas and hydrogen. The improvement effect was in the order of Ni > Co > Fe.	(Yin et al., 2021b)
$La_{1-x}MnCu_xO_3$ (x = 0, 0.05, 0.1, 0.15, 0.2) SM: Sol-Gel Calcination: 800 °C, 2 h	Steam Reforming T: 900 °C (CH_4: 5%)	X:(CH_4): 30-55% Se (CO): 80%	H_2:CO ratio: 2	$La_{1-x}MnCu_xO_3$ exhibited smaller crystal size and cell volume, and better reducibility compared with the pure $LaMnO_3$. The syngas productivity of $La_{1-x}MnCu_xO_3$ increased with the Cu content.	(Zheng et al., 2021)
$La_{0.85}MnFe_{0.15}O_3$ (LMF) SM: Sol-Gel Calcination: 700-850 °C, 2 h	Steam Reforming T: 700-850 °C (CH_4: 5%)		H_2:CO ratio-800: 2 H_2:CO ratio-850: 1.7	The LMF series displayed superior structural and porous properties. Among them, LMF-800 showcased the highest reactivity and thermal stability. The samples subjected to calcination at 800 °C exhibited an increased concentration of oxygen vacancies and improved oxygen mobility.	(Yang et al., 2021)
$La_{1-x}Sr_xM_yFe_{1-y}O_3$ (M = Ni, Co, Cr, Cu) SM: Sol-Gel	Dry Reforming Pulse, 1000 °C		Y-H_2 (POx): 90%	Small quantities of NiO, increases the methane decomposition and selectivity towards CO and H_2.	(Nalbandian et al., 2011)

Calcination: 1000 °C, 6 h					The CH_4 conversion was in the order of Ni > Cr > Cu> Fe> Co. The CH_4 conversion was in the order of Cr > Cu> Fe> Co> Ni.	
$Cu_xMn_{1-x}Fe_2O_4$ (x = 0.3, 0.5, 0.6, and 0.7) SM: Co-precipitation Calcination: 500 °C, 6 h		Steam Reforming	X(CH_4): 98.7%	Y(H_2): 83%	The association of Cu, Mn, and Fe in the spinel ferrite structure results in high sustainability, XCH4, YH2, and low carbon content on the OC..	(Nazari et al., 2023)
$La_{1-y}Ca_yNi_{0.9}Cu_{0.1}O_3$ SM: Sol-Gel Calcination: 750 °C, 1 h, 900 °C, 6 h		Steam Reforming T: 850 °C (CH_4: 10%)	X:(CH_4): 80%	H_2:CO ratio: 2	The reactivity of the $La_{1-y}Ca_yNi_{0.9}Cu_{0.1}O_3$ is improved as the calcium substitution increases.	(Jiang et al., 2019)
$La_{0.9}Sr_{0.1}Fe_{1-x}Ni_xO_3$ SM: Sol-Gel Calcination: 400 °C, 2 h 850 °C, 6 h	CeO_2	Steam Reforming T: 850 °C (CH_4: 40%)	Se (H_2): 88% (LSN) X:(CH_4): 90%	H_2:CO ratio: 2	The Ni doping in the B-site increased their reactivity with methane. The substitution of La by Sr in A site improves the syngas selectivity via adjusting the migration rate of lattice oxygen.	(Zhao, Fang, et al., 2022)
Ni(0.5) Ni(2.5) Ni(10.0)	$La_{0.9}Ca_{0.1}AlO_{2.95}$ SM: Sol-Gel Calcination: 450 °C, 5 h	Dry Reforming CH_4:CO_2:Ar = 1:1:2	X:(CH_4): 60% X:(CH_4): 73% X:(CH_4): 79%		The initial activity followed the sequence of Ni(10.0) > Ni(2.5) > Ni(0.5), whereas the Ni(2.5) catalyst exhibited the best stability	(Qi et al., 2022)
xCuO/ $La_{0\cdot7}Sr_{0\cdot3}FeO_3$ (LSF) x: 0,2,5,10,15 SM: Sol-Gel Calcination: 900 °C, 4 h		Partial Oxidation T: 750 °C (CH_4: 40%)	X_{LSF}:(CH_4):65% $X_{Cu\text{-}LSF}$:(CH_4):80%	H_2:CO_{LSF}: 3.5-4 H_2:$CO_{Cu\text{-}LSF}$: 2.5-3.5	The CuO and KSF interaction played a vital role in oxygen carriers. CuO modification improved methane dissociation and activation of lattice oxygen. 10CuO/$La_{0\cdot7}Sr_{0\cdot3}FeO_3$ showed good reactivity and regenerability.	(Zhang et al., 2020)
Ni-Co doped $La_{0.6}Ca_{0.4}FeO_{3-\delta}$ SM: Sol-Gel Calcination: 900 °C, 5 h		T: 850 °C (CH_4: 5%, CO_2:5%)	X-Ni:(CH_4):73% X-Co:(CH_4):65%	H_2:CO(Ni):1.4 H_2:CO(Co):1	https://doi.org/10.1016/j.apcatb.2023.122745 The inclusion of Ni and Co in the sample led to enhanced resistance against coke formation and improved reactivity of CH_4.	(Oh et al., 2023)
$La_{1.6}Sr_{0.4}FeCoO_6$ (LSFC) (doped with Mg/Li/bare) SM: Sol-Gel Calcination: 1000 °C, 8 h		Reforming T: 800-900 °C (CH_4: 37%, CO_2:5%)	X-Mg:(CH_4):90%	H_2:CH_4(Mg):1.6	Mg doping enhances the migration rate of lattice oxygen. LSFC doped with Mg demonstrates excellent reactivity and stability. The potential reaction mechanism involves both methane cracking and oxidation.	(Li et al., 2019)

Fe-substituted $LaCoO_3$ SM: modified Pechini Calcination: 450 °C, 4 h, 900 °C, 6 h		Steam Reforming T: 700 °C	X(CH_4): 92%	H_2:CH_4(Mg):2.2	$LaCo_{0.6}Fe_{0.4}O_3$ showed the highest H_2 purity and yield at 700 °C. Fe substitution enhanced hydroxide adsorption and decomposition, while increasing CO selectivity by reducing lattice oxygen transfer to the surface.	(Lee et al., 2020)
MeO_x@$La_ySr_{1-y}FeO_3$ Me: Co, Mn, Fe SM: Pechini Calcination: 450 °C, 4 h, 950 °C, 8 h		Partial oxidation T: 950 °C, 8h (CH_4: 10%, O_2:10%)	Se-Co(CO): 62% Se-Co(CO): 88% Se-Co(CO): 82%	H_2 (POx): 33% H_2 (POx): 71% H_2 (POx): 84%	Mn and Co oxides were used as core in a MeOx@LSF core-shell structure. The selectivity and formation of coke depend on the core material.	(Neal et al., 2015)
$La_{1-x}Sr_xM_yFe_{1-y}O_3$ (M = Ni, Co, Cr, Cu) SM: Sol-Gel Calcination: 1000 °C, 6 h		Dry Reforming Pulse, 1000 °C	X-Ni:(CH_4):75% X-Cr:(CH_4):78% X-Cu:(CH_4):78% X-Fe:(CH_4):60% X-Co:(CH_4):50%	Y-H_2 (POx): 40% Y-H_2 (POx): 60% Y-H_2 (POx): 55% Y-H_2 (POx): 50% Y-H_2 (POx): 35%	Small quantities of NiO significantly increased methane decomposition and selectivity towards CO and H_2. Mechanically mixing NiO with the perovskites yields different results compared to adding Ni to the perovskite crystal structure.	(Nalbandian et al., 2011)
La_2NiO_4 (LN) $La_{1.8}Ca_{0.2}NiO_4$ (LCN) $La_{1.8}Ba_{0.2}NiO_4$ (LBN) $La_{1.8}Ca_{0.1}Ba_{0.1}NiO_4$ (LCBN) SM: MW-combustion Calcination: 900 °C, 2 h		Steam Reforming T: 950 °C (CH_4: 15%, H_2O: 20%)	R_O: 4.12 R_O: 4.47 R_O: 2.41 R_O: 3.44	H_2:CO ratio: 1.10 H_2:CO ratio: 0.93 H_2:CO ratio: 0.95 H_2:CO ratio: 0.87	Ni-based double perovskites did not present oxygen decoupling property. LBN was less reactive than the others due to its greater stability LCN showed good reactivity and high recovery capacity	(Medeiros et al., 2020)
$LaFe_{1-x}Ni_xO_3$ (x: 0.05, 0.1, 0.15, 0.2, 0.25, 0.3) SM: polystyrene colloidal crystal templating Calcination: 500 °C, 3 h		Steam Reforming T: 850 °C (CH_4: 5%)	x:0.05, 0.1, 0.15 X:(CH_4): 85%	H_2:CO ratio: 2.8	Ni substitution improved the oxygen supply capacity. Ni substitution increased the dissociation of methane and coke deposition.	(Shen et al., 2019)
La_2NiO_4 SM: Sol-Gel, SSM, CP, HT Calcination:		Dry Reforming T: 850 °C (CH_4: 7%)	X(CH_4): 91.4% X(CO_2): 91.5%		Sol-gel method exhibited the highest carbon resistance. The lowest performance was observed in the sample prepared using the solid-state method	(Cao et al., 2023)
$LaNiO_3$ Calcination: 700 °C, 6 h	SBA-15, MCM-41, silica	Dry Reforming T: 700 °C CH_4:CO_2 = 1:1	X(CH_4): 75%	H_2:CO ratio: 1.1	$LaNiO_3$/MCM-41 demonstrated superior initial catalytic activity due to its enhanced Ni dispersion. $LaNiO_3$/SBA-15 exhibited superior long-term stability compared to $LaNiO_3$/MCM-41.	(Wang et al., 2013)
Fe_2O_3–NiO/$La_{0.8}Sr_{0.2}FeO_3$		Dry Reforming T: 900 °C	X(CH_4): 97%	H_2:2*CH_4 ratio: 0.9	Transitioning from mixed Fe_2O_3-NiO oxides to single $NiFe_2O_4$ enhances	(Lim et al., 2017)

Calcination: 400 °C, 2 h SM: modified Pechini		(CH_4: 25%, CO_2: 25%)			syngas yields, while also improving carrier activity and stability over repeated cycles.	
$La_{0.9}M_{0.1}Ni_{0.5}Fe_{0.5}O_3$ (LNF) (M = Sr, Ca) Modified EDTA-cellulose method Calcination: 550 °C, 5 h		Dry Reforming T: 900 °C CH_4:CO_2 = 1:1	X-LNF(CH_4): 84.2% X-SrLNF(CH_4): 92% X-CaLNF(CH_4): 90%	H_2:CO ratio: 0.6 H_2:CO ratio: 0.8 H_2:CO ratio: 0.8	C deposition is a challenge in $LaNiO_3$ families during DRM. Fe insertion in the perovskite structure has strong resistance to carbon formation. The basicity of catalysts was changed by partial substitution of A site either by Ca or Sr and prevented metal sintering.	(Yang et al., 2015)
$LaNi_{1-x}Mn_xO_3$ 0<x<1 SM: Ultrasonic spray pyrolysis Calcination: 800 °C, 4 h		Dry Reforming T: 800 C CH_4: CO_2: N_2 1: 1: 2	X (CH_4): 90% X (CO_2): 80-90%	H_2:CO ratio: 1.05	https://doi.org/10.1016/j.jcou.2021.101455 C deposition is a challenge in $LaNiO_3$ families during DRM. Mn-substituted catalysts greatly reduced carbon deposition and transformed its morphology from whiskers to amorphous.	(Shahnazi & Firoozi, 2021)
$LaAl_{0.25}Ni_{0.75}O_3$ (LANO) Si-doped-$LaAl_{0.25}Ni_{0.75}O_3$(LANO-Si) Calcination: 750 °C, 4 h		Dry Reforming T: 800 °C CH_4:CO_2:N_2 1:1:2	X_{LANO}:(CH_4):82% X_{LANO}:(CO_2):82% $X_{LANO-Si}$:(CH_4):65% $X_{LANO-Si}$:(CO_2):6%		Mesoporous perovskite catalyst was synthesized using SBA-15 as template. Si doping enhanced Ni-support interaction, inhibiting Ni particle sintering.	(Ruan et al., 2020)
$La_{0.95}Ce_{0.05}NiO_3$ (LCN) $La_{0.95}Sr_{0.05}NiO_3$ (LSN) Modified Pechini's Calcination: 800 °C, 5 h		Tri-Reforming CH_4:CO_2:H_2O:O_2 1:0.5:0.25:0.5 M	Se (H_2): 55% (LCN) Se (H_2): 62% (LSN) X:(CH_4): 75%	H_2:CO ratio: 1.2 H_2:CO ratio: 1.5-1.6	https://doi.org/10.1016/j.ijhydene.2022.07.053 LCN demonstrates the quickest attainment of steady state. LSN facilitates interactions between strontium phases and coke. $La_{0.95}Ce_{0.05}NiO_3$ exhibits higher CO_2 conversions compared to the other catalysts. The order of H_2/CO molar ratio is LN ≈ LSN > LCN.	(Bertoldi et al., 2022)
$La_2Ni_{2-x}Co_xO_6$ SM: Sol-Gel Calcination: 850 °C, 3 h	CeO_2	Steam Reforming T: 850 °C	Se (syngas): 95% X(CH_4): 86%	H_2:CO ratio: 2	Co introduction increases surface active sites, accelerating CH_4 activation. Ni addition promotes oxygen vacancy formation for lattice oxygen migration.	(F. Wang et al., 2023)
Ni/$LaAlO_3$ Ni/$La_{0.8}Mg_{0.2}AlO_{2.9}$ (N/LMA) SM: Sol-Gel Calcination: 450 °C, 5 h		Dry Reforming T: 700 °C CH_4:CO_2 = 1:1	X(CH_4): 70% X(CO_2): 80%	H_2:CO ratio: 0.8 H_2:CO ratio: 0.9	The N/LMA catalyst exhibited better performance compared to the Ni/LaAlO3 catalyst. Mg substitution resulted in the formation of smaller Ni nanoparticles.	(Bai et al., 2021)

					Mg substitution increased the both basic sites and oxygen vacancies.	
$La_{0.95}Ce_{0.05}Ni_xFe_{1-x}O_3$ (LCNF) (x = 0, 0.2, 0.5, 0.8, 1.0)		Steam Reforming	x:0.2, X(CH_4): 95% x:0.5, X(CH_4): 89%	H_2:CO ratio: 2	LCNF with x: 0.2 and 0.5 reached a higher syngas selectivity accompanying with good methane conversion (93.1% and 95.7%). The proper amount of Ni doping forming the Ni Fe synergetic effects also contributed highly to methane partial oxidation.	(Zhao, Zhang, et al., 2022)
$La_{1-x}Ce_xFeO_3$ (x = 0, 0.5, 1) SM: Sol-Gel Calcination: 900 °C, 4 h		Steam Reforming	X:(CH_4): 80% Se (CO): 75% Se (H_2): 90%		https://doi.org/10.1016/j.ces.2020.115707 Substituting Ce^{3+} at the A site enhanced the surface reactivity during the H_2O splitting process. $La_{0.5}Ce_{0.5}FeO_3$ demonstrated rapid oxygen restoration kinetics during the re-oxidation step.	(Zhao, Zhang, et al., 2022)
Ba Based Perovskites						
$BaCoO_{3-\delta}$ perovskite SM: Sol-Gel Calcination: 850 °C, 5 h	CeO_2	Steam Reforming T: 850 °C (CH_4: 50%)	Se(H_2): 2 Se(CO): 1	H_2:CO ratio: 2	The co-sol-gel sample contained impurities (Co_3O_4, $BaCO_3$, and $BaCeO_3$) that reduced the reaction capacity and promoted secondary methane decomposition. This resulted in an excessive H_2/CO ratio in the syngas and the formation of coke.	(Ding et al., 2023)
$Ba_{1-x}Sr_xCoO_{3-\delta}$ SM: Impregnation Calcination: 400 °C, 30 min	CeO_2	Steam Reforming (CH_4: 50%)	Se(CO): 90% Se(H_2): 125%	H_2:CO ratio: 2	A series of cordierite (honeycomb ceramics) monolith reactors coated with $Ba_{1-x}Sr_xCoO_{3-\delta}/CeO_2$ was prepared. the introduction of cordierite could inhibit the methane pyrolysis and the carbon deposition in the later stage during the partial oxidation	(D. Cao et al., 2021)
$Ba_{1-x}Sr_xCoO_{3-\delta}$ SM: Sol-Gel Calcination: 850 °C, 5 h	CeO_2	Steam Reforming (CH_4: 50%)	Se(H_2): 85% Se(CO): 90%	H_2:CO ratio: 2	The combined influence of A-site elements (Ba/Sr) and CeO_2 boosted the reactivity of $Ba_{1-x}Sr_xCoO_{3-\delta}/CeO_2$. The partial sintering of $Ba_{1-x}Sr_xCoO_{3-\delta}$ perovskite improved the oxygen movement within $Ba_{1-x}Sr_xCoO_{3-\delta}/CeO_2$.	(Ding et al., 2019)
Ca Based Perovskites						
$Ca_2Fe_2O_5$ SM: solid-state Calcination: 1150 °C, 10 h	MgO	Dry Reforming (CH_4: 10%, CO_2: 40%)	X(CH_4): 99.88%	H_2:CO ratio: 2.03	$Ca_2Fe_2O_5$ oxygen carriers outperform Fe2O3 in syngas production. The utilization of $Ca_2Fe_2O_5$ results in a higher thermodynamic conversion of	(Shah et al., 2021)

					CO_2 when oxidizing the reduced samples.	
$Ca_2Fe_2O_5/Zr_{0.5}Ce_{0.5}O_2$ SM: Sol-Gel Calcination: 1000 °C, 10 h		Dry Reforming T: 850 °C (H_2: 10%, CO_2: 10%)	-	H_2: 99.88%	Ce-Zr oxides enhanced the methane conversion and the selectivity of H_2/CO in $Ca_2Fe_2O_5$. The reactivity declined with increasing recycling time	(Chen et al., 2023)
$Ca_2Ni_xFe_{2-x}O_5$ (x = 0, 0.25, 0.5, 0.75, 1) SM: Sol gel method Calcination: 1000 °C, 10 h	MgO	Toluene Reforming T: 900 °C Toluene: 0.01 ml/min Steam: 0.01 ml/min	Se (syngas): 66.88% Se (H_2): 82.41%	Y (Syngas): 1.06 Nm^3/L Y (H2): 2.13 Nm^3/L	Ni doping enhances the redox activity of lattice O_2 Ni-doping causes the energy of oxygen vacancy formation and bulk oxygen migration to reduce Ni doping perturbs the electronic structures of the transition metal oxides	(Xu et al., 2023)
Sr Based Perovskites						
$SrFeO_{3-\delta}$-$Ca_{0.5}Mn_{0.5}O$ SM: Sol gel method Calcination: 1000 °C, 6 h		Partial Oxidation CH_4 T: 850, 900, 950	X(CH_4)-850: 6.7% X(CH_4)-900: 6.0% X(CH_4)-950: 4.1%	Y(H_2): 4 mmol/g Y(CO): 2 mmol/g (@900 °C)	Strontium ferrite nanocomposite was synthesized in the form of reticulated foam, rather than powder, for solar driven CLMR. The foam exhibits a higher solar-to-fuel efficiency (5.68% vs. 4.68%)	(Wang et al., 2022)
Chloride-promoted $SrFeO_{3-\delta}$ (SFO-CA) $SrFeO_{3-\delta}$-CaO (SFOC-CA) SM: Pechini method Calcination: 1200 °C, 12 h		Dry Reforming T: 980 (CH_4: 4%, CO_2: 5%)	X(CH_4)-SFO-CA: 78% X(CH_4)- SFOC-CA: 88%		Chlorine promotes coke formation. Tailored window both suppresses complete oxidation and enhances CH_4 and CO_2 transformations.	(Chen et al., 2020)
Ce Based Perovskites						
Fe_2O_3 Fe_3O_4 Fe SM: Sol gel Pechini method Calcination: 900 °C, 1 h	CeO_{2-x} $CeFeO_3$ $CeFeO_3$	Dry Reforming T: 900 (CH_4: 10%)		H_2:CO ratio< 2 H_2:CO ratio: 2 H_2:CO ratio> 2	https://doi.org/10.1016/j.catcom.2021.106356 The activity of Fe/Ce mixed oxides can be adjusted by controlling the Fe_2O_3/CeO_2 mass ratio, initial oxidation state, and reaction time. Compared to Fe_2O_3@$CeO_{2-\delta}$, Fe_3O_4@$CeFeO_3$ reached a higher hydrogen and carbon monoxide yields.	(García-García & Metcalfe, 2021)
$CeFe_xAl_{1-x}O_3$ (CFA) SM: co-precipitation Calcination: 900 °C, 4 h		Dry Reforming (CH_4: 5%)	X(CH_4): 70-85%	H_2:CO ratio: 2.2	https://doi.org/10.1016/j.apcatb.2023.122636 CeFexAl1−xO3/Fe0/Ba-hexaaluminate improved carbon resistance	(Q. Yang et al., 2023)

							CFA formed through CeO_2-Fe-Al interaction in hexaaluminate. Metallic Fe0 from Fe-hexaaluminate facilitated CH_4 activation. CFA exhibited high oxygen ion conduction.

Rd: Reduction, Ox: Oxidation, Se: Selectivity, OC: Oxygen Carrier, Y: Yield, Conversions: X, SSM: Solid State Method, CP: co-precipitation method, HT: hydrothermal method, SG: sol-gel method, C: Carbon, T: Temperature

Perovskites in Chemical Looping Gasification (CLG)

Table 3 summarizes the perovskite structures for chemical looping gasification. La-based perovskites, especially $LaFeO_3$, have gained significant attention in recent years ((Yan et al., 2023), (Shen et al., 2022)). In terms of A-site modification, the effects of the Ba-substitution in lanthanum ferrites were investigated by Yan et al. (Yan et al., 2021), who found that $La_{0.3}Ba_{0.7}FeO_3$ (L3B7F) performed best compared with $LaFeO_3$ (LF) and $LaFe_{0.5}Ni_{0.5}O_3$ (LN5F5), provided the maximum syngas output, carbon conversion, and gasification efficiency. In terms of B-site modification, Shen et al. (Shen et al., 2019) partially substituted Fe with Mn, Co, Ni, and Cu and reported that the oxygen releasing capacity increasing in the following order: LaFeCu > LaFeCo > LaFeNi > LaFeMn > LaFe. A similar trend has also been reported by Li et al, LaFeCu > LaFeCo > LaFeNi > LaFeCr > LaFe.

Gasification processes are usually applied to coal, lignite, biomass, and wastes, but could be applied to microalgae as well with economic constraints. Due to their increased output, quicker development, and higher photosynthetic efficiency, microalgae are particularly appealing among these fuels (Yan et al., 2023). However, because microalgae have a high nitrogen content, the emission of nitrogen-containing chemicals like NO_x and its precursors (HCN and NH_3) is becoming a serious environmental problem during the thermochemical conversion of microalgae (Yan et al., 2023). This challenge is a major focus of many CLG process using La-based perovskites. Similar to CLC, thermal and rapid NO_x generation during CLG was significantly minimized by the gasifier's comparatively low temperature (1000 ºC) and nitrogen-free environment (Wang et al., 2021).Yan et. al (Yan et al., 2023) proposed a possible evolution pathway of gas-N during CLG of microalgae over $La_{0.3}Ba_{0.7}FeO_3$ (L3B7F). They found that the L3B7F has the capacity to reduce tar and NO_x synergistically at high temperatures (>700 °C) and

to store NO_x on its surface at moderate temperatures (400 °C). To improve the oxygen releasing ability of $LaFeO_3$, various studies have been conducted by substituting the B-site metal ions. According to Zhang et al., (Zhang et al., 2006) the B-site doping could significantly increase the conversion of NO to N_2, and $LaMnO_3$ perovskite had a noticeable catalytic impact on the synergistic removal of NO and C_3H_6. Additionally, the doped La-Fe-O series perovskites were evaluated, and the yield of N_2 over $LaFe_{0.8}Cu_{0.2}O_3$ reached around 97 % at 700 °C. Shen et. al. (Zhang et al., 2006) revealed that lanthanum manganite's initial oxygen vacancy count grew and that, following Cu doping ($LaMn_{1-x}Cu_xO_3$) , the link between metal and oxygen deteriorated, which enriched surface absorption oxygen and improved lattice oxygen release. However, the increased α-oxygen content expedited the non-selective oxidation of hydrocarbons while inhibiting the creation of organo-nitrogen compounds. As a consequence, the N_2 yield in comparison to Mn-based perovskites was adversely affected, resulting in poor performance. Co-doping at the B-site also improves the reactivity and inhibits carbon formation of chemical looping reaction (Zhao, He, et al., 2016a). Wang and Shen (P. Wang et al., 2023) proposed $La_{1-x}Ca_xFeO_3$ perovskites (x = 0, 0.1, 0.2 and 0.3) as possible catalysts for NH_3 selectivity promotion in biomass gasification. Ca^{2+} has a smaller ionic radius than La^{2+}, is a more basic element and can act as a promoter for the formation of active sites on the surface of the catalyst. The results indicate that $La_{0.8}Ca_{0.2}FeO_3$ possessed the highest conversion of nitrogen into NH_3 (62.2 wt%). It also showed superior stability, with a conversion of nitrogen into NH_3 of 58.4 wt% after 100 h of reaction.

Several studies have also been conducted on Ca-based perovskite structures ((Hu et al., 2020), (Liu et al., 2019a), (Liu et al., 2019b)). Compared to the gasification process of rice husk char without $CaMn_{0.6}Fe_{0.4}O_3$, Liu et al. found that the $CaMn_{0.6}Fe_{0.4}O_3$ structure serves the roles of both oxygen carrier and catalyst with greater H_2/CO and low energy consumption (C. Liu et al., 2018). The

performance of the oxygen evolution reaction can be increased by proper Mn-doping due to the increase in d-spacing, which resulted in more high-charge Mn ions and better oxygen-ion migration and oxygen activation (Liu et al., 2023). $CaFe_2O_4$ and $Ca_2Fe_2O_5$ have been found by Zhang et al. (Zhang et al., 2017) to have a gasification efficiencies of 89.21% and 92.49% respectively. Sun et. al. (Sun et al., 2018) explored three calcium ferrite catalysts (CaO-$Ca_2Fe_2O_5$, $Ca_2Fe_2O_5$, and $CaFe_2O_4$) for gasifying pine wood and increasing H_2-rich syngas yields. As a consequence of its continuous promoting mechanism and considerable redox durability, the results indicated that $Ca_2Fe_2O_5$ is a viable catalyst for large-scale biomass conversion applications. On the other hand, Liu et. al (Liu et al., 2023) revealed a clear reaction pathway for $Mn/Ca_2Fe_2O_5$ perovskites in CLG of biogas residue that involved oxygen uncoupling, CO_2 catalytic conversion, the regeneration of oxygen uncoupling vacancy and finally recoverable oxygen uncoupling (Figure 7).

Ba containing oxygen carriers among various composite metal oxides demonstrated great performance in CLG process (Sun, Xiao, et al., 2022). Chen et. al (Chen et al., 2019) explored the

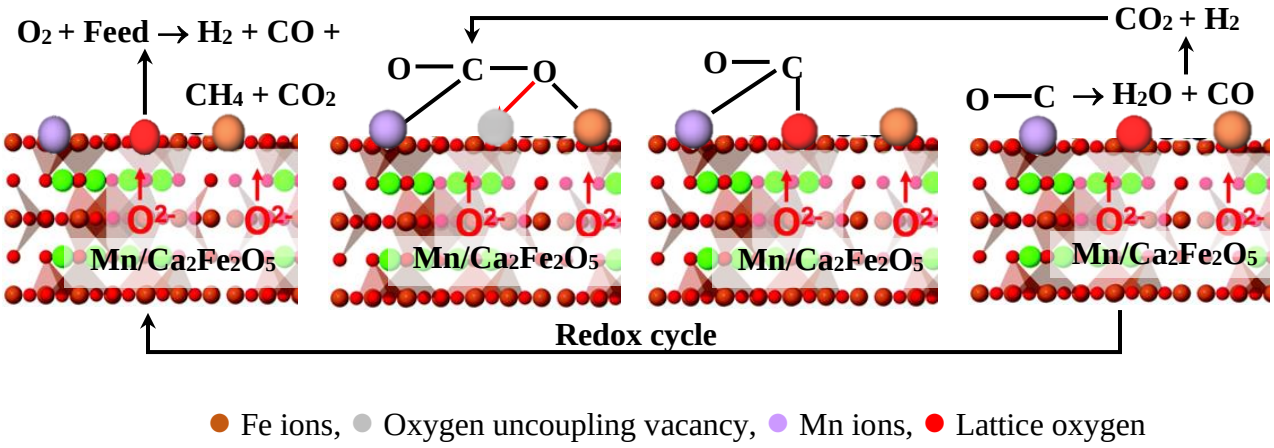

Figure 7: Reaction mechanism model for CLG over Mn/Ca2Fe2O5 OCs. Reproduced from Ref. (Liu et al., 2023).

reactivity of $BaFe_2O_4$ in CLG and discovered that it is a potential catalyst for the production of

H_2-rich syngas because of its continuous promoting mechanism, strong redox durability, and high hydrogen output. Yan et. al. (Yan et al., 2020) studied the reaction mechanism between carbon and barium ferrite. They concluded that $BaFe_2O_4$ is a potential OC for gasification with generation of hydrogen-rich syngas and removal of tar. Siriwardane et. al. studied $BaFe_2O_4$ as oxygen carriers in CLG of coal and proved that when these oxygen carriers were present during the steam gasification, the rate of gasification and selectivity for the formation of synthesis gas were much increased (Siriwardane et al., 2016).

Table 3. Perovskite Structures for Chemical Looping Gasification

Catalyst information	Reaction parameters	Cycles	results	Main findings/conditions	Ref
Ca Based Perovskites					
$Ca_2Fe_2O_5$ SM: wet impregnation Calcination: 800 °C, 4 h W: 1 g PS: 0.090–0.212 mm	CLG temp: 600 - 900 °C Fuel: Rice straw Packed bed	3 c	Hydrogen yield (at optimal temperature of 800 °C) = 63.20 %	Improving cyclic durability of $Ca_2Fe_2O_5$ can enhance its suitability for chemical looping gasification of biomass. CLG cyclic performance decreases due to Si accumulation from biomass ash destroying Fe-Ca structure.	(Hu et al., 2020)
$Ca_{1.4}Sr_{0.6}Fe_2O_5$ SM: sol-gel method Calcination: 600 °C, 2h, 900 °C, 5 h PS: > 200 μm	CLG temp: 850 °C Fuel: microalgae Packed bed	10 c	H_2 (%) = 48.7 CO (%) = 29.5 CO_2 (%) = 11.6	Sr-doping in low is a great method for enhancing the reactivity of $Ca_2Fe_2O_5$ as OC in microalgae CLG.	(Liu et al., 2019a)
$Ca_2Fe_{1.8}Co_{0.2}O_5$ SM: sol-gel method Calcination: 600 °C, 2 h 900 °C, 5 h	CLG temp: 850 °C Fuel: microalgae Packed bed	10 c	η Gasification (without steam): 66.80% η Gasification (with steam): 91.14 %	Cobalt substitution for Fe improves the activity of oxygen carriers, but excess Cobalt tends to complete oxidation	(Liu et al., 2019b)
$Mn/Ca_2Fe_2O_5$ SM: sol-gel method Calcination: 900 °C, 4 h PS: < 200 μm	CLG temp: 800 °C Fuel: biogas solid residues Reactor: tube furnace		The gasification efficiency: 72.31% and Carbon conversion efficiency: 95.72%	The reaction mechanisms of are due to the oxygen uncoupling ability achieving gas–solid reaction.	(Liu et al., 2023)
$CaFe_2O_4$ SM: sol-gel method Calcination: 900 °C, 4 h	CLG temp: 800 °C Fuel: coal Reactor: fixed bed	5 c	Syngas selectivity: 0.9 Carbon conversion up to 90 %	Only interacts with coal, which makes it simpler to keep the reaction going throughout the gasification step to create syngas. Wyodak coal and $CaFe_2O_4$ seemed to be a synergistic combination of steam and oxygen carriers.	(Siriwardane et al., 2016)
$CaFe_2O_4$ $Ca_2Fe_2O_5$ SM: combustion calcined at 900 °C for 5 h PS: < 200 μm	CLG temp: 850 °C Fuel: microalgae Reactor: fixed bed		Gasification efficiency (%) $CaFe_2O_4$ 89.21 $Ca_2Fe_2O_5$ 92.49	Calcium ferrites would be reduced by the step of $CaFe_2O_4 \rightarrow FeO/Ca_2Fe_2O_5 \rightarrow Fe$ $Ca_2Fe_2O_5$ provides better surface structure	(G. Liu et al., 2018)
$Ca_2Fe_2O_5$ SM: wet impregnation Calcination: 950 °C, 5 h	CLG temp: 800 - 900°C Fuel: char coal Reactor: fluidized bed		Gasification efficiency (%): 85 Gasification rate: 1.5 g/min/gcat	hampers hydrogen production in the iron-steam process enhances the rate of hydrogen production due to its active sites.	(Wang et al., 2019)

$CaFe_2O_4$ SM: direct decomposition Calcination: 500 °C, 6 h, 1000 °C, 6 h	CLG temp: 700 - 900°C Fuel: coal		OC LF LN5F5 L3B7F	Accumulative mole of syngas (mol/kg) 34 35 37	Carbon conversion (%) 93 94 97	Calcium plays a dual role in regulating the transportation of oxygen ions within the solid material and influencing the rate of carbon oxidation in coal char.	(Miller & Siriwardane, 2018)
Ba Based Perovskites							
$BaCoO_3$ $BaFeO_3$ $Ba_{0.5}Sr_{0.5}Co_{0.8}Fe_{0.2}O_3$ (BSCF) SM: sol gel method Calcination: 400, 850 ^{0}C, 20 h Perovskite/coal mass ratio: 0 – 0.3	CLG temp: room – 850 °C Fuel: lignite Fixed bed	12 c	Q̄: BSCF > BC > BF Steam/hydrogen: 0.641			BSCF sample had the lowest proportion of CO_2 and the highest hydrogen production. Elemental compositions do not change during CLG and stable after 6 cycles. Optimum reaction temperature between 800 ^{0}C and 850 ^{0}C the carbon conversion rate of pyrolysis stage decreases with increasing S/H ratio.	(Ding et al., 2016)
$BaFe_2O_4$ SM: direct decomposition	CLG temp: 850 °C Fuel: coal char Reactor: fixed bed		Max CO yield at first stage: 1.51 % at 552 °C Max CO yield at second stage: 0.38% at 850 °C			$BaFe_2O_4 \rightarrow BaFe_4O_7 \rightarrow BaO + FeO + Fe$	(Sun, Xiao, et al., 2022)
La Based Perovskites							
$LaFeO_3$ (LF) $LaFe_{0.5}Ni_{0.5}O_3$ (LN5F5) $La_{0.3}Ba_{0.7}FeO_3$ (L3B7F) SM: modified citric acid–nitrate sol–gel method	CLG temp: 700–900 ◦C Fuel: microalgae Reactor: fixed bed		Syngas yield (mol/mol microalgae) LF: 0.56 LN5F5: 0.71 L3B7F: 0.64			Below 400 °C, nitrogen oxides can be stored on the perovskite surface in the form of nitrites and/or nitrates. NO can be selectively reduced by reducing components over perovskites over 700 °C	(Yan et al., 2023)
$LaFe_{0.5}Mn_{0.5}O_3$ $LaFe_{0.5}Co_{0.5}O_3$ $LaFe_{0.5}Ni_{0.5}O_3$ $LaFe_{0.5}Cu_{0.5}O_3$ SM: sol gel method calcined at 900 ℃ for 4 h	CLG temp: 250 – 600 Fuel: biomass Reactor: fixed bed		Highest H_2 yield for LaFeNi: 3.71 $mmol.g^{-1}$ Highest CO yield for LaFeCo: 1.98 $mmol.g^{-1}$			LaFeNi suitable for torrefied biomass CLG The sequence of oxygen releasing capacity: LaFeCu > LaFeCo > LaFeNi > LaFeMn > LaFe	(Shen et al., 2022)
$La_{1-x}Ba_xFeO_3$ (x = 0, 0.3, 0.5, 0.7, 0.9, 1.0) SM: sol gel method calcined at 750 ◦C for 6 h	CLG temp: 900 ◦C Fuel: microalgae Reactor: fixed bed	10 c	$La0.3Ba_{0.7}FeO_3$ (L3B7F) exhibits the best performance in CLCSG The maximum syngas yield of 1.00 m^3/kg-Algae, carbon conversion of 98.86% and gasification efficiency of 96.71%			Tetravalent iron (Fe^{4+}) and oxygen vacancies are created when divalent barium (Ba^{2+}) is substituted for trivalent lanthanum (La^{3+}) at the A-site of $LaFeO_3$, greatly enhancing the oxygen transport capability and catalytic activity of perovskite.	(Yan et al., 2021)
$La_{1-x}Ca_xFeO_3$ (x = 0–0.4) SM: sol gel method	CLG temp: 700 - 900 ◦C Fuel:		CO conversion (%) highest for x=0.4: 9.8			CO conversion is increased by increasing CO adsorption capacity	(Sun, Shen, et

calcined in air at 800 °C for 6 h W: 0.05 g	Reactor: fixed bed			CO conversion increases by Ca substitution	al., 2022)
$LaCr_{0.5}Fe_{0.5}O_3$ $LaCo_{0.5}Fe_{0.5}O_3$ $LaCu_{0.5}Fe_{0.5}O_3$ SM: sol gel method calcined at 850 °C for 5 h in air PS: < 200 μm	CLG temp: 800 °C Fuel: digestate Reactor: fixed bed	8 c	For $LaCu_{0.5}Fe_{0.5}O_3$: gas yield: 1.03 Nm^3/kg gasification efficiency: 72.69%	B site can be doped with metal to increase activity and facilitate the CLG reaction	(Z. Li et al., 2022)
$La_{1-x}Ca_xFeO_3$ SM: sol-gel Calcination: 750°C, 6h	CLG temp: 800 °C Fuel: biomass Reactor: fixed bed Steam/biomass ratio: 1:1		X(N_2 to NH_3): 62.2%	Excessive doping of calcium (x = 0.3) reduces ammonia production. $La_{0.8}Ca_{0.2}FeO_3$ possessed the highest conversion	(P. Wang et al., 2023)

SM: Synthesis method, η: Efficiency, SSM: Solid State Method, CP: co-precipitation method, HT: hydrothermal method, SG: sol-gel method, X: Conversion, PS: Particle Size

CHAPTER 3: METHODOLOGY

3.1 Materials

The study focused on catalytic pyrolysis and steam gasification experiments conducted with biomass - Miscanthus, supplied by the Idaho National Laboratory. The biomass samples (Fig 8.) were dried at a temperature of 105 °C for 12 h and subsequently underwent crushing and sieving, resulting in particle sizes ranging from 125 to 150 μm.

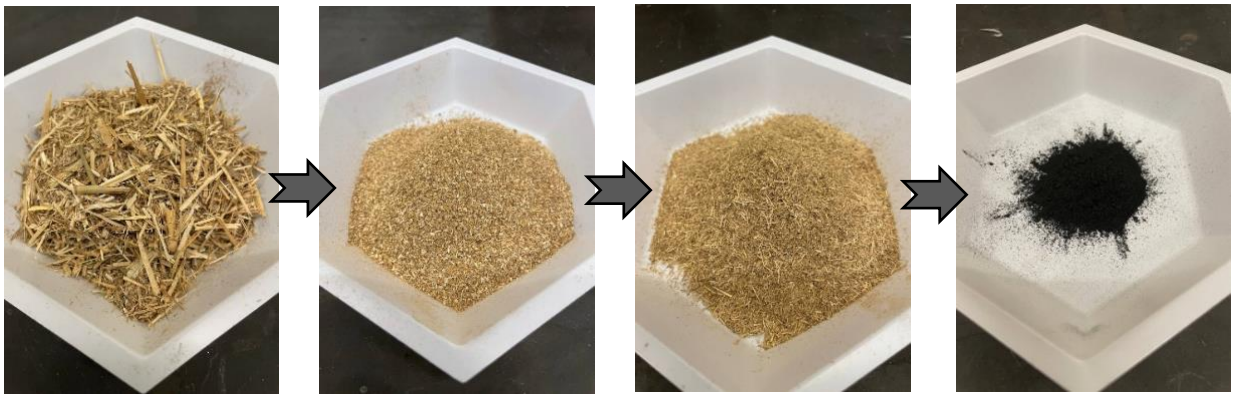

(a) (b) (c) (d)

Figure 8: a) Miscanthus biomass, b) dried and ground biomass, c) sieved biomass to the desired particle size, d) produced biochar (sieved for the second time to achieve the desired particle size)

The results of elemental analysis and ash composition of the biomass samples are presented in Table 4 and 5 respectively. The mass concentrations of C, H and O in miscanthus are 50.64%, 5.85%, and 43.06%, respectively. Thus, the H/C and O/C molar ratios of miscanthus are 1.376 and 0.621, respectively, suggesting that the molecular formula of miscanthus could be defined as $CH_{1.376}O_{0.621}$.

Table 4: Proximate and ultimate analysis of biomass (Miscanthus) composition.

Proximate analysis	**(% by weight)**
Fixed carbon	13.06
Volatile	85.53
Ash	1.40
Carbon	50.64
Hydrogen	5.85
Nitrogen	0.21
Oxygen	41.88
Sulfur	0.01

Table 5:Ash composition of biomass (Miscanthus) samples.

Compound	**Biomass ash (%)**
Al_2O_3	0.29
CaO	18.34
Fe_2O_3	1.20
K_2O	6.44
MgO	9.03
MnO	1.11
Na_2O	0.18
P_2O_5	3.58
SiO_2	52.31
TiO_2	0.02
SO_3	3.15

3.2 Preparation of Ca-Fe based oxygen carriers

Four different oxygen carriers $Ca_2Fe_2O_5$, $Ca_2Fe_{1.9}Cu_{0.1}O_5$, $Ca_2Fe_{1.9}Ni_{0.1}O_5$ and $Ca_2Fe_{1.9}Co_{0.1}O_5$ were prepared using the citric acid assisted sol-gel method (Fig 9.). In this process, calcium nitrate tetrahydrate ($Ca(NO_3)_2 \cdot 4H2O$), iron(III) nitrate nonahydrate ($Fe(NO_3)_3 \cdot 9H_2O$), and citric acid were mixed according to the desired molar ratios (Fe:Ca:citric acid = 1:1:6 for $Ca_2Fe_2O_5$ preparation). For the other modifications, $Cu(NO_3)_2.3H_2O$, $Ni(NO_3)_2.6H_2O$ and $Co(NO_3)_2 \cdot 6H_2O$ were added. The mixture was dissolved in deionized water and stirred constantly overnight at 80°C. The resulting solution was dried at 180°C for 12 hours and then calcined in air in a muffle furnace at 650°C for 4 hours (temperature ramp 5°C/min from room temperature to 650°C).

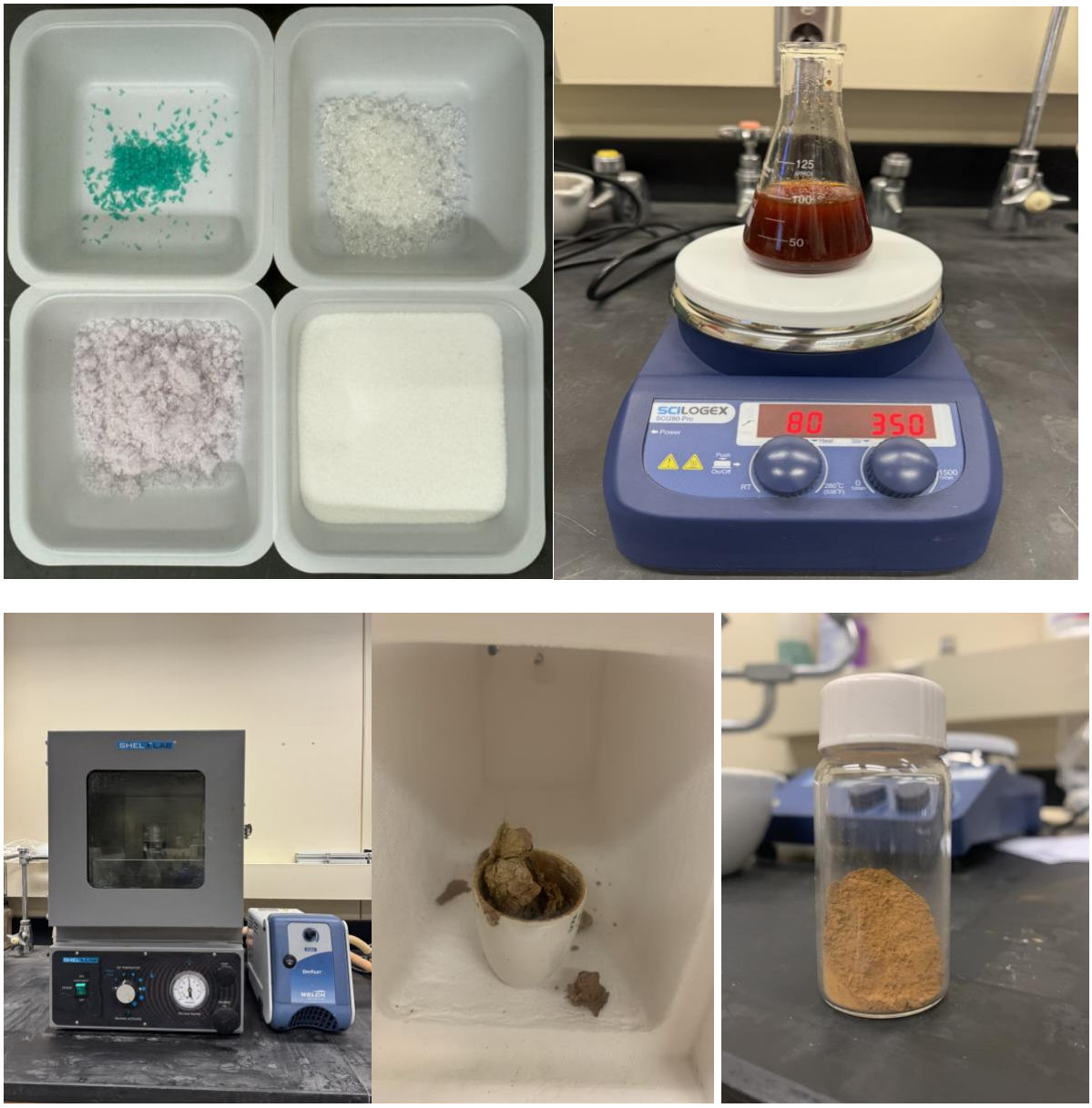

Figure 9: Synthesis of oxygen carrier via sol-gel process.

3.3 Characterization of carrier materials

The crystalline phases of OCs were determined by X-ray diffraction (XRD) which was conducted by Rigaku SmartLab X-ray Diffractometer using a Cu K α radiation (λ = 0.15046 nm), a target current of 40 mA, and a target voltage of 40 kV. The diffraction angle 2θ was scanned from 20 to 80 ° with a step of 0.0167 $°/s$. Transmission Electron Microscopy (TEM) was conducted using the JEOL 2010F Field Emission Transmission Electron Microscope to view ~3-5 clusters of each catalyst type. For morphological analysis, the scanning electron microscopy (SEM) and energy dispersive spectrometer (EDS) were conducted using the Thermo Quattro S field-emission environmental Scanning Electron Microscope.

3.4 Experimental set-up and procedure

The steam gasification tests on biomasses were conducted using a fixed bed reactor, with the experimental setup consisting primarily of an electrical furnace, a reactor, a steam generator, a temperature controller, flow meters, and gas collecting bags (as depicted in Fig 10. & 11.). The reactor was constructed from a quartz tube with dimensions of 0.750” in outer diameter, 0.500” in inner diameter and 40” in length.

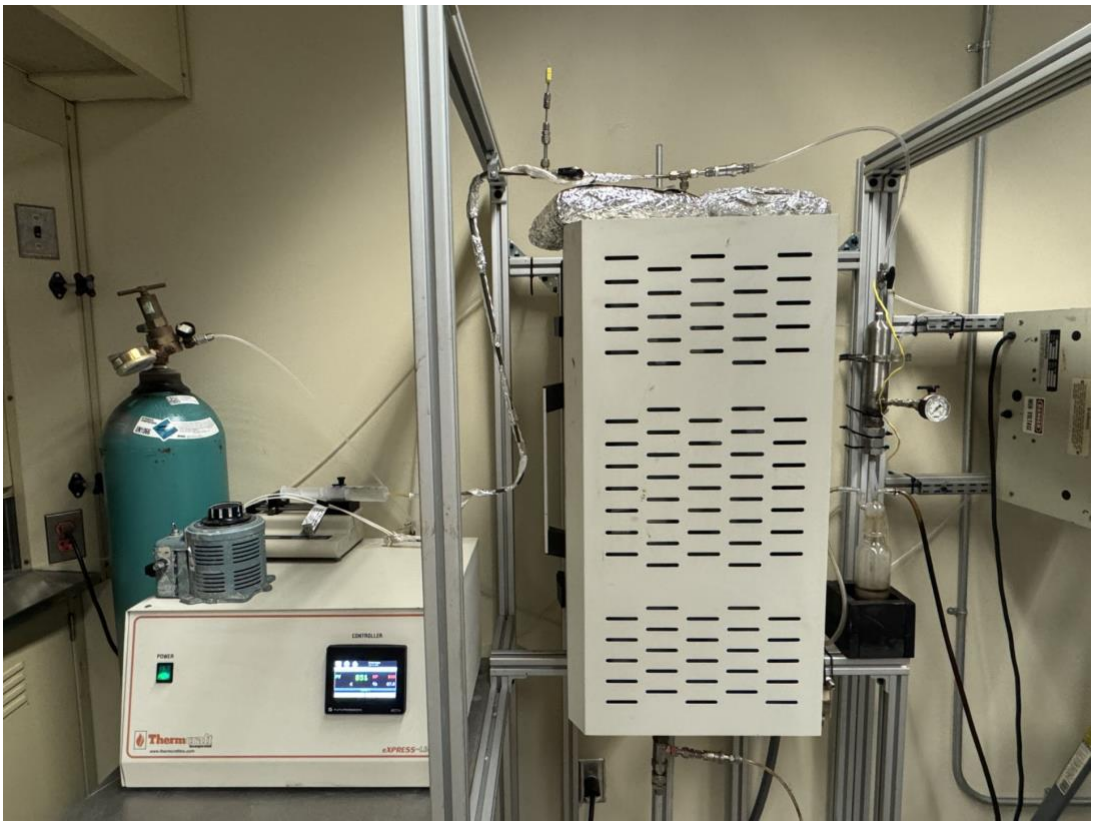

Figure 10: Experimental setup for investigating biomass conversion processes: pyrolysis and gasification.

In a typical experiment, a mixture of 4 g of biomass and 0.4 g of catalyst was prepared by constant stirring and grinding for at least 5 min. Subsequently, the mixture was loaded into the constant temperature zone of the quartz tube reactor. Prior to heating the furnace to the desired temperature (650 °C, 750 °C or 850 °C) at a heating rate of 20 °C/min and an N_2 flow rate of 50 mL/min, the system was purged with N_2. Once the specified temperature was reached, water was injected at the desired flow rate of 0.10 mL/min using a syringe pump, initiating the gasification stage. The produced gas underwent cleaning and drying before being sampled with gas bags every 10 min. The concentrations of H_2, CH_4, CO, and CO_2 in each sample bag were determined using a Shimadzu 2014 GC.

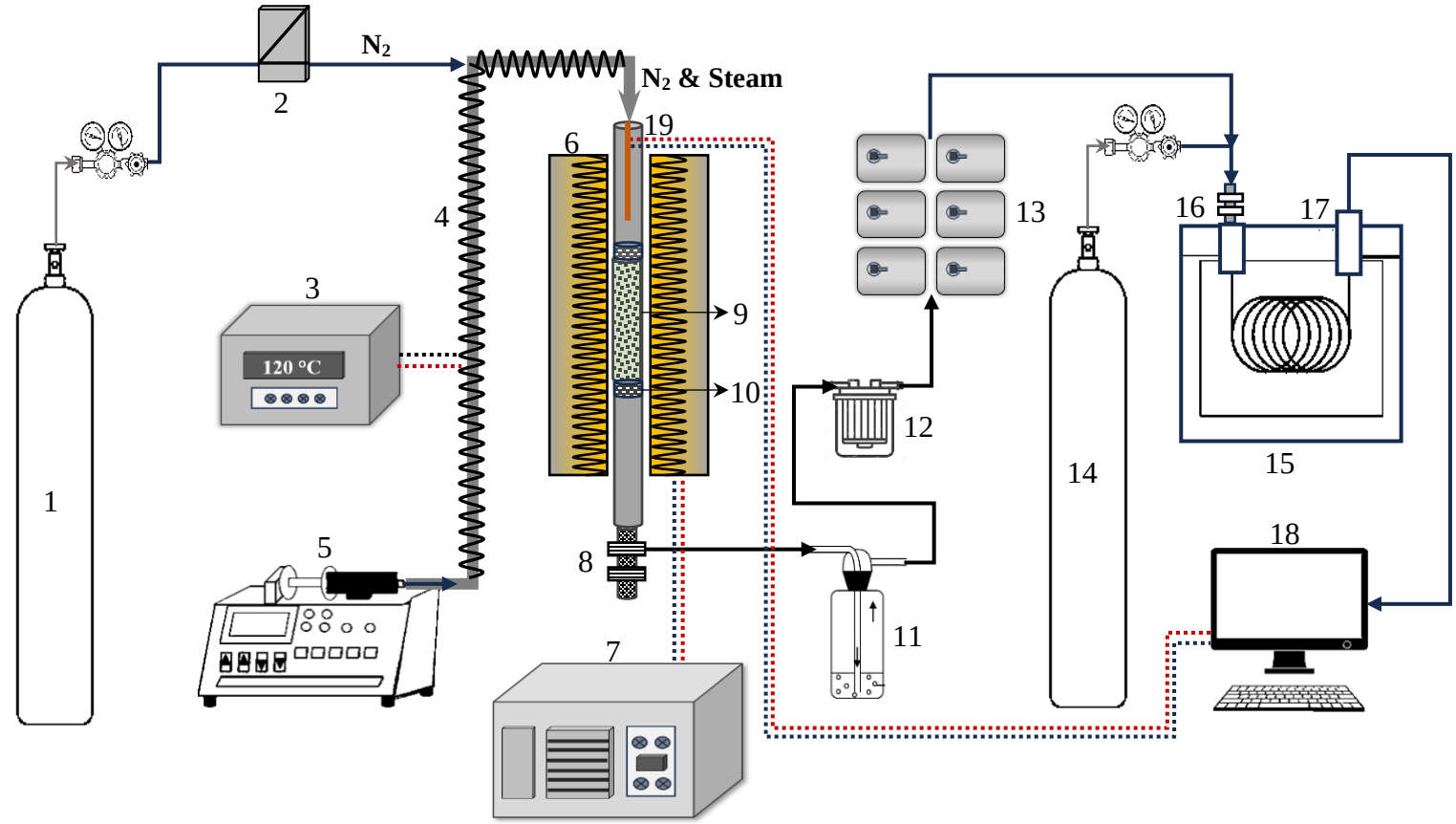

Figure 11: Schematic diagram of fixed bed catalytic biomass refinery system. (1) N_2 cylinder; (3) heating tape temperature controller; (4) Heating tape; (5) HPLC syringe pump 0.1 – 10 ml/min; (6) fixed bed furnace and quartz tubular reactor; (7) temperature controller of furnace; (8) bio-oil collector; (9) biomass sample; (10) sample stopper; (11) gas wash bottle; (12) membrane filter; (13) gas bags; (14) Argon cylinder; (15) Gas chromatograph, Shimadzu; (16)

As seen in Fig 12., gas samples were collected using 1 L Tedlar® bags connected to the outlet of the gas wash unit, where the gas was passed through a cleaning process. The flow rate of the gas exiting the gas wash unit was measured using a soap film flowmeter.

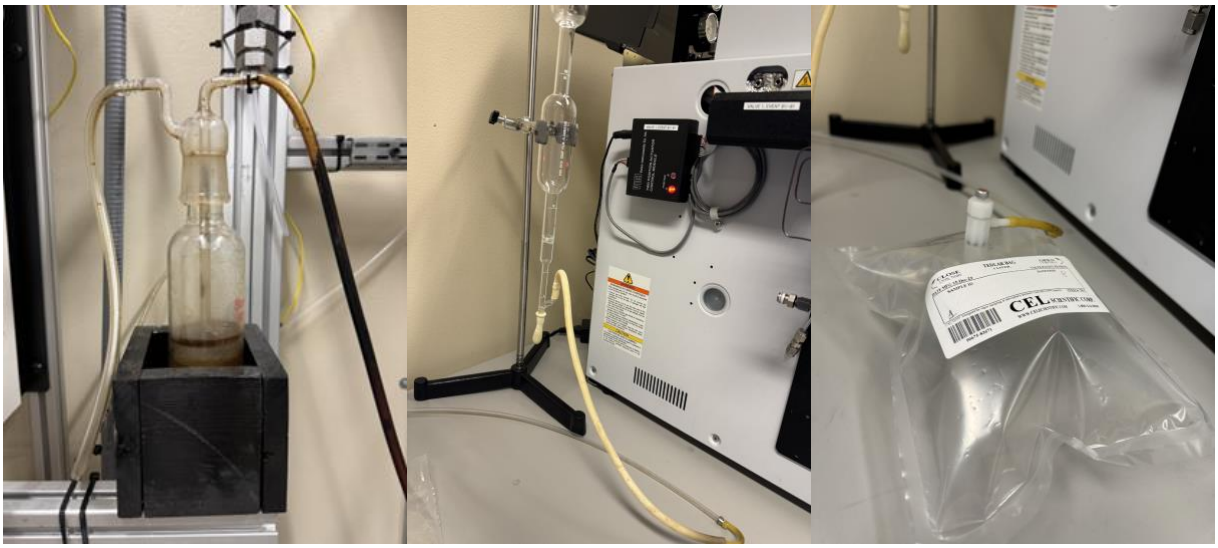

Figure 12: Schematic of the gas sampling setup.

A Shimadzu GC-2014 equipped with a ShinCarbon column (2.0 m length, 0.53 mm ID, 212 µm film thickness) was employed for the analysis of the collected gas samples. Argon served as the carrier gas. Five calibration standards were prepared with varying concentrations of target gas components as shown in Table 6.

Table 6. Calibration Standard Compositions

Std	CO_2 (mol %)	CO (mol %)	H_2 (mol %)	CH_4 (mol %)	O_2 (mol %)	N_2 (mol %)
1	1 %	1 %	1%	1%	1%	95 %
2	15 %	7 %		4.5 %	4 %	-
3	-	-	99.99 %	-	-	-
4	-	-	-	99.99 %	-	-
5	99.8 %	-	-	-	-	-

The GC was operated under the following conditions:

- Column temperature: 40 °C (isothermal)
- Equilibration time: 0.2 min
- Injector temperature: 250 °C
- Injection mode: Split
- Sampling time: 1 min
- Pressure: 278.5 kPa
- Total flow: 10.5 mL/min
- Linear velocity: 187.9 cm/s
- Purge flow: 3.0 mL/min
- Split ratio: 2

The detector (DTCD) was operated at a temperature of 100 °C with a filament current of 70 mA. Byproducts, including biochar and bio-oil (Fig 13.), were collected in vials. These materials can be utilized for further applications.



Figure 13: Bio-oil (left) and biochar (right) collected during the biomass conversion process.

3.5 Data Analysis

The volume of syngas components (H_2, CH_4, CO, CO_2) were calculated as follows:

$$V_{H_2} = C_{H_2}V \quad \text{(Equation 4)}$$

$$V_{CO} = C_{CO}V \quad \text{(Equation 5)}$$

$$V_{CH_4} = C_{CH_4}V \quad \text{(Equation 6)}$$

$$V_{CO_2} = C_{CO_2}V \quad \text{(Equation 7)}$$

where $C_{H_2}, C_{CH_4}, C_{CO}, C_{CO_2}$ represent the syngas concentrations of H_2, CH_4, CO, and CO_2, respectively, and V represents the volume of gas collected in sampling bag every 10 minutes. The total gas yields for one gas bag are calculated as:

$$Y_i = \frac{C_i V}{m} \quad \text{(Equation 8)}$$

where C_i was the actual concentration of gas component i, measured by the GC; V (L) was the volume of gas collected in sampling bag every 10 minutes and m (g) was the mass of Miscanthus.

The cumulative H_2 yield is the sum of H_2 obtained with every 10 min:

$$Y_{H_2} = \sum_1^n Y_{H_2} \quad \text{(n=1,2,3,4,5,6,7,8,9)} \quad \text{(Equation 9)}$$

The syngas concentration (C_{syngas}) and CO selectivity (S_{CO}) are defined as:

$$C_{syngas} = \frac{Y_{CO}+Y_{H_2}}{\sum Y_i} \quad \text{(Equation 10)}$$

$$S_{CO} = \frac{Y_{CO}}{Y_{CO}+Y_{CO_2}} \quad \text{(Equation 11)}$$

CHAPTER 4: RESULTS AND DISCUSSIONS

4.1 Physical properties

Fig 14. shows SEM images revealing the surface morphology of the synthesized OCs, along with corresponding EDS mapping. As can be seen, $Ca_2Fe_2O_5$ performed as a flake structure with large

amount of pores. When doped with Co, its structure did not have significant variations. The EDS mapping confirms the presence of Ca, Fe, Co, Cu and Ni in respective catalysts. The results of EDS mapping are summarized in Table 7. It also revealed that all elements were uniformly distributed within all synthesized OCs, indicating the uniform impact of OC.

Table 7: Extracted spectrum weight % for each element by SEM.

	Weight %			
Element	**$Ca_2Fe_2O_5$**	**$Ca_2Fe_{1.9}Cu_{0.1}O_5$**	**$Ca_2Fe_{1.9}Co_{0.1}O_5$**	**$Ca_2Fe_{1.9}Ni_{0.1}O_5$**
O	40.209	35.58	29.745	32.037
Ca	19.703	23.349	21.343	12.992
Fe	29.089	26.633	35.057	37.068
Cu	-	3.805	-	-
Co	-	-	2.944	-
Ni	-	-	-	6.055

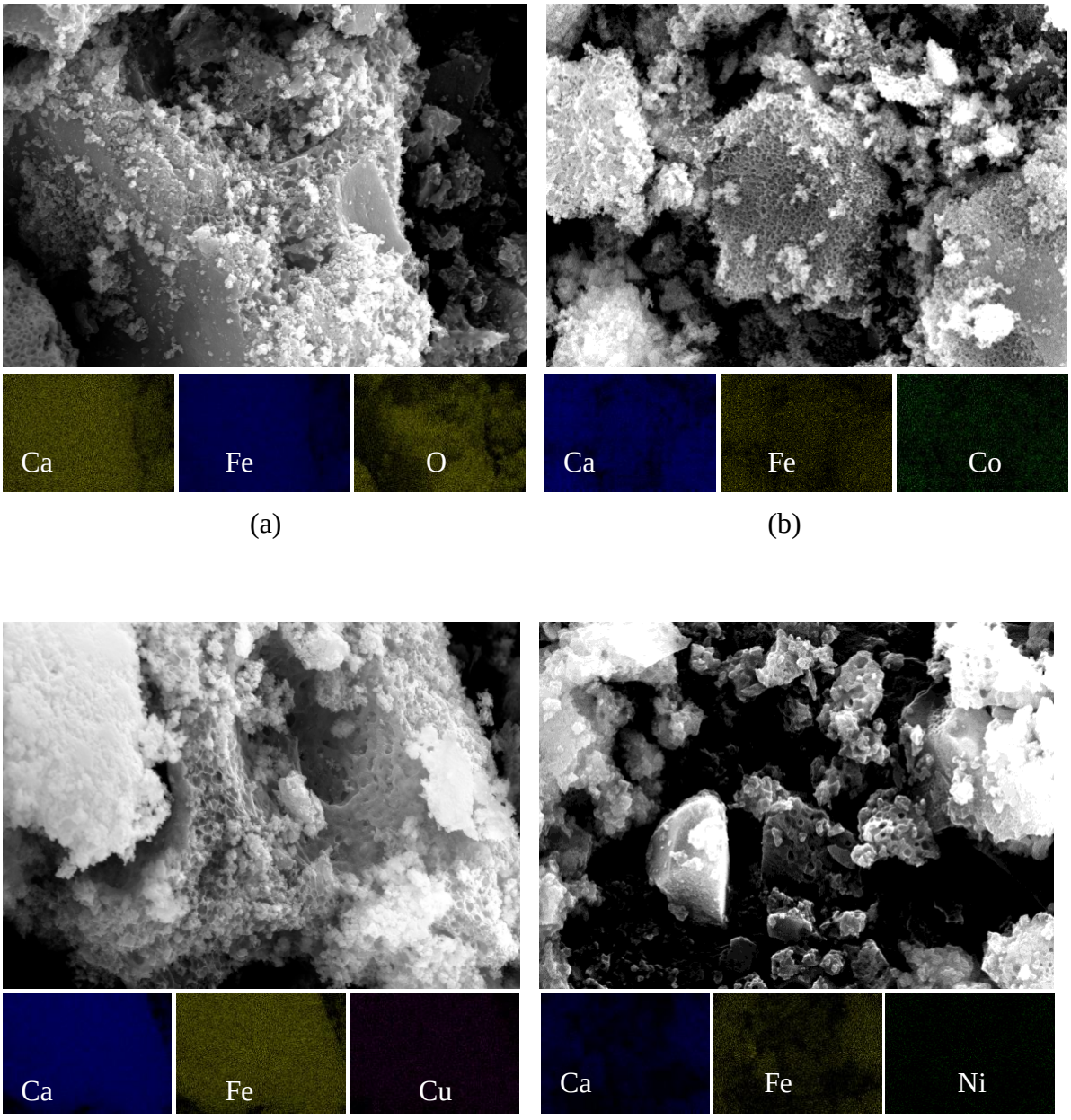

Figure 14: SEM-EDS images of a) $Ca_2Fe_2O_5$, b) $Ca_2Fe_{1.9}Co_{0.1}O_5$, c) $Ca_2Fe_{1.9}Cu_{0.1}O_5$, d) $Ca_2Fe_{1.9}Ni_{0.1}O_5$.

TEM micrographs (Fig 15.) were obtained using lacey carbon grids (Ted Pella) for all samples except those containing Cu. For Cu-containing variants, lacey carbon nickel grids were employed. Grid preparation involved dry shaking the grids within the sample vial, ensuring adherence of the smallest nanoparticles to the grid mesh. Notably, the $Ca_2Fe_2O_5$ morphology remained consistent across all samples, while variations in secondary signals detected by EDS were observed between different samples. All samples exhibited uniform elemental distribution, regions with elevated Fe content also displayed a corresponding increase in O content, as revealed by EDS mapping.

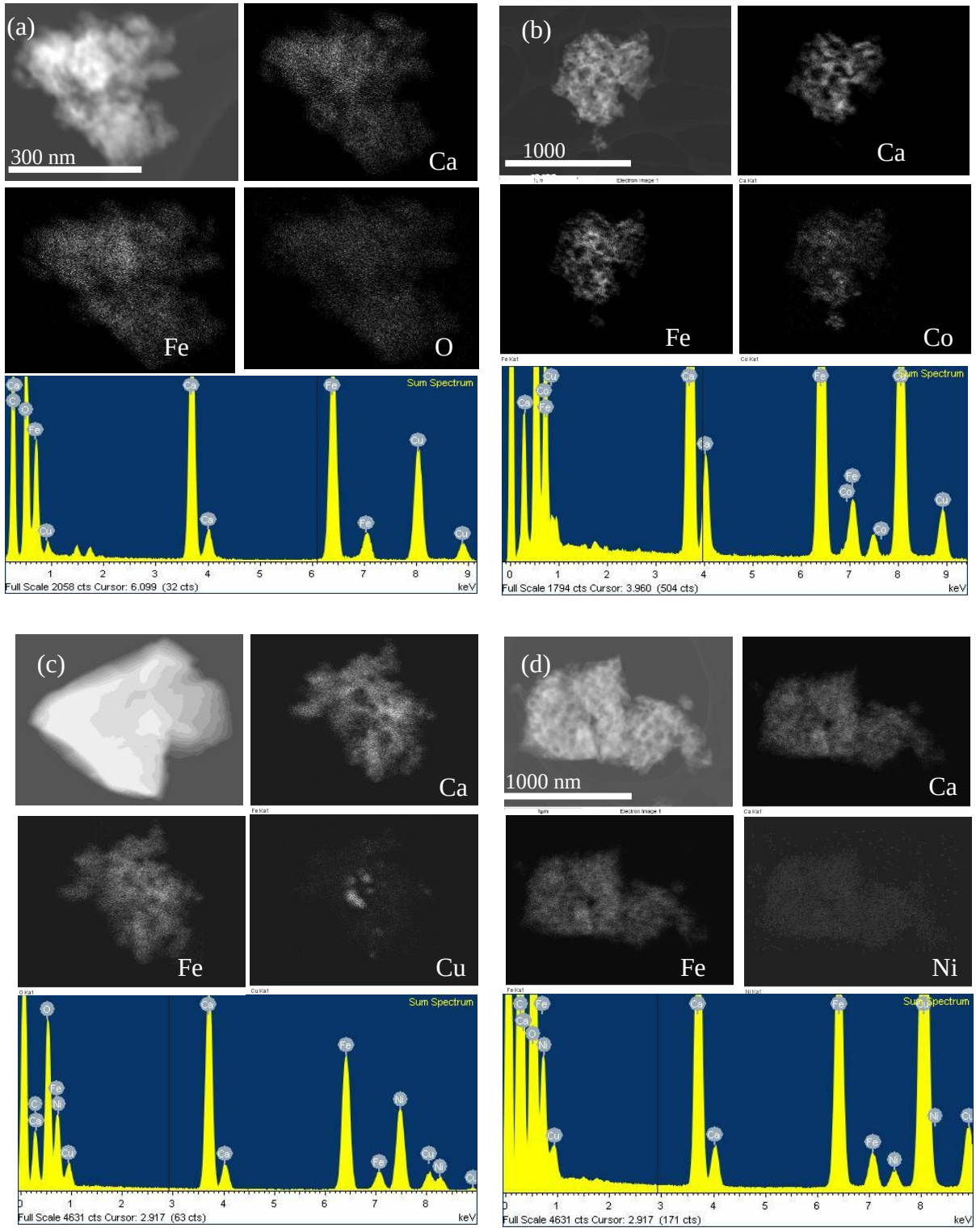

Figure 15: TEM-EDS images of fresh a) $Ca_2Fe_2O_5$, b) $Ca_2Fe_{1.9}Co_{0.1}O_5$, c) $Ca_2Fe_{1.9}Cu_{0.1}O_5$, d) $Ca_2Fe_{1.9}Ni_{0.1}O_5$.

As shown in Fig 16., XRD was carried out to detect the phase structures of OC. The crystallite size was calculated using the Scherrer equation by fitting a Gaussian function to the four most intense characteristic peak to obtain the peak width at half maximum. The observed diffraction peaks of $Ca_2Fe_2O_5$ were perfectly indexed with JCPDS Card no 71–2264. The results also revealed that all oxygen carriers exhibited a brownmillerite-type crystalline structure. Doping with Co, Ni, or Cu did not alter the overall crystal structure, but some variations in the diffraction patterns were observed. Notably, Cu doping resulted in a shift of most diffraction peaks to higher angles. This suggests that Cu doping may decrease the grain size within the brownmillerite structure, leading to an increase in crystal plane d-spacings.

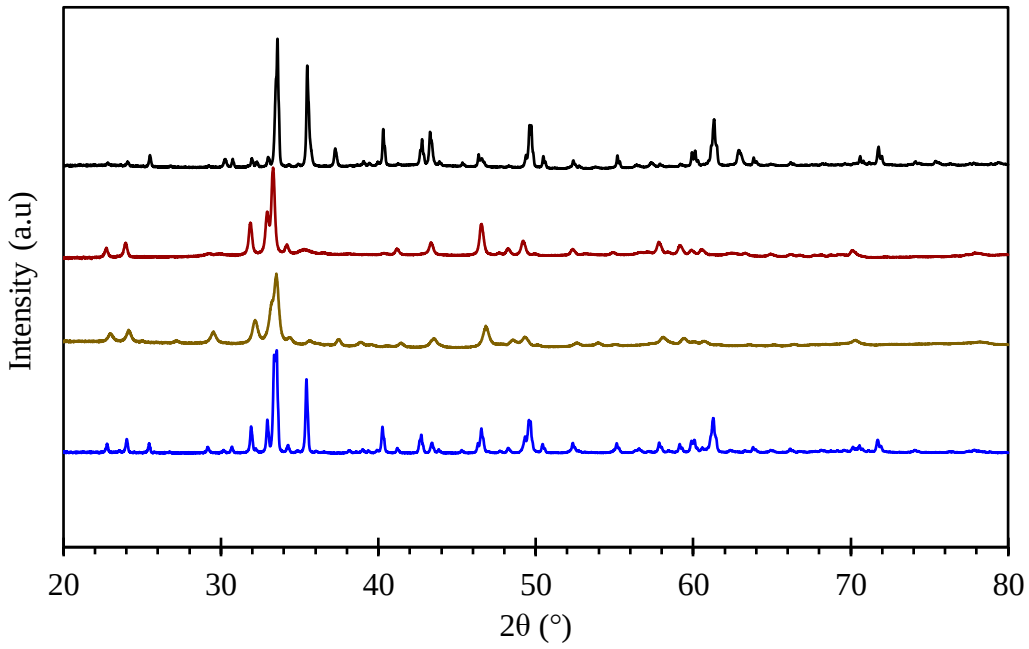

Figure 16: XRD images of fresh a) $Ca_2Fe_2O_5$, b) $Ca_2Fe_{1.9}Co_{0.1}O_5$, c) $Ca_2Fe_{1.9}Cu_{0.1}O_5$, d) $Ca_2Fe_{1.9}Ni_{0.1}O_5$.

Figure 17 presents the FTIR spectra of the $Ca_2Fe_2O_5$ catalysts with Cu, Co, and Ni dopants. All samples exhibit characteristic peaks at 594 cm^{-1} and 710 cm^{-1}, corresponding to Fe-O and Fe-Ca stretching vibrations, respectively (Vadivel et al., 2016). The addition of dopants leads to a slight decrease in the intensity of the Fe-Ca peak, suggesting a potential interaction between the dopant and calcium cations. The strongest absorption band observed at 3470 cm^{-1} can be attributed to O-H groups in aromatic and aliphatic structures (Choi et al., 2020). This suggests the presence of surface hydroxyls likely formed during the breaking of hydrogen bonds, potentially releasing water or alcohols during the synthesis process. Additionally, a peak at 1450 cm^{-1} indicates the presence of C-O stretching vibrations (Berestova et al., 2020), while the peak at 1640 cm^{-1} is associated with amide I bonds (Tenri Ola et al., 2022).

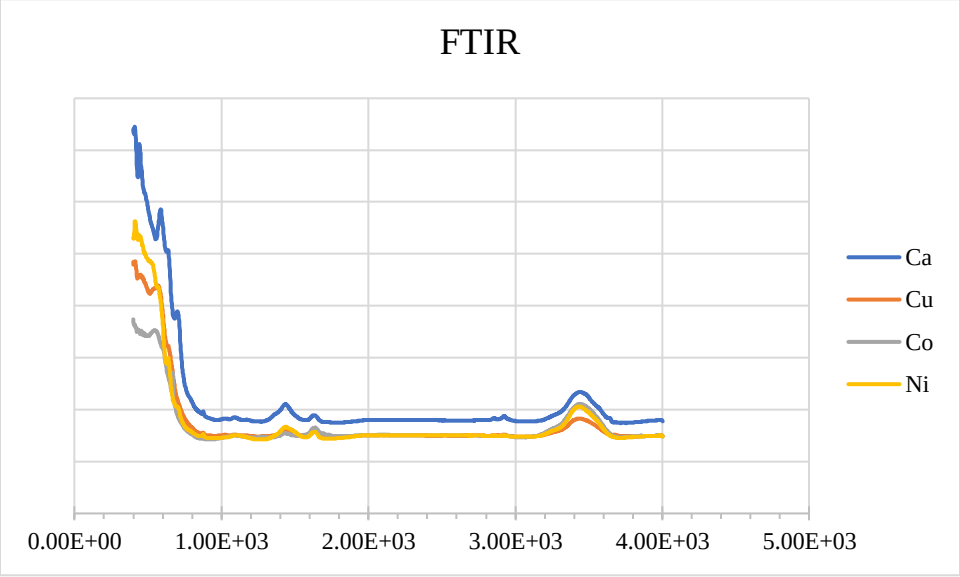

Figure 17: FTIR spectra of oxygen carriers

4.2 CLG without steam

The reactivity of different OCs in BCLG was tested in a fixed bed reactor. Biomass first undergoes initial decomposition into gaseous products, tars, and char. The OC then participates in a redox reaction with these pyrolysis products. This redox interaction, involving both the oxidation of char and reforming of tars, significantly enhances the production of syngas. However, excessively high oxidation activity by the OC can be detrimental to syngas yield. This is because it can promote the conversion of valuable syngas components (CO and H_2) into less desirable products like CO_2 and H_2O.

Figure 18 reveals the contrasting effects of pyrolysis on biomass alone compared to when four different OCs are introduced. The presence of the OC demonstrates a two-fold impact. Firstly, it acts as a cracking catalyst, significantly boosting the overall yield of gaseous products from the biomass. Secondly, the OC exhibits selective oxidation behavior. While the addition of the catalyst doesn't substantially alter the production of hydrogen (H_2), it does lead to a noticeable increase in CO selectivity, shifting from 41.5% without the catalyst to 53.3% with $Ca_2Fe_2O_5$. This observed CO appears to originate from the partial oxidation of carbon species on the OC surface, rather than direct decomposition by oxygen or complete oxidation for heat generation. Consequently, the partial oxidation activity of $Ca_2Fe_2O_5$ in this study results in the highest CO content observed in the gas products from the biomass-OC mixture. Interestingly, the addition of $Ca_2Fe_2O_5$ significantly enhances H_2 yield, with a notable increase from 5.71 mol/kg biomass (raw pyrolysis) to 9.406 mol/kg biomass with catalyst. However, doping the OC with small quantities (0.1 mol/kg) of Cu, Co, or Ni did not necessarily improve the purity of the H_2 produced. Copper's low melting point (1085 °C) can lead to agglomeration in Cu-doped oxygen carriers (OCs). This phenomenon might contribute to the observed lower H_2 production compared to other dopants. Operating the fuel reactor at temperatures below 800 °C is recommended to mitigate this potential issue.

The reaction temperature plays a critical role in governing the efficiency of catalytic biomass pyrolysis, as corroborated by numerous studies (Hu & Gholizadeh, 2019). This is further supported by the data presented in Figure 19 that depicts the trend of total gas yield with increasing temperature during biomass pyrolysis with and without the OC. The results show a gradual increase in total gas production at 750 °C compared to 650 °C, followed by a slight decrease at 850 °C. This non-monotonic behavior can be attributed to the interplay of several competing reactions involving the OC, syngas, biochar, and tar. While literature confirms that syngas production generally increases with temperature during biomass pyrolysis [49], high temperature can also enhance the OC's reactivity towards syngas [39]. The observed decrease at 850 °C suggests that these competing reactions become significant. The OC may be consuming a portion of the syngas at this temperature. At higher temperatures, the OC's reactivity might be compromised due to sintering at excessively high temperatures [50]. Consequently, the dominant reaction becomes biomass pyrolysis for syngas production, leading to an overall increase in total gas yield.

Figure 20 illustrates the average composition of syngas across experiments with increasing temperature. The CO concentration remains relatively while the H_2 fraction exhibits a gradual increase with temperature. This can be attributed to the CO_2 reforming reaction with CH_4 and the Boudouard reaction, both of which are known to be favored by higher temperatures [51]. This explains the observed decrease in CO_2 and CH_4 fractions. Additionally, higher temperatures promote tar cracking, further contributing to the rise in H_2 content.

Pyrolysis of miscanthus proceeds in the ways of:

Biomass pyrolysis: $CH_{1.376}O_{0.621} \rightarrow (H_2 + CO + CO_2 + CH_4 + C_2 + \ldots) + Tar + Char$ (R1)

Tar cracking: $C_n H_m \rightarrow (m/2) H_2 + C_n$ (R2)

$Ca_2Fe_2O_5$ reduction with CO: $Ca_2Fe_2O_5 + 3CO \rightarrow 2CaO + 2Fe + 3CO_2$ (R3)

$Ca_2Fe_2O_5$ reduction with H_2: $Ca_2Fe_2O_5 + 3H_2 \rightarrow 2CaO + 2Fe + 3H_2O$ (R4)

$Ca_2Fe_2O_5$ reduction with CH_4: $4Ca_2Fe_2O_5 + 3CH_4 \rightarrow 8CaO + 8Fe + 3CO_2 + 6\ H_2O$ (R5)

Tar conversion with CO_2: $C_n H_m(tar) + nCO_2 \rightarrow nCO + m/2H_2$ (R6)

Tar conversion with H_2O: $C_n H_m(tar) + nH_2O \rightarrow nCO + (m/2 + n)H_2$ (R7)

The introduction of a $Ca_2Fe_2O_5$ introduces complexity to the biomass pyrolysis process compared to uncatalyzed reactions. This complexity arises from the interaction between the catalyst and the syngas produced during pyrolysis. The catalyst undergoes reduction by syngas, generating H_2O and CO_2 according to reactions (R3-R5). These reduction products can further promote the decomposition of tar, a complex mixture of heavier hydrocarbon molecules, into smaller molecules during pyrolysis. This enhances the yield of valuable products like syngas. While the catalyst consumes a portion of the reducing gases (H_2 and CO) that contribute to syngas production, the generated CO_2 and H_2O promote tar cracking, potentially leading to a higher overall syngas yield. This suggests a net benefit despite the initial consumption of reducing gases. The reducing atmosphere created by syngas during pyrolysis partially reduces the Fe in $Ca_2Fe_2O_5$ to FeO, with the concurrent formation of CaO, which offers an additional advantage. CaO itself acts as a catalyst, further enhancing tar cracking and promoting better overall biomass conversion during pyrolysis.

Figure 20 reveals that the majority of H_2 release occurs within the first 20-40 minutes of the experiment. This observation suggests that investigating the influence of water injection rate prior

to reaching the set reaction temperature might be beneficial. Consequently, in this study, the syringe pump for water injection was activated as soon as the furnace temperature reached 100 °C.

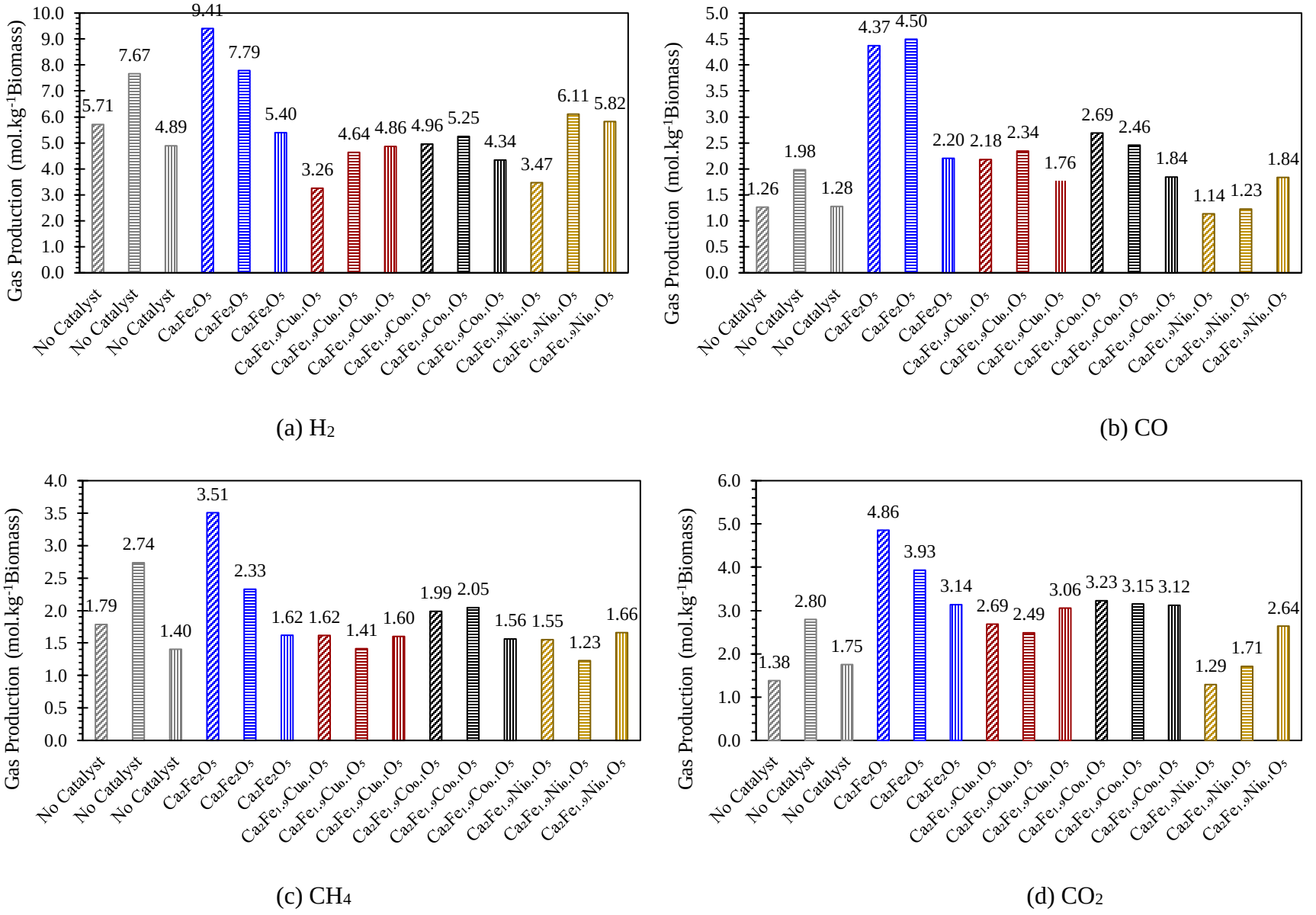

Figure 18: Effect of doping $Ca_2Fe_2O_5$ with Cu, Co and Ni on gas composition and production during pyrolysis.

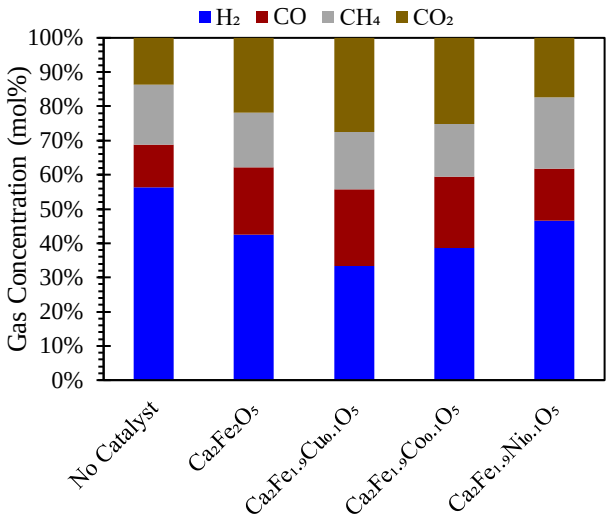
H₂
CO
CH₄
CO₂
Gas Concentration (mol%)
100%
90%
80%
70%
60%
50%
40%
30%
20%
10%
0%
No Catalyst
Ca2Fe2O5
Ca2Fe1.9Cu0.1O5
Ca2Fe1.9Co0.1O5
Ca2Fe1.9Ni0.1O5

(a) 650 °C

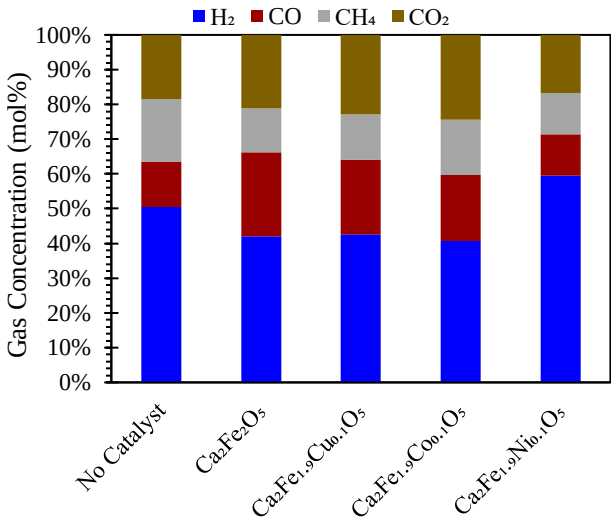
H₂
CO
CH₄
CO₂
Gas Concentration (mol%)
100%
90%
80%
70%
60%
50%
40%
30%
20%
10%
0%
No Catalyst
Ca2Fe2O5
Ca2Fe1.9Cu0.1O5
Ca2Fe1.9Co0.1O5
Ca2Fe1.9Ni0.1O5

(a) 750 °C

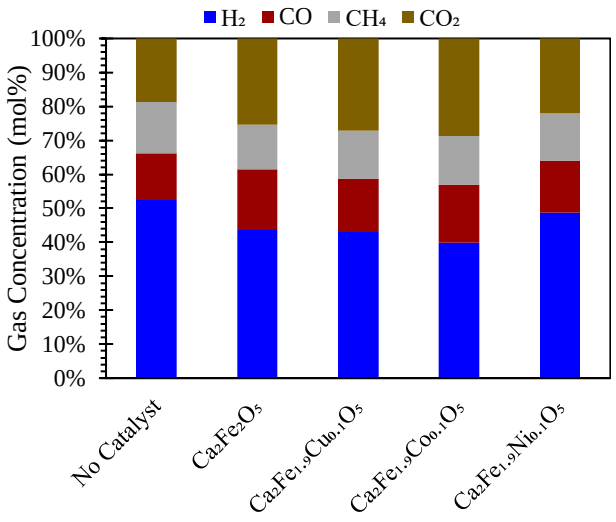

(a) 850 °C

Figure 19: Gas composition and total gas production during pyrolysis stage at different temperatures.

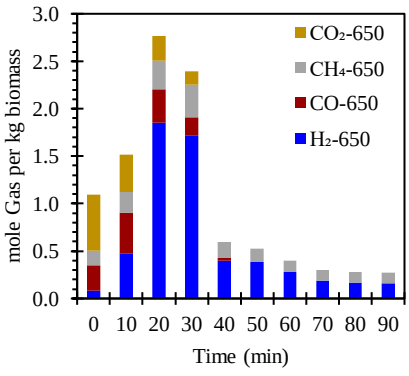

(a) No Catalyst, 650 °C

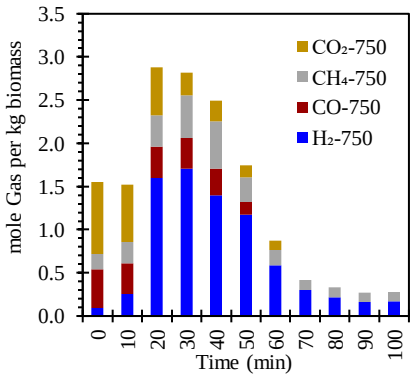

(a) No Catalyst, 750 °C

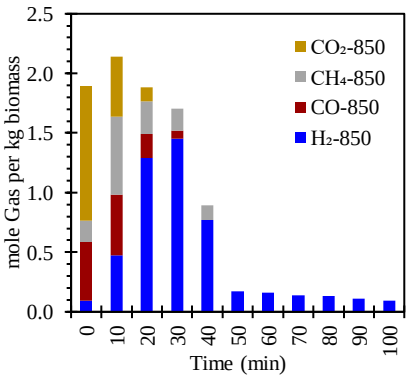

(a) No Catalyst, 850 °C

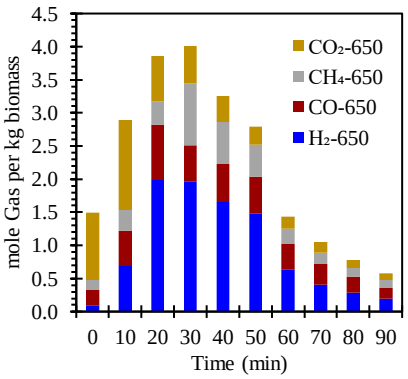

(b) $Ca_2Fe_2O_5$, 650 °C

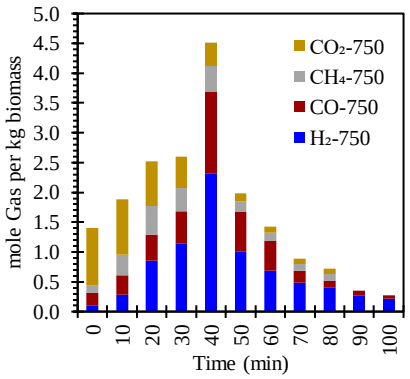

(b) $Ca_2Fe_2O_5$, 750 °C

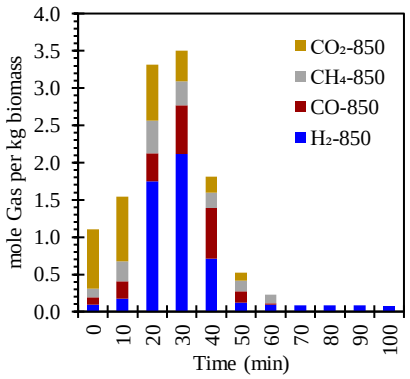

(b) $Ca_2Fe_2O_5$, 850 °C

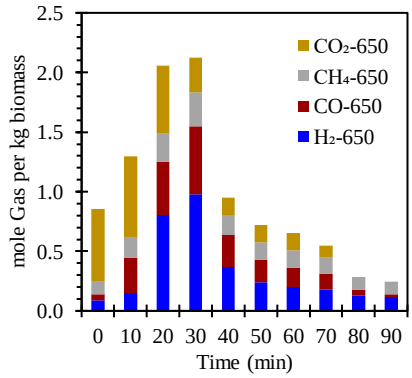

(c) $Ca_2Fe_{1.9}Cu_{0.1}O_5$, 650 °C

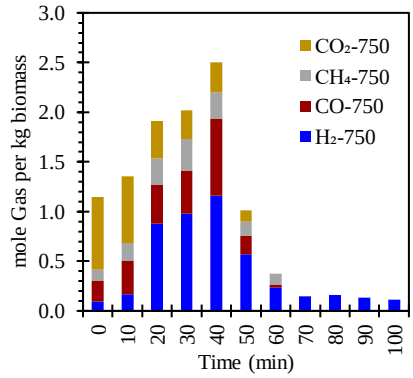

(c) $Ca_2Fe_{1.9}Cu_{0.1}O_5$, 750 °C

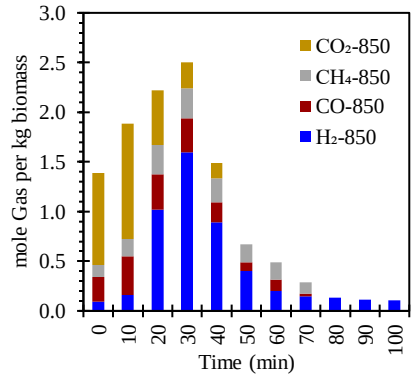

(c) $Ca_2Fe_{1.9}Cu_{0.1}O_5$, 850 °C

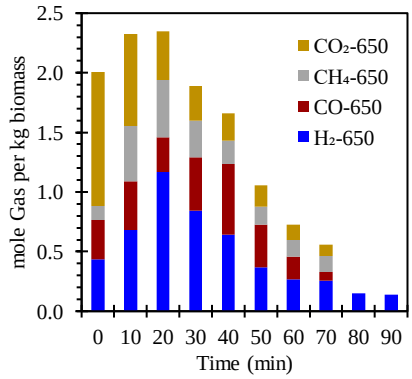

(d) $Ca_2Fe_{1.9}Co_{0.1}O_5$, 650 °C

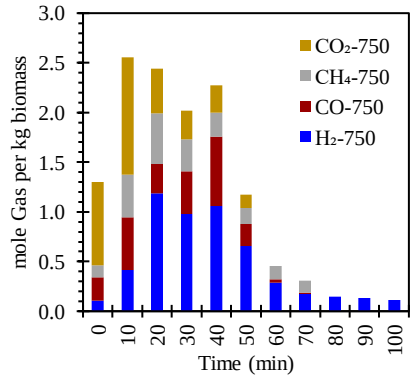

(d) $Ca_2Fe_{1.9}Co_{0.1}O_5$, 750 °C

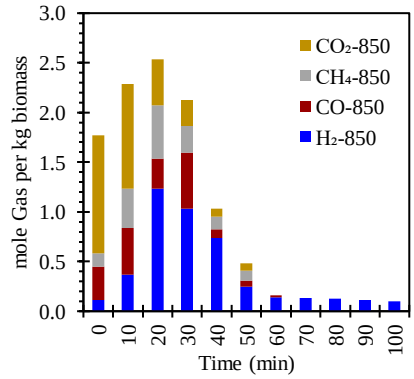

(d) $Ca_2Fe_{1.9}Co_{0.1}O_5$, 850 °C

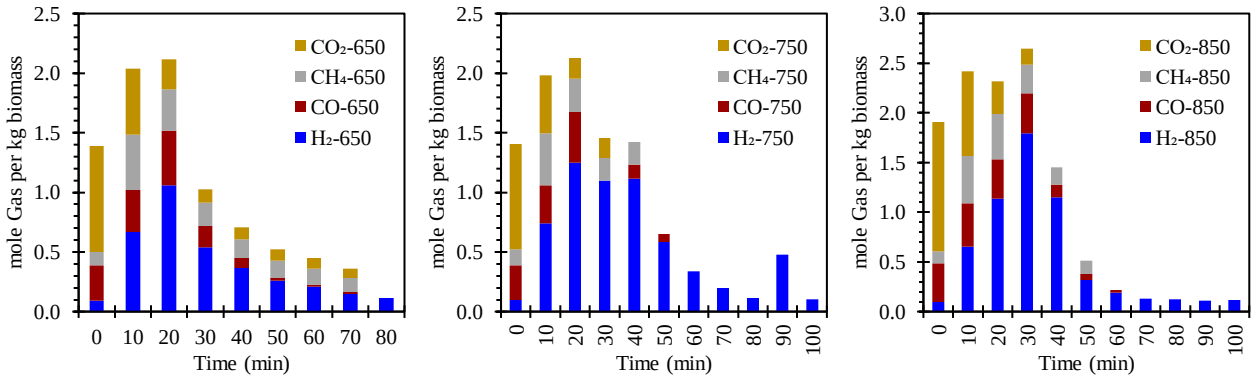

(e) $Ca_2Fe_{1.9}Ni_{0.1}O_5$, 650 °C (e) $Ca_2Fe_{1.9}Ni_{0.1}O_5$, 750 °C (e) $Ca_2Fe_{1.9}Ni_{0.1}O_5$, 850 °C

Figure 20: Syngas concentration and yields from miscanthus pyrolysis using pure biomass, $Ca_2Fe_2O_5$, $Ca_2Fe_{1.9}Cu_{0.1}O_5$, $Ca_2Fe_{1.9}Co_{0.1}O_5$, and $Ca_2Fe_{1.9}Ni_{0.1}O_5$.

4.3 CLG with steam

Steam is a well-established gasifying agent for the production of hydrogen-rich syngas. Studies have demonstrated an initial increase in H_2 yield with increasing steam concentration during biomass pyrolysis. To investigate this effect, steam was injected into the system at three flow rates: 0.05 mL/min, 0.1 mL/min, and 0.2 mL/min (Figure 21). As expected, H_2 production initially increased with increasing steam flow. However, observations indicated that a significant portion of the injected steam remained unreacted, leading to bio-oil dilution and potential inefficiency.

Furthermore, the relationship between steam and H_2 production becomes more intricate when oxygenated catalysts are present. Two key factors contribute to this complexity. Firstly, higher initial temperatures promote biochar conversion, reducing the amount of biochar available for steam gasification and ultimately decreasing H_2 yield. Secondly, excessive steam can impede H_2 production by blocking active sites on the OCs, hindering their catalytic activity.

Therefore, to optimize H_2 production while minimizing unreacted steam, a steam flow rate of 0.1 mL/min was chosen for all subsequent gasification tests within this study.

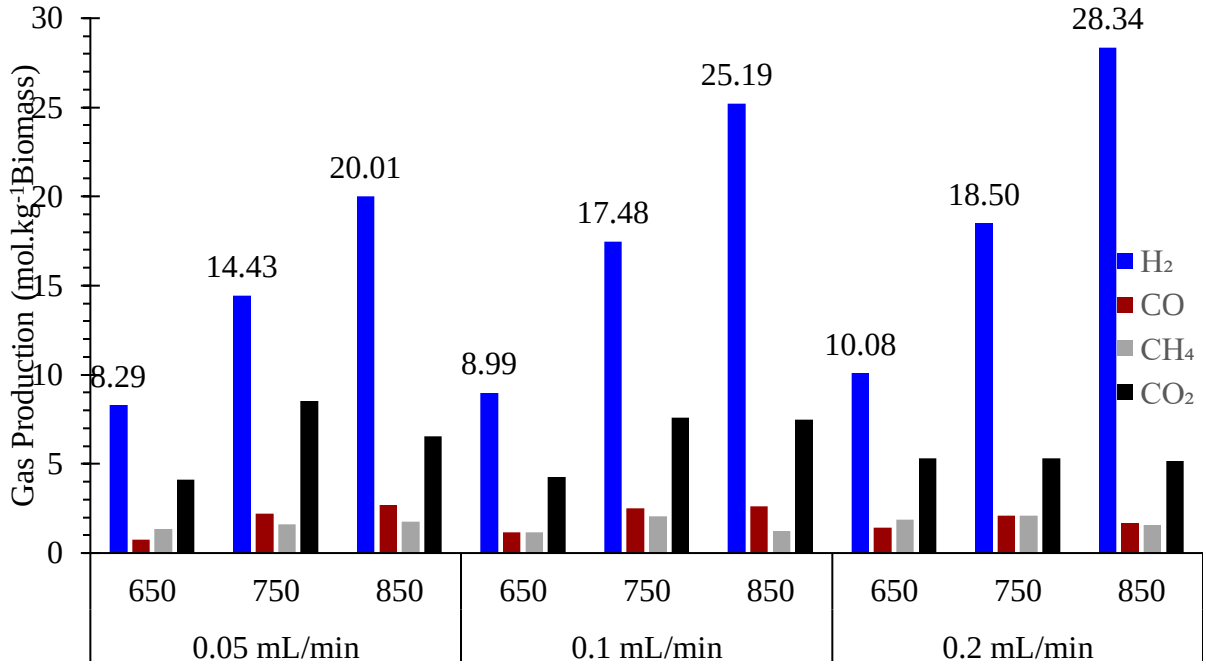

Figure 21: H_2 Production During Gasification Trials at Different Temperatures and Water Injection Rates

Steam plays a critical role in shaping the product gas distribution during biomass gasification, as evident in Figure 21. Its introduction significantly increases H_2 and CO_2 yields, while decreasing CO and CH_4 production. This effect arises from two main steam-driven reactions: the water gas shift (WGS) reaction ($CO + H_2O \rightarrow CO_2 + H_2$), which consumes CO and promotes H_2 and CO_2 formation, and the iron-steam reaction with reduced iron in the catalyst, further enhancing H_2 production. The second stage of gasification with steam encompasses a complex interplay between various gas species, vapor, biochar, and the reduced catalyst. The main reactions were shown as follows:

Steam oxidation of Fe^0: $2Fe + 2CaO + 3H_2O \rightarrow Ca_2Fe_2O_5 + 3H_2$ (R8)

Steam tar reforming: $C_nH_m + 2nH_2O \rightarrow \left(n + \frac{m}{2}\right) H_2 + nCO_2$ (R9)

$steam\ biochar\ reaction\ (primary)$: $C + H_2O \rightarrow CO + H_2$ (R10)

$steam\ biochar\ reaction\ (secondary)$: $C + 2H_2O \rightarrow CO_2 + 2H_2$ (R11)

$water\ gas\ shift$: $CO + H_2O \rightarrow CO_2 + H_2$ (R12)

$steam\ methane\ reforming$: $CH_4 + H_2O \rightarrow CO + 3H_2$ (R13)

$Boudouard\ reaction$: $C + CO_2 \rightarrow 2CO$ (R14)

$methanation$: $C + 2H_2 \rightarrow CH_4$ (R15)

The $Ca_2Fe_2O_5$ catalyst significantly alters the reaction pathway during steam gasification. Firstly, reduced $Ca_2Fe_2O_5$ from the pyrolysis stage undergoes oxidation by steam, leading to increased H_2 concentration and yield. Secondly, the water gas shift reaction ($CO + H_2O \rightarrow CO_2 + H_2$) becomes the dominant pathway, generating CO while simultaneously reducing the re-oxidized catalyst. This reduction-oxidation cycle involving the catalyst and steam promotes the formation of Fe^{3+} cations, facilitating an "inner looping" mechanism. This mechanism enables the continuous conversion of biochar through the redox reactions. Notably, the $Ca_2Fe_2O_5$ catalyst remains stable throughout the process, allowing for its reusability in subsequent outer looping experiments.

4.3.1 Effect of temperature on chemical looping gasification

The impact of temperature on the chemical looping gasification of biomass is evident from the experimental results presented in Figure 23. As the temperature increases from 650°C to 850°C, there is a notable enhancement in the production of gases such as H_2, CO, CH_4, and CO_2.

For instance, in the absence of a catalyst, at 650°C, the mol/kg of gas produced is 8.99 for H_2, 1.18 for CO, 1.16 for CH_4, and 4.28 for CO_2. As the temperature rises to 850°C, these values increase substantially to 25.19 for H_2, 2.61 for CO, 2.01 for CH_4, and 8.05 for CO_2. This escalation indicates the favorable effect of elevated temperatures on gas production during the chemical looping gasification process.

Moreover, the temperature effect is also observed in the presence of different oxygen carriers. Taking $Ca_2Fe_2O_5$ as an example, at 650°C, the mol/kg of gas produced is 13.01 for H_2, 0.97 for CO, 1.05 for CH_4, and 3.14 for CO_2, which significantly increases to 27.82 for H_2, 2.84 for CO, 2.26 for CH_4, and 8.14 for CO_2 at 850°C. This trend underscores the significance of temperature in enhancing gas yields across various catalysts.

4.3.2 Effect of oxygen carrier on chemical looping gasification

The influence of catalysts on the chemical looping gasification of biomass is evident from the comparative analysis of different oxygen carriers (Figure 22). The introduction of catalysts such as $Ca_2Fe_{1.9}Cu_{0.1}O_5$, $Ca_2Fe_{1.9}Co_{0.1}O_5$, and $Ca_2Fe_{1.9}Ni_{0.1}O_5$ has a discernible impact on gas production, particularly in terms of the composition and quantity of gases generated.

For instance, considering $Ca_2Fe_{1.9}Cu_{0.1}O_5$ at 650°C, the mol/kg of gas produced is 9.56 for H_2, 0.76 for CO, 1.50 for CH_4, and 4.55 for CO_2. In comparison, with $Ca_2Fe_{1.9}Ni_{0.1}O_5$ under the same conditions, the production yields are 13.54 for H_2, 0.98 for CO, 1.49 for CH_4, and 4.91 for CO_2. This suggests that the catalyst composition significantly affects gas generation, with variations observed in the quantities of H_2, CO, CH_4, and CO_2.

Furthermore, the effect of catalysts becomes more pronounced as the temperature increases. For example, with $Ca_2Fe_{1.9}Co_{0.1}O_5$ at 850°C, the mol/kg of gas produced is 32.05 for H_2, 2.41 for CO, 1.21 for CH_4, and 8.97 for CO_2, showcasing the catalytic influence on gas production at higher temperatures.

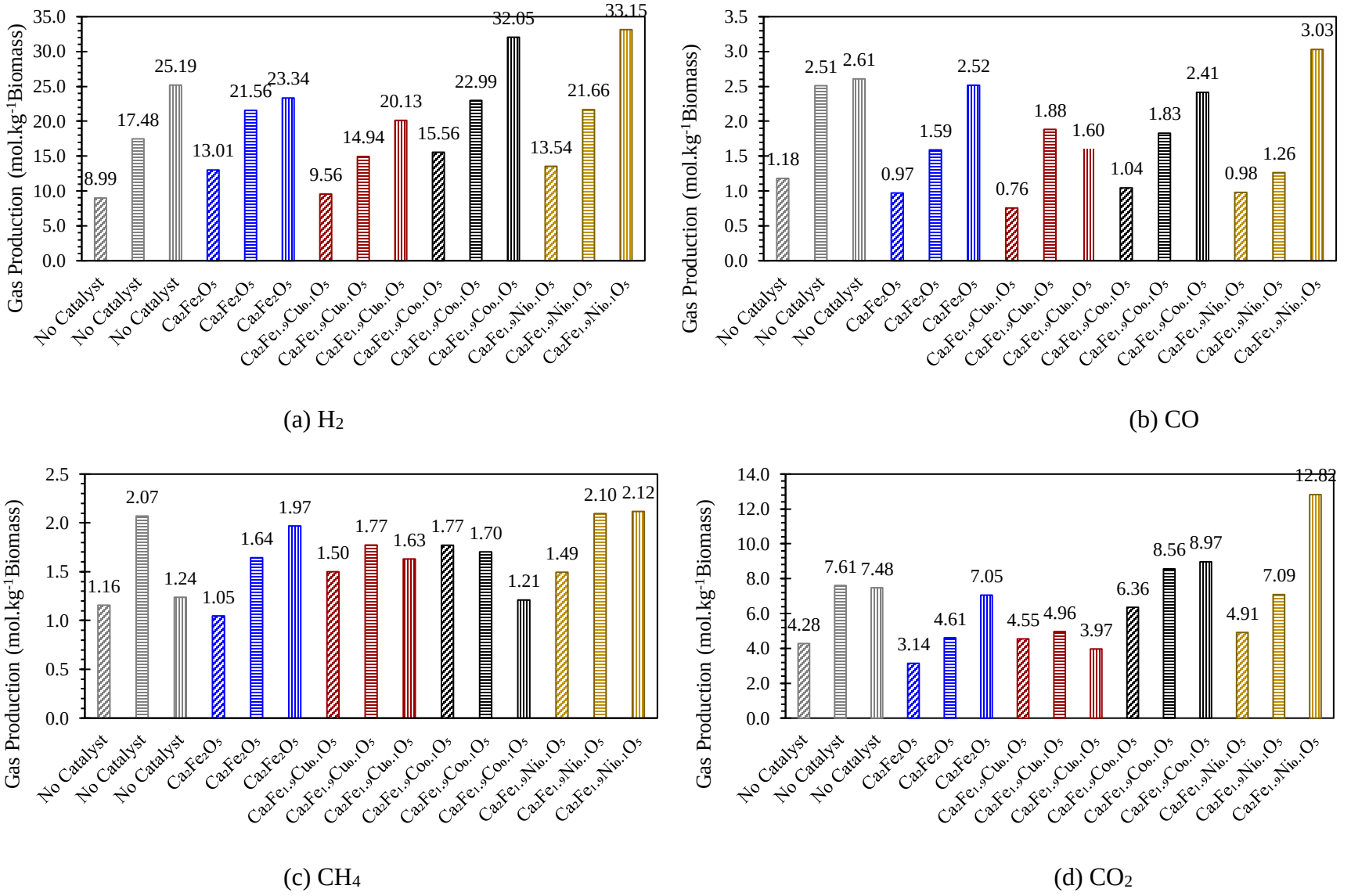

Figure 22: Effect of doping $Ca_2Fe_2O_5$ with Cu, Co and Ni on gas composition and production during gasification.

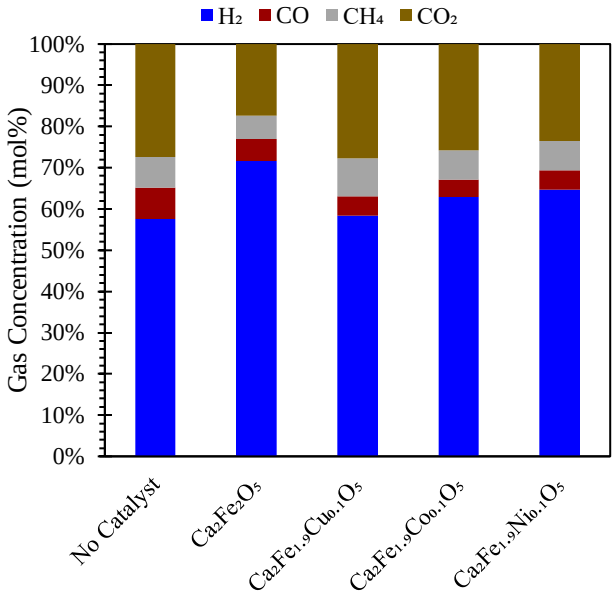
H₂
CO
CH₄
CO₂
Gas Concentration (mol%)
100%
90%
80%
70%
60%
50%
40%
30%
20%
10%
0%
No Catalyst
Ca2Fe2O5
Ca2Fe1.9Cu0.1O5
Ca2Fe1.9Co0.1O5
Ca2Fe1.9Ni0.1O5

(a) 650 °C

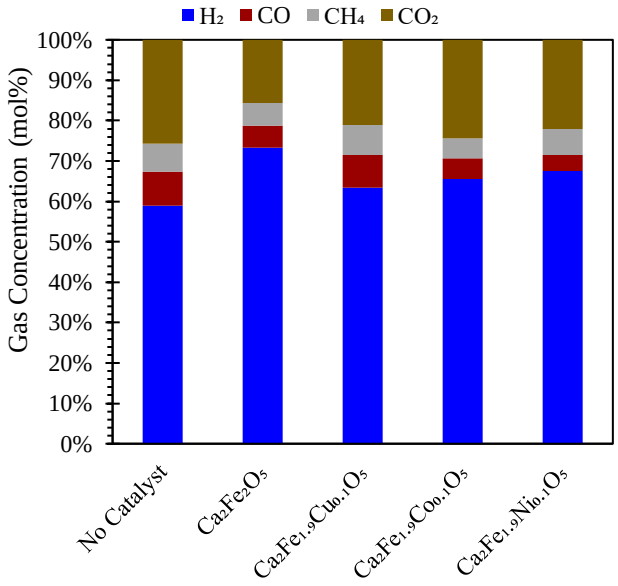
H₂
CO
CH₄
CO₂
Gas Concentration (mol%)
100%
90%
80%
70%
60%
50%
40%
30%
20%
10%
0%
No Catalyst
Ca2Fe2O5
Ca2Fe1.9Cu0.1O5
Ca2Fe1.9Co0.1O5
Ca2Fe1.9Ni0.1O5

(a) 750 °C

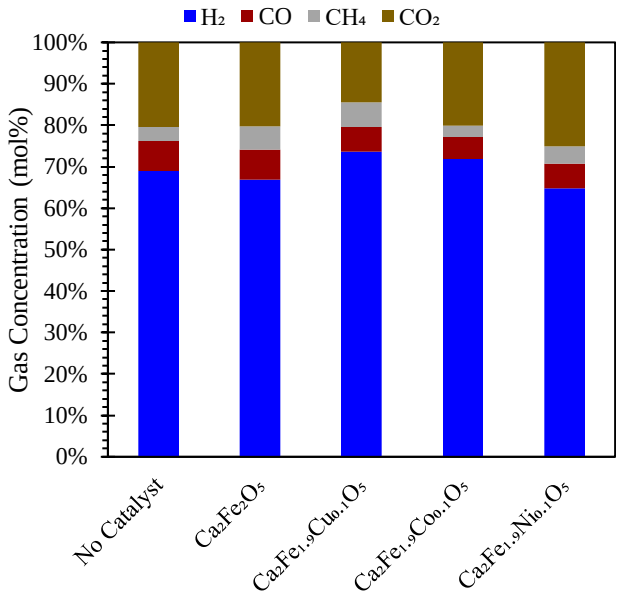

(a) 850 °C

Figure 23: Gas composition and total gas production during gasification stage at different temperatures.

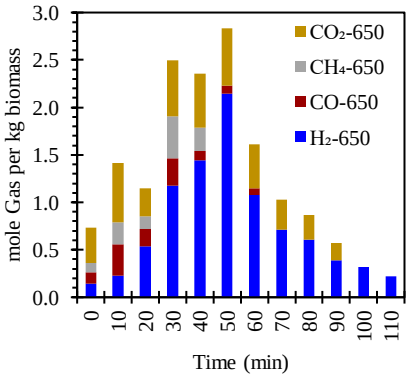

(a) No Catalyst, 650 °C

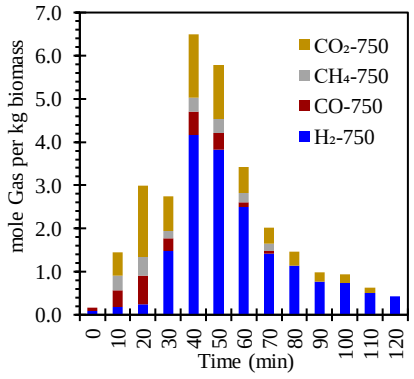

(a) No Catalyst, 750 °C

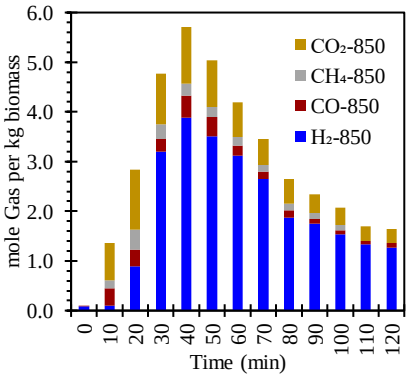

(a) No Catalyst, 850 °C

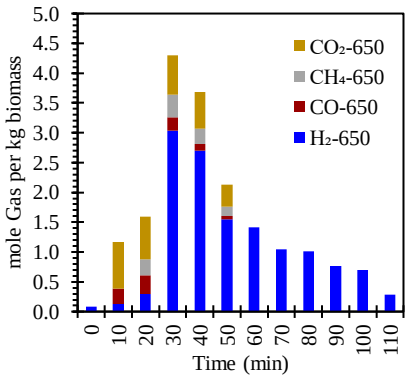

(b) $Ca_2Fe_2O_5$, 650 °C

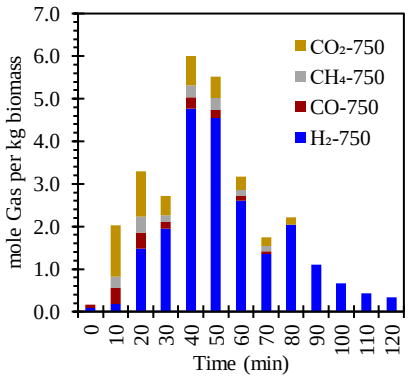

(b) $Ca_2Fe_2O_5$, 750 °C

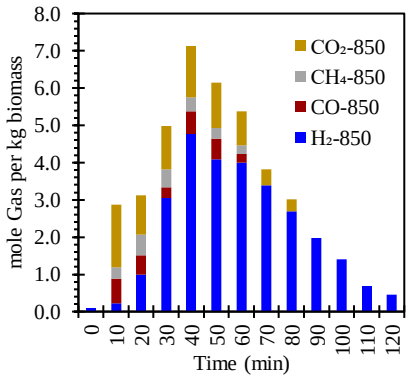

(b) $Ca_2Fe_2O_5$, 850 °C

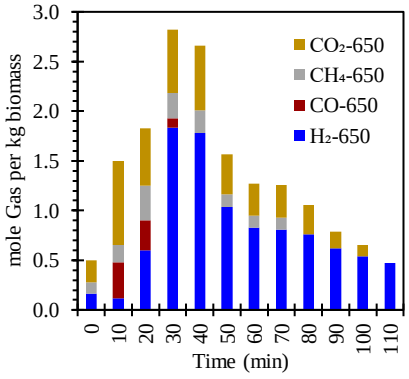

(c) $Ca_2Fe_{1.9}Cu_{0.1}O_5$, 650 °C

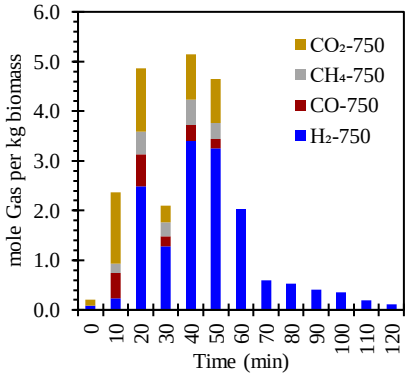

(c) $Ca_2Fe_{1.9}Cu_{0.1}O_5$, 750 °C

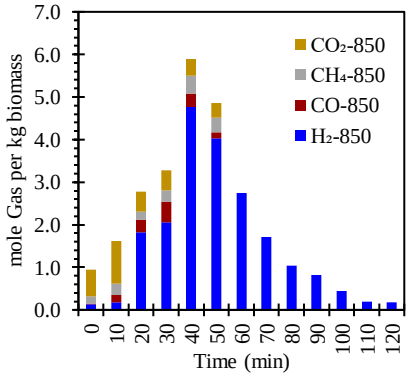

(c) $Ca_2Fe_{1.9}Cu_{0.1}O_5$, 850 °C

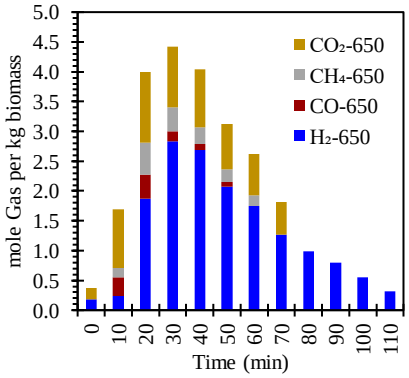

(d) $Ca_2Fe_{1.9}Co_{0.1}O_5$, 650 °C

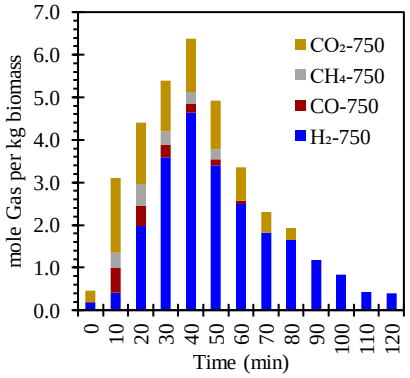

(d) $Ca_2Fe_{1.9}Co_{0.1}O_5$, 750 °C

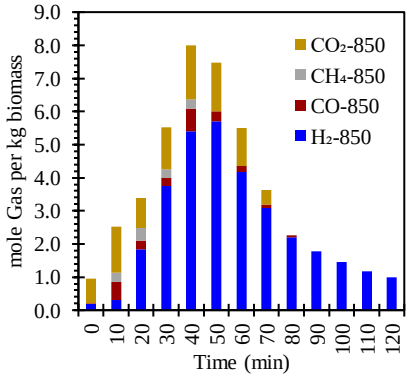

(d) $Ca_2Fe_{1.9}Co_{0.1}O_5$, 850 °C

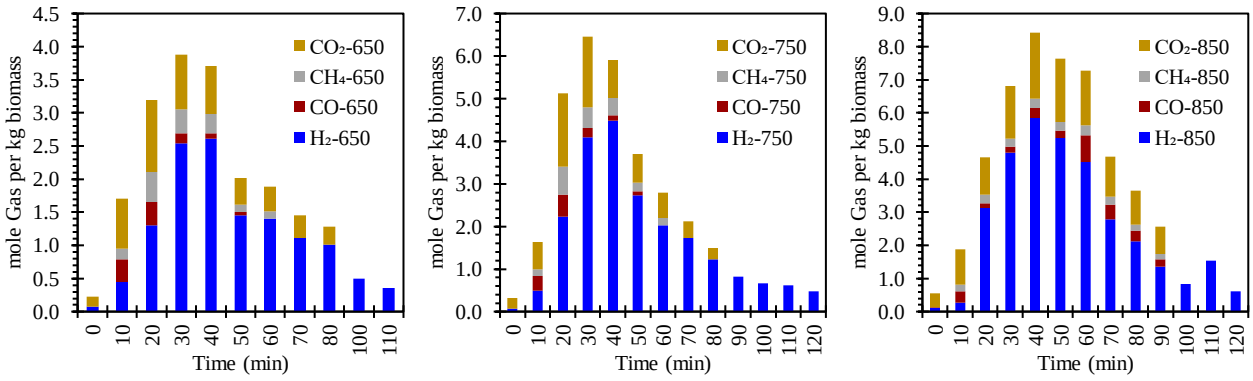

(e) $Ca_2Fe_{1.9}Ni_{0.1}O_5$, 650 °C (e) $Ca_2Fe_{1.9}Ni_{0.1}O_5$, 750 °C (e) $Ca_2Fe_{1.9}Ni_{0.1}O_5$, 850 °C

Figure 24: Syngas concentration and yields from miscanthus gasification using pure biomass, $Ca_2Fe_2O_5$, $Ca_2Fe_{1.9}Cu_{0.1}O_5$, $Ca_2Fe_{1.9}Co_{0.1}O_5$, and $Ca_2Fe_{1.9}Ni_{0.1}O_5$.

4.4 Biochar asphalt mix

Asphalt binder is one of the most commonly used materials in the paving industry for road and airport pavement infrastructures. This durable, cost-effective material boasts impressive application, and swift build times keep the world moving. However, as cities and countries undergo extensive development globally, asphalt pavement is increasingly susceptible to cracking, rutting, moisture damage, and other forms of degradation when subjected to dynamic loads and extreme weather conditions (Hemmati et al., 2023). These challenges pose a threat to the quality and safety of roads, necessitating additional maintenance and reconstruction efforts. Derived as a byproduct of refineries, asphalt is a complex material characterized by unique viscoelastic properties attributed to its high content of asphaltenes and resins. This viscoelastic nature renders it an ideal blend with aggregates for diverse load-bearing applications. It's crucial to acknowledge that the effectiveness of asphalt's viscoelasticity is confined to a specific temperature range. Beyond this range, be it too high or too low temperatures, the asphalt binder is more prone to defects and diminished durability (Hemmati et al., 2022). The asphalt industry

has been committed to reducing greenhouse gas emissions since the 1990s, driven by increasing concerns about environmental issues such as global warming and carbon footprint (Caputo et al., 2020). One notable initiative involves blending asphalt with biochar, where carbon remains stable in biochar's structure for 10^2 to 10^7 years. Therefore, incorporating biochar into asphalt binder contributes to reducing the construction industry's carbon footprint by securely trapping carbon within the infrastructure.

The produced biochar was crushed and sieved into three different particles sizes of 50, 100 and 150 mm. This was then mixed with the PG 64-22 asphalt binder. Biochar percentages used were 2%, 4% and 6% by weight of asphalt. Then, the biochar and matrix asphalt were subjected to three different mixing protocols summarized in Table 8 using a high-speed shearing machine (Eurostar 200 controller).

Table 8: Mixing Protocols considered for binder mix

Mixing Protocol	RPM	Temperature (°C)	Duration (min)
M1	1100	163	5
M2	1100	135	30
M3	1100	150	30

The mixed samples were poured into cigar tubes and cut into three sections—top, middle, and bottom. These sections then underwent dynamic shear rheometer (DSR) tests to determine which mixing protocol yielded the highest-grade binder mix.

As a result of the superior performance grade observed in the 6% biochar asphalt mixture created through mixing protocol 3, all subsequent tests were conducted under consistent conditions: an RPM of 1100 at 163°C for 30 minutes. Ten samples were examined, including neat asphalt, as well as asphalt with 6% biochar produced at temperatures of 550, 650, and 750 °C, with particle sizes of 50, 100, and 150 μm.

Standard laboratory procedures were employed to simulate the aging process asphalt undergoes throughout its lifespan. The rolling thin film oven (RTFO) test (ASTM D2872) mimics the short-term aging that occurs during production, transportation, and construction. First, 35 g of the sample are poured into a glass bottle and placed in a preheated Despatch oven maintained at 325°F (163°C) for 85 minutes. During this process, the bottles rotate continuously, ensuring the asphalt evenly coats the inner surface and forms a thin film of approximately 1.25 millimeters. Additionally, hot air is continuously injected into the bottles at a rate of 4 liters per minute to accelerate the aging process.

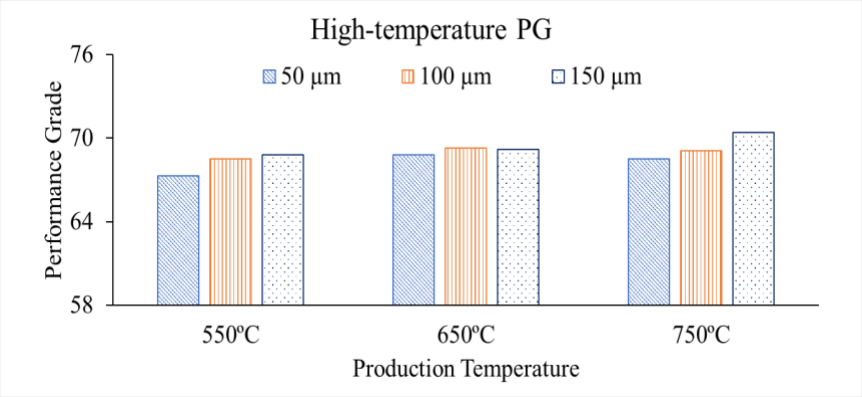

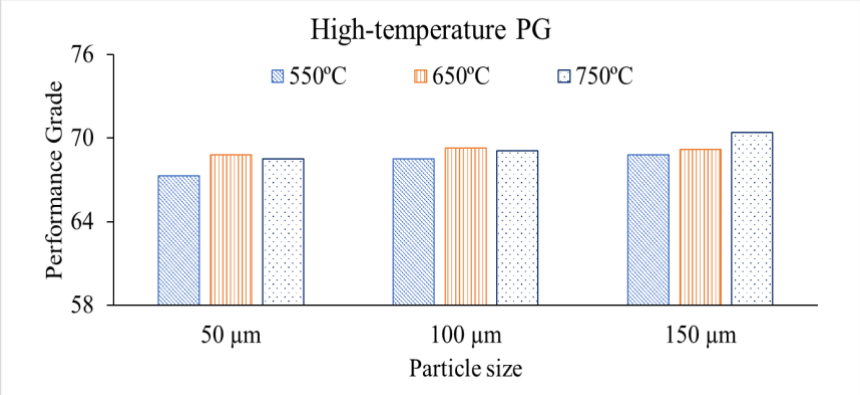

Figure 25: Effect of particle size and production temperature on asphalt performance grade

The incorporation of biochar into the asphalt mixture resulted in enhanced performance in both dynamic shear rheometer (DSR) grading and high-temperature rolling thin film oven (RTFO) testing

CHAPTER 6: CONCLUSIONS

This study investigated the influence of $Ca_2Fe_2O_5$ catalysts doped with Co, Ni, and Cu on the chemical looping gasification of Miscanthus biomass for enhanced H_2 production purity. Employing 350 gas chromatography analyses, we compared pyrolysis and gasification performance with and without catalysts at various temperatures. Sol-gel synthesized catalysts exhibited uniform elemental distribution, resulting in consistent influence on gasification.

A comparison between pyrolysis and gasification revealed that steam oxidation of the reduced oxygen carrier significantly enhanced H_2 production through a synergistic reaction. A 0.1 mL/min steam injection rate increased H_2 yield by 82.4% for the best performing Ni-doped catalyst ($Ca_2Fe_{1.9}Ni_{0.1}O_5$). Increasing temperature consistently led to higher H_2 yield. Doping with Ni and Co proved particularly effective, enhancing H_2 yield from 27.82 g/mol biomass (undoped) to 33.15 g/mol biomass (Ni) and 32.05 g/mol biomass (Co), respectively. These findings demonstrate the potential of sol-gel synthesized $Ca_2Fe_2O_5$ catalysts doped with Ni and Co for promoting H_2 production purity in chemical looping gasification of biomass, particularly when combined with steam injection.

Furthermore, this study successfully developed a valuable application for biochar. Cigar tube tests revealed that Mixing Protocol 3 produces uniform binder blends with biochar, leading to improved high-temperature performance grade and potentially enhanced rutting resistance. Additionally, biochar particle size significantly impacted the performance grade of the binder blends, while increasing production temperature showed a slight positive effect.

References

Abad, A., Cabello, A., Gayán, P., García-Labiano, F., de Diego, L. F., Mendiara, T., & Adánez, J. (2020). Kinetics of CaMn0.775Ti0.125Mg0.1O2.9-δ perovskite prepared at industrial scale and its implication on the performance of chemical looping combustion of methane. *Chemical Engineering Journal*, *394*, 124863. https://doi.org/https://doi.org/10.1016/j.cej.2020.124863

Abuelgasim, S., Wang, W., & Abdalazeez, A. (2021). A brief review for chemical looping combustion as a promising CO2 capture technology: Fundamentals and progress. *Science of The Total Environment*, *764*, 142892. https://doi.org/https://doi.org/10.1016/j.scitotenv.2020.142892

Adanez, J., Abad, A., Garcia-Labiano, F., Gayan, P., & de Diego, L. F. (2012). Progress in Chemical-Looping Combustion and Reforming technologies. *Progress in Energy and Combustion Science*, *38*(2), 215-282. https://doi.org/https://doi.org/10.1016/j.pecs.2011.09.001

Anthony, E. J., & Symonds, R. T. (2022). Chemical Looping Technology. In M. Lackner, B. Sajjadi, & W.-Y. Chen (Eds.), *Handbook of Climate Change Mitigation and Adaptation* (pp. 1689-1723). Springer International Publishing. https://doi.org/10.1007/978-3-030-72579-2_42

Assirey, E. A. R. (2019). Perovskite synthesis, properties and their related biochemical and industrial application. *Saudi Pharmaceutical Journal*, *27*(6), 817-829. https://doi.org/https://doi.org/10.1016/j.jsps.2019.05.003

Bai, X., Xie, G., Guo, Y., Tian, L., El-Hosainy, H. M., Awadallah, A. E., Ji, S., & Wang, Z.-j. (2021). A highly active Ni catalyst supported on Mg-substituted LaAlO3 for carbon dioxide reforming of methane. *Catalysis Today*, *368*, 78-85. https://doi.org/https://doi.org/10.1016/j.cattod.2019.12.033

Basavarajappa, M. G., & Chakraborty, S. (2022). Rationalization of Double Perovskite Oxides as Energy Materials: A Theoretical Insight from Electronic and Optical Properties. *ACS Materials Au*, *2*(6), 655-664. https://doi.org/10.1021/acsmaterialsau.2c00031

Berestova, T. V., Khursan, S. L., & Mustafin, A. G. (2020). Experimental and theoretical substantiation of differences of geometric isomers of copper(II) α-amino acid chelates in ATR-FTIR spectra. *Spectrochimica Acta Part A: Molecular and Biomolecular Spectroscopy*, *229*, 117950. https://doi.org/https://doi.org/10.1016/j.saa.2019.117950

Bergmann, F. (1897). Process for the production of calcium carbide in blast furnaces. *German Patent*, *29*, *384*.

Bertoldi, J., de Campos Roseno, K. T., Schmal, M., Lage, V. D., Lenzi, G. G., & Brackmann, R. (2022). La1−x(Ce, Sr)xNiO3 perovskite-type oxides as catalyst precursors to syngas production through tri-reforming of methane. *International Journal of Hydrogen Energy*, *47*(73), 31279-31294. https://doi.org/https://doi.org/10.1016/j.ijhydene.2022.07.053

Cabello, A., Abad, A., Gayán, P., de Diego, L. F., García-Labiano, F., & Adánez, J. (2014). Effect of Operating Conditions and H2S Presence on the Performance of CaMg0.1Mn0.9O3−δ Perovskite Material in Chemical Looping Combustion (CLC). *Energy & Fuels*, *28*(2), 1262-1274. https://doi.org/10.1021/ef4020718

Cabello, A., Abad, A., Gayán, P., García-Labiano, F., de Diego, L. F., & Adánez, J. (2021). Increasing energy efficiency in chemical looping combustion of methane by in-situ activation of perovskite-based oxygen carriers. *Applied Energy*, *287*, 116557. https://doi.org/https://doi.org/10.1016/j.apenergy.2021.116557

Cao, D., Ding, H., Luo, C., Wu, F., Li, X., & Zhang, L. (2021). Development of a cordierite monolith reactor coated with CeO2-supported BaSrCo-based perovskite for chemical looping steam methane reforming. *Fuel Processing Technology*, *220*, 106889. https://doi.org/https://doi.org/10.1016/j.fuproc.2021.106889

Cao, D., Luo, C., Luo, T., Shi, Z., Wu, F., Li, X., Zheng, Y., & Zhang, L. (2023). Dry reforming of methane by La2NiO4 perovskite oxide, part I: Preparation and characterization of the samples.

Fuel Processing Technology, *247*, 107765. https://doi.org/https://doi.org/10.1016/j.fuproc.2023.107765
Cao, D., Luo, C., Wu, F., Zhang, L., & Li, X. (2022). Screening loaded perovskite oxygen carriers for chemical looping steam methane reforming. *Journal of Environmental Chemical Engineering*, *10*(2), 107315. https://doi.org/https://doi.org/10.1016/j.jece.2022.107315
Cao, D., Luo, C., Xing, W., Cai, G., Luo, T., Wu, F., Li, X., & Zhang, L. (2022). Coal-direct chemical looping hydrogen generation with BaMnO3 perovskite oxygen carrier. *Fuel Processing Technology*, *233*, 107296. https://doi.org/https://doi.org/10.1016/j.fuproc.2022.107296
Cao, Y., Liang, J., Li, X., Yue, L., Liu, Q., Lu, S., Asiri, A. M., Hu, J., Luo, Y., & Sun, X. (2021). Recent advances in perovskite oxides as electrode materials for supercapacitors [10.1039/D0CC07970G]. *Chemical Communications*, *57*(19), 2343-2355. https://doi.org/10.1039/D0CC07970G
Caputo, P., Abe, A. A., Loise, V., Porto, M., Calandra, P., Angelico, R., & Oliviero Rossi, C. (2020). The Role of Additives in Warm Mix Asphalt Technology: An Insight into Their Mechanisms of Improving an Emerging Technology. *Nanomaterials (Basel)*, *10*(6). https://doi.org/10.3390/nano10061202
Chen, C., Yu, W., Duan, Y., Wang, X., & Zhang, J. (2020). Chlorine-promoted perovskite nanocomposite as a high-performance oxygen transfer agent for chemical looping methane-assisted CO2 splitting. *Chemical Engineering Journal Advances*, *4*, 100052. https://doi.org/https://doi.org/10.1016/j.ceja.2020.100052
Chen, J., Zhao, K., Zhao, Z., He, F., Huang, Z., Wei, G., & Xia, C. (2019). Reaction schemes of barium ferrite in biomass chemical looping gasification for hydrogen-enriched syngas generation via an outer-inner looping redox reaction mechanism. *Energy Conversion and Management*, *189*, 81-90. https://doi.org/https://doi.org/10.1016/j.enconman.2019.03.084
Chen, X., Wang, L., Lin, Y., Zeng, T., Huang, Z., Zhang, Y., Xiong, Y., Li, J., Deng, L., & Huang, H. (2023). Migration of lattice oxygen during chemical looping dry reforming of methane with Ca2Fe2O5/Zr0.5Ce0.5O2 oxygen carrier. *Fuel Processing Technology*, *244*, 107706. https://doi.org/https://doi.org/10.1016/j.fuproc.2023.107706
Cheng, Z., & Lin, J. (2010). Layered organic–inorganic hybrid perovskites: structure, optical properties, film preparation, patterning and templating engineering [10.1039/C001929A]. *CrystEngComm*, *12*(10), 2646-2662. https://doi.org/10.1039/C001929A
Choi, Y.-K., Gurav, R., Kim, H. J., Yang, Y.-H., & Bhatia, S. K. (2020). Evaluation for Simultaneous Removal of Anionic and Cationic Dyes onto Maple Leaf-Derived Biochar Using Response Surface Methodology. *Applied Sciences*, *10*(9), 2982. https://www.mdpi.com/2076-3417/10/9/2982
Condori, O., de Diego, L. F., Garcia-Labiano, F., Izquierdo, M. T., Abad, A., & Adánez, J. (2021). Syngas Production in a 1.5 kW(th) Biomass Chemical Looping Gasification Unit Using Fe and Mn Ores as the Oxygen Carrier. *Energy Fuels*, *35*(21), 17182-17196. https://doi.org/10.1021/acs.energyfuels.1c01878
Condori, O., García-Labiano, F., de Diego, L. F., Izquierdo, M. T., Abad, A., & Adánez, J. (2021). Biomass chemical looping gasification for syngas production using ilmenite as oxygen carrier in a 1.5 kWth unit. *Chemical Engineering Journal*, *405*, 126679. https://doi.org/https://doi.org/10.1016/j.cej.2020.126679
Coppola, A., & Scala, F. (2021). Chemical Looping for Combustion of Solid Biomass: A Review. *Energy & Fuels*, *35*(23), 19248-19265. https://doi.org/10.1021/acs.energyfuels.1c02600
Cui, X., Wang, J., Cao, J.-P., Zhao, P.-T., Wang, Y.-X., Yan, H., & Huang, N. (2020). Effect of A-site disubstituted of lanthanide perovskite on catalytic activity and reaction kinetics analysis of coal combustion. *Fuel*, *260*, 116380. https://doi.org/https://doi.org/10.1016/j.fuel.2019.116380
Dai, X., Cheng, J., Li, Z., Liu, M., Ma, Y., & Zhang, X. (2016). Reduction kinetics of lanthanum ferrite perovskite for the production of synthesis gas by chemical-looping methane reforming. *Chemical Engineering Science*, *153*, 236-245. https://doi.org/https://doi.org/10.1016/j.ces.2016.07.011

Dawa, T., & Sajjadi, B. (2024). Exploring the potential of perovskite structures for chemical looping technology: A state-of-the-art review. *Fuel Processing Technology*, *253*, 108022. https://doi.org/10.1016/j.fuproc.2023.108022

de Santana Santos, M., Frety, R., Lisi, L., Cimino, S., & Teixeira Brandão, S. (2021). LaNi1-xCoxO3 perovskites for methane combustion by chemical looping. *Fuel*, *292*, 120187. https://doi.org/https://doi.org/10.1016/j.fuel.2021.120187

Ding, H., Jin, Y., Hawkins, S. C., Zhang, L., & Luo, C. (2023). Development and performance of CeO2 supported BaCoO3−δ perovskite for chemical looping steam methane reforming. *Fuel Processing Technology*, *239*, 107546. https://doi.org/https://doi.org/10.1016/j.fuproc.2022.107546

Ding, H., Luo, C., Li, X., Cao, D., Shen, Q., & Zhang, L. (2019). Development of BaSrCo-based perovskite for chemical-looping steam methane reforming: A study on synergistic effects of A-site elements and CeO2 support. *Fuel*, *253*, 311-319. https://doi.org/https://doi.org/10.1016/j.fuel.2019.04.150

Ding, H., Xu, Y., Luo, C., Zheng, Y., Shen, Q., Liu, Z., & Zhang, L. (2016). Synthesis and characteristics of BaSrCoFe-based perovskite as a functional material for chemical looping gasification of coal. *International Journal of Hydrogen Energy*, *41*(48), 22846-22855. https://doi.org/https://doi.org/10.1016/j.ijhydene.2016.11.005

Fan, L.-S. (2017). *Chemical looping partial oxidation: gasification, reforming, and chemical syntheses*. Cambridge University Press.

Fang, F., Feng, N., Wang, L., Meng, J., Liu, G., Zhao, P., Gao, P., Ding, J., Wan, H., & Guan, G. (2018). Fabrication of perovskite-type macro/mesoporous La1-xKxFeO3-δ nanotubes as an efficient catalyst for soot combustion. *Applied Catalysis B: Environmental*, *236*, 184-194. https://doi.org/https://doi.org/10.1016/j.apcatb.2018.05.030

García-García, F. R., & Metcalfe, I. S. (2021). Chemical looping dry reforming of methane using mixed oxides of iron and cerium: Operation window. *Catalysis Communications*, *160*, 106356. https://doi.org/https://doi.org/10.1016/j.catcom.2021.106356

He, F., Chen, J., Liu, S., Huang, Z., Wei, G., Wang, G., Cao, Y., & Zhao, K. (2019). La1-xSrxFeO3 perovskite-type oxides for chemical-looping steam methane reforming: Identification of the surface elements and redox cyclic performance. *International Journal of Hydrogen Energy*, *44*(21), 10265-10276. https://doi.org/https://doi.org/10.1016/j.ijhydene.2019.03.002

He, F., Li, X., Zhao, K., Huang, Z., Wei, G., & Li, H. (2013). The use of La1−xSrxFeO3 perovskite-type oxides as oxygen carriers in chemical-looping reforming of methane. *Fuel*, *108*, 465-473. https://doi.org/https://doi.org/10.1016/j.fuel.2012.11.035

He, F., Zhao, K., Huang, Z., Li, X. a., Wei, G., & Li, H. (2013). Synthesis of three-dimensionally ordered macroporous LaFeO3 perovskites and their performance for chemical-looping reforming of methane. *Chinese Journal of Catalysis*, *34*(6), 1242-1249. https://doi.org/https://doi.org/10.1016/S1872-2067(12)60563-4

Hemmati, N., Vigneswaran, S., Kim, H. H., Lee, M. S., & Lee, S. J. (2023). Laboratory Evaluation of Asphalt Binders Containing Styrene-Butadiene-Styrene (SBS) and Processed Oil. *Materials (Basel)*, *16*(3). https://doi.org/10.3390/ma16031235

Hemmati, N., Yun, J., Kim, H., Lee, M.-S., & Lee, S.-J. (2022). Effect of Processed Oil on Asphalt Binder Properties. *Materials*, *15*(11), 3739. https://www.mdpi.com/1996-1944/15/11/3739

Hu, Q., Shen, Y., Chew, J. W., Ge, T., & Wang, C.-H. (2020). Chemical looping gasification of biomass with Fe2O3/CaO as the oxygen carrier for hydrogen-enriched syngas production. *Chemical Engineering Journal*, *379*, 122346. https://doi.org/https://doi.org/10.1016/j.cej.2019.122346

Hu, X., & Gholizadeh, M. (2019). Biomass pyrolysis: A review of the process development and challenges from initial researches up to the commercialisation stage. *Journal of Energy Chemistry*, *39*, 109-143. https://doi.org/https://doi.org/10.1016/j.jechem.2019.01.024

Jerndal, E., Mattisson, T., & Lyngfelt, A. (2006). Thermal Analysis of Chemical-Looping Combustion. *Chemical Engineering Research and Design*, *84*(9), 795-806. https://doi.org/https://doi.org/10.1205/cherd05020

Jiang, Q., Cao, Y., Liu, X., Zhang, H., Hong, H., & Jin, H. (2020). Chemical Looping Combustion over a Lanthanum Nickel Perovskite-Type Oxygen Carrier with Facilitated O2− Transport. *Energy & Fuels*, *34*(7), 8732-8739. https://doi.org/10.1021/acs.energyfuels.0c01038

Jiang, Q., Zhang, H., Cao, Y., Hong, H., & Jin, H. (2019). Solar hydrogen production via perovskite-based chemical-looping steam methane reforming. *Energy Conversion and Management*, *187*, 523-536. https://doi.org/https://doi.org/10.1016/j.enconman.2019.01.112

Jiang, Q., Zhang, H., Deng, Y. n., Kang, Q., Hong, H., & Jin, H. (2018). Properties and reactivity of LaCuxNi1−xO3 perovskites in chemical-looping combustion for mid-temperature solar-thermal energy storage. *APPLIED ENERGY*, *228*, 1506-1514. https://doi.org/https://doi.org/10.1016/j.apenergy.2018.07.028

Källén, M., Rydén, M., Dueso, C., Mattisson, T., & Lyngfelt, A. (2013). CaMn0.9Mg0.1O3-δ as Oxygen Carrier in a Gas-Fired 10 kWthChemical-Looping Combustion Unit. *Industrial & Engineering Chemistry Research*, *52*(21), 6923-6932. https://doi.org/10.1021/ie303070h

King, G., & Woodward, P. M. (2010). Cation ordering in perovskites [10.1039/B926757C]. *Journal of Materials Chemistry*, *20*(28), 5785-5796. https://doi.org/10.1039/B926757C

Ksepko, E. (2018). Perovskite Sr(Fe1-xCux)O3-δ materials for chemical looping combustion applications. *International Journal of Hydrogen Energy*, *43*(20), 9622-9634. https://doi.org/https://doi.org/10.1016/j.ijhydene.2018.04.046

Kwong, K. Y., Harrison, A. R. P., Gebers, J. C., Dennis, J. S., & Marek, E. J. (2022). Chemical Looping Combustion of a Biomass Char in Fe2O3-, CuO-, and SrFeO3−δ-Based Oxygen Carriers. *Energy & Fuels*, *36*(17), 9437-9449. https://doi.org/10.1021/acs.energyfuels.2c01269

Lee, M., Lim, H. S., Kim, Y., & Lee, J. W. (2020). Enhancement of highly-concentrated hydrogen productivity in chemical looping steam methane reforming using Fe-substituted LaCoO3. *Energy Conversion and Management*, *207*, 112507. https://doi.org/https://doi.org/10.1016/j.enconman.2020.112507

Leion, H., Lyngfelt, A., Johansson, M., Jerndal, E., & Mattisson, T. (2008). The use of ilmenite as an oxygen carrier in chemical-looping combustion. *Chemical Engineering Research and Design*, *86*(9), 1017-1026. https://doi.org/https://doi.org/10.1016/j.cherd.2008.03.019

Li, D., Xu, R., Li, X., Li, Z., Zhu, X., & Li, K. (2020). Chemical Looping Conversion of Gaseous and Liquid Fuels for Chemical Production: A Review. *Energy & Fuels*, *34*(5), 5381-5413. https://doi.org/10.1021/acs.energyfuels.0c01006

Li, J., Zhang, H., Gao, Z., Fu, J., Ao, W., & Dai, J. (2017). CO2 Capture with Chemical Looping Combustion of Gaseous Fuels: An Overview. *Energy & Fuels*, *31*(4), 3475-3524. https://doi.org/10.1021/acs.energyfuels.6b03204

Li, M., Zhao, K., Zhao, Z., Li, H., He, F., & Lv, P. (2019). Enhanced hydrogen-rich syngas generation in chemical looping methane reforming using an interstitial doped La1.6Sr0.4FeCoO6. *International Journal of Hydrogen Energy*, *44*(21), 10250-10264. https://doi.org/https://doi.org/10.1016/j.ijhydene.2019.03.012

Li, X., Li, Z., Lu, C., Li, D., Li, Z., Gao, J., Wei, J., & Li, K. (2022). Enhanced performance of LaFeO3 oxygen carriers by NiO for chemical looping partial oxidation of methane. *Fuel Processing Technology*, *236*, 107396. https://doi.org/https://doi.org/10.1016/j.fuproc.2022.107396

Li, Z., Dong, X., Yan, B., Li, J., Wang, J., Jiao, L., Chen, G., Ahmed, S., & Cao, Y. (2022). Chemical looping gasification of digestate: Investigation on the surface and lattice oxygen of perovskite oxygen carrier. *Fuel*, *318*, 123663. https://doi.org/https://doi.org/10.1016/j.fuel.2022.123663

Lim, H. S., Kang, D., & Lee, J. W. (2017). Phase transition of Fe2O3–NiO to NiFe2O4 in perovskite catalytic particles for enhanced methane chemical looping reforming-decomposition with CO2

conversion. *Applied Catalysis B: Environmental*, *202*, 175-183. https://doi.org/https://doi.org/10.1016/j.apcatb.2016.09.020
Liu, C., Wang, W., & Chen, D. (2018). Hydrogen-Rich Syngas Production from Chemical Looping Gasification of Biomass Char with CaMn1–xFexO3. *Energy & Fuels*, *32*(9), 9541-9550. https://doi.org/10.1021/acs.energyfuels.8b01836
Liu, G., Liao, Y., Wu, Y., & Ma, X. (2018). Application of calcium ferrites as oxygen carriers for microalgae chemical looping gasification. *Energy Conversion and Management*, *160*, 262-272. https://doi.org/https://doi.org/10.1016/j.enconman.2018.01.041
Liu, G., Liao, Y., Wu, Y., & Ma, X. (2019a). Evaluation of Sr-substituted Ca2Fe2O5 as oxygen carrier in microalgae chemical looping gasification. *Fuel Processing Technology*, *191*, 93-103. https://doi.org/https://doi.org/10.1016/j.fuproc.2019.03.019
Liu, G., Liao, Y., Wu, Y., & Ma, X. (2019b). Reactivity of Co-doped Ca2Fe2O5 brownmillerite oxides as oxygen carriers for microalgae chemical looping gasification. *International Journal of Hydrogen Energy*, *44*(5), 2546-2559. https://doi.org/https://doi.org/10.1016/j.ijhydene.2018.11.232
Liu, Z., Wang, J., Cao, Y., Tao, J., Yan, B., & Chen, G. (2023). Mn-doping Ca2Fe2O5-based oxygen carriers in chemical looping gasification of biogas residue: A comprehensive study on the reaction mechanisms. *Fuel*, *332*, 126207. https://doi.org/https://doi.org/10.1016/j.fuel.2022.126207
Luo, S., & Daoud, W. (2014). Recent progress in organic-inorganic halide perovskite solar cells: Mechanisms and material design. *J. Mater. Chem. A*, *3*. https://doi.org/10.1039/C4TA04953E
Ma, J., Zhang, X., Peng, P., Tian, X., Li, M., Li, Y., Xu, Z., & Zhao, H. (2023). Converting ethane to syngas via chemical looping dry reforming with LaFeO3 perovskite oxygen carrier. *Fuel Processing Technology*, *247*, 107806. https://doi.org/https://doi.org/10.1016/j.fuproc.2023.107806
Ma, S., Chen, S., Soomro, A., & Xiang, W. (2017). Effects of supports on hydrogen production and carbon deposition of Fe-based oxygen carriers in chemical looping hydrogen generation. *International Journal of Hydrogen Energy*. https://doi.org/10.1016/j.ijhydene.2017.02.132
Mayer, K., Piesenberger, S., Penthor, S., Pröll, T., & Hofbauer, H. (2018). Chemical Looping Combustion Using Two Different Perovskite Based Oxygen Carriers: A Pilot Study. *Energy Technol (Weinh)*, *6*(12), 2333-2343. https://doi.org/10.1002/ente.201800244
Medeiros, R. L. B. A., Melo, V. R. M., Melo, D. M. A., Macedo, H. P., Moure, G. T., Adánez-Rubio, I., Melo, M. A. F., & Adánez, J. (2020). Double perovskite (La2-xCa-Bax)NiO4 oxygen carriers for chemical looping reforming applications. *International Journal of Hydrogen Energy*, *45*(3), 1681-1696. https://doi.org/https://doi.org/10.1016/j.ijhydene.2019.11.004
Mei, X., Xiong, J., Wei, Y., Zhang, Y., Zhang, P., Yu, Q., Zhao, Z., & Liu, J. (2020). High-efficient non-noble metal catalysts of 3D ordered macroporous perovskite-type La2NiB'O6 for soot combustion: Insight into the synergistic effect of binary Ni and B' sites. *Applied Catalysis B: Environmental*, *275*, 119108. https://doi.org/https://doi.org/10.1016/j.apcatb.2020.119108
Miller, D. D., & Siriwardane, R. (2018). CaFe2O4 oxygen carrier characterization during the partial oxidation of coal in the chemical looping gasification application. *Applied Energy*, *224*, 708-716. https://doi.org/https://doi.org/10.1016/j.apenergy.2018.05.035
Nalbandian, L., Evdou, A., & Zaspalis, V. (2011). La1−xSrxMyFe1−yO3−δ perovskites as oxygen-carrier materials for chemical-looping reforming. *International Journal of Hydrogen Energy*, *36*(11), 6657-6670. https://doi.org/https://doi.org/10.1016/j.ijhydene.2011.02.146
Nazari, M., Ghasemi, N., Khan, M. M., Rokni, M., & Taghavi, S. R. (2023). CuxMn1-xFe2O4 as oxygen carrier for chemical looping steam methane reforming. *Chemical Physics Impact*, *6*, 100191. https://doi.org/https://doi.org/10.1016/j.chphi.2023.100191
Neal, L., Shafiefarhood, A., & Li, F. (2015). Effect of core and shell compositions on MeOx@LaySr1−yFeO3 core–shell redox catalysts for chemical looping reforming of methane. *Applied Energy*, *157*, 391-398. https://doi.org/https://doi.org/10.1016/j.apenergy.2015.06.028

Oh, D., Colombo, F., Nodari, L., Kim, J. H., Kim, J. K., Lee, S., Kim, S., Kim, S., Lim, D.-K., Seo, J., Ahn, S., Mascotto, S., & Jung, W. (2023). Rocking chair-like movement of ex-solved nanoparticles on the Ni-Co doped La0.6Ca0.4FeO3-δ oxygen carrier during chemical looping reforming coupled with CO2 splitting. *Applied Catalysis B: Environmental*, *332*, 122745. https://doi.org/https://doi.org/10.1016/j.apcatb.2023.122745

Ono, L. K., Juarez-Perez, E. J., & Qi, Y. (2017). Progress on Perovskite Materials and Solar Cells with Mixed Cations and Halide Anions. *ACS Applied Materials & Interfaces*, *9*(36), 30197-30246. https://doi.org/10.1021/acsami.7b06001

Ozcan, H., El-Emam, R. S., & Amini Horri, B. (2023). Thermochemical looping technologies for clean hydrogen production – Current status and recent advances. *Journal of Cleaner Production*, *382*, 135295. https://doi.org/https://doi.org/10.1016/j.jclepro.2022.135295

Pachler, R. F., Penthor, S., Mayer, K., & Hofbauer, H. (2019). Fate of sulfur in chemical looping combustion of gaseous fuels using a Perovskite oxygen carrier. *Fuel*, *241*, 432-441. https://doi.org/https://doi.org/10.1016/j.fuel.2018.12.054

Padula, S., Tregambi, C., Troiano, M., Di Benedetto, A., Salatino, P., Landi, G., & Solimene, R. (2022). Chemical Looping Reforming with Perovskite-Based Catalysts for Thermochemical Energy Storage. *Energies*, *15*(22), 8556. https://www.mdpi.com/1996-1073/15/22/8556

Patience, G. S., & Bockrath, R. E. (2010). Butane oxidation process development in a circulating fluidized bed. *Applied Catalysis A: General*, *376*(1), 4-12. https://doi.org/https://doi.org/10.1016/j.apcata.2009.10.023

Qi, R., Jin, R., An, L., Bai, X., & Wang, Z.-j. (2022). A Ni/perovskite catalyst with low metal content for CO2 reforming of methane. *Catalysis Communications*, *163*, 106419. https://doi.org/https://doi.org/10.1016/j.catcom.2022.106419

Readman, J. E., Olafsen, A., Larring, Y., & Blom, R. (2005). La0.8Sr0.2Co0.2Fe0.8O3−δ as a potential oxygen carrier in a chemical looping type reactor, an in-situ powder X-ray diffraction study [10.1039/B416526H]. *Journal of Materials Chemistry*, *15*(19), 1931-1937. https://doi.org/10.1039/B416526H

Royer, S., Duprez, D., Can, F., Courtois, X., Batiot-Dupeyrat, C., Laassiri, S., & Alamdari, H. (2014). Perovskites as Substitutes of Noble Metals for Heterogeneous Catalysis: Dream or Reality. *Chemical Reviews*, *114*(20), 10292-10368. https://doi.org/10.1021/cr500032a

Ruan, Y., Zhao, Y., Lu, Y., Guo, D., Zhao, Y., Wang, S., & Ma, X. (2020). Mesoporous LaAl0.25Ni0.75O3 perovskite catalyst using SBA-15 as templating agent for methane dry reforming. *Microporous and Mesoporous Materials*, *303*, 110278. https://doi.org/https://doi.org/10.1016/j.micromeso.2020.110278

Sarshar, Z., & Kaliaguine, S. (2013). Reduction Kinetics of Perovskite-Based Oxygen Carriers for Chemical Looping Combustion. *Industrial & Engineering Chemistry Research*, *52*(21), 6946-6955. https://doi.org/10.1021/ie400766b

Sastre, D., Galván, C. Á., Pizarro, P., & Coronado, J. M. (2022). Enhanced performance of CH4 dry reforming over La0.9Sr0.1FeO3/YSZ under chemical looping conditions. *Fuel*, *309*, 122122. https://doi.org/https://doi.org/10.1016/j.fuel.2021.122122

Sastre, D., Serrano, D. P., Pizarro, P., & Coronado, J. M. (2019). Chemical insights on the activity of La1-xSrxFeO3 perovskites for chemical looping reforming of methane coupled with CO2-splitting. *Journal of CO2 Utilization*, *31*, 16-26. https://doi.org/https://doi.org/10.1016/j.jcou.2019.02.013

Shah, V., Cheng, Z., Baser, D. S., Fan, J. A., & Fan, L.-S. (2021). Highly Selective Production of Syngas from Chemical Looping Reforming of Methane with CO2 Utilization on MgO-supported Calcium Ferrite Redox Materials. *APPLIED ENERGY*, *282*, 116111. https://doi.org/https://doi.org/10.1016/j.apenergy.2020.116111

Shahnazi, A., & Firoozi, S. (2021). Improving the catalytic performance of LaNiO3 perovskite by manganese substitution via ultrasonic spray pyrolysis for dry reforming of methane. *Journal of CO2 Utilization*, *45*, 101455. https://doi.org/https://doi.org/10.1016/j.jcou.2021.101455

Sharma, A. (2019). *EXPERIMENTAL EVALUATION OF A CENTRIFUGAL PACKER-TYPE DOWNHOLE SEPARATOR*

Shen, X., Wu, Y., Xu, X., Su, J., He, Z., Jiang, E., Ren, Y., & Sun, Y. (2022). Torrefaction enhanced biomass chemical-looping gasification coupled with CO2-splitting via half doped LaFe0.5M0.5O3 perovskites. *Fuel Processing Technology*, *234*, 107314. https://doi.org/https://doi.org/10.1016/j.fuproc.2022.107314

Shen, Y., Zhao, K., He, F., & Li, H. (2019). The structure-reactivity relationships of using three-dimensionally ordered macroporous LaFe1−xNixO3 perovskites for chemical-looping steam methane reforming. *Journal of the Energy Institute*, *92*(2), 239-246. https://doi.org/https://doi.org/10.1016/j.joei.2018.01.012

Shen, Y., Zhao, K., He, F., & Li, H.-b. (2016). Synthesis of three-dimensionally ordered macroporous LaFe0.7Co0.3O3 perovskites and their performance for chemical-looping steam reforming of methane. *Journal of Fuel Chemistry and Technology*, *44*(10), 1168-1176. https://doi.org/https://doi.org/10.1016/S1872-5813(16)30051-2

Siriwardane, R., Riley, J., Tian, H., & Richards, G. (2016). Chemical looping coal gasification with calcium ferrite and barium ferrite via solid–solid reactions. *APPLIED ENERGY*, *165*, 952-966. https://doi.org/https://doi.org/10.1016/j.apenergy.2015.12.085

Solunke, R. D., & Veser, G. (2011). Integrating desulfurization with CO2-capture in chemical-looping combustion. *Fuel*, *90*(2), 608-617. https://doi.org/https://doi.org/10.1016/j.fuel.2010.09.039

Sun, R., Shen, L., Wang, S., & Bai, H. (2022). CO conversion over LaFeO3 perovskite during chemical looping processes: Influences of Ca-doping and oxygen species. *Applied Catalysis B: Environmental*, *316*, 121598. https://doi.org/https://doi.org/10.1016/j.apcatb.2022.121598

Sun, R., Xiao, Y., Yan, J., Shen, L., & Bai, H. (2022). Mechanism study on the high-performance BaFe2O4 during chemical looping gasification. *Fuel*, *307*, 121847. https://doi.org/https://doi.org/10.1016/j.fuel.2021.121847

Sun, Z., Chen, S., Russell, C. K., Hu, J., Rony, A. H., Tan, G., Chen, A., Duan, L., Boman, J., Tang, J., Chien, T., Fan, M., & Xiang, W. (2018). Improvement of H2-rich gas production with tar abatement from pine wood conversion over bi-functional Ca2Fe2O5 catalyst: Investigation of inner-looping redox reaction and promoting mechanisms. *APPLIED ENERGY*, *212*, 931-943. https://doi.org/https://doi.org/10.1016/j.apenergy.2017.12.087

Szuromi, P., & Grocholski, B. (2017). Natural and engineered perovskites. *Science*, *358*(6364), 732-733. https://doi.org/doi:10.1126/science.358.6364.732

Tan, K. W., Moore, D. T., Saliba, M., Sai, H., Estroff, L. A., Hanrath, T., Snaith, H. J., & Wiesner, U. (2014). Thermally Induced Structural Evolution and Performance of Mesoporous Block Copolymer-Directed Alumina Perovskite Solar Cells. *ACS Nano*, *8*(5), 4730-4739. https://doi.org/10.1021/nn500526t

Tenri Ola, A. T., Rahmat, R., Fahri, A. N., Heryanto, H., Mutmainna, I., Sesa, E., & Tahir, D. (2022). Synergistic Effect of Chitosan and Activated Carbon (AC) in Suppressing Recombination Charge of Composite Ca2Fe2O5−AC/Chitosan for High Photodegradation of Fipronil Wastewater. *Journal of Polymers and the Environment*, *30*(8), 3218-3229. https://doi.org/10.1007/s10924-022-02425-1

Vadivel, S., Maruthamani, D., Habibi-Yangjeh, A., Paul, B., Dhar, S. S., & Selvam, K. (2016). Facile synthesis of novel CaFe2O4/g-C3N4 nanocomposites for degradation of methylene blue under visible-light irradiation. *Journal of Colloid and Interface Science*, *480*, 126-136. https://doi.org/https://doi.org/10.1016/j.jcis.2016.07.012

Vries, M., McLaughlin, A., & Bos, J. W. (2010). Valence Bond Glass on an fcc Lattice in the Double Perovskite Ba2YMoO6. *Physical review letters*, *104*, 177202. https://doi.org/10.1103/PhysRevLett.104.177202

Wang, F., Chen, S., Chen, S., Du, J., Duan, L., & Xiang, W. (2023). Double adjustment of Ni and Co in CeO2/La2Ni2-xCoxO6 double perovskite type oxygen carriers for chemical looping steam methane reforming. *Chemical Engineering Journal*, *465*, 143041. https://doi.org/https://doi.org/10.1016/j.cej.2023.143041

Wang, N., Yu, X., Wang, Y., Chu, W., & Liu, M. (2013). A comparison study on methane dry reforming with carbon dioxide over LaNiO3 perovskite catalysts supported on mesoporous SBA-15, MCM-41 and silica carrier. *Catalysis Today*, *212*, 98-107. https://doi.org/https://doi.org/10.1016/j.cattod.2012.07.022

Wang, P., Xu, P., & Shen, L. (2023). Promotional effect of Ca on La1-xCaxFeO3 perovskites for ammonia production via steam catalytic gasification of microalgae. *Chemical Engineering Journal*, *455*, 140483. https://doi.org/https://doi.org/10.1016/j.cej.2022.140483

Wang, P., Yan, J., Wang, S., Xu, P., Shen, L., & Song, T. (2021). Synergistic effects of lanthanum ferrite perovskite and hydrogen to promote ammonia production during microalgae catalytic pyrolysis process. *Bioresource Technology*, *340*, 125641. https://doi.org/https://doi.org/10.1016/j.biortech.2021.125641

Wang, X., Abanades, S., Chuayboon, S., Zhang, J., & Wei, J. (2022). Solar-driven chemical looping reforming of methane over SrFeO3-δ-Ca0.5Mn0.5O nanocomposite foam. *International Journal of Hydrogen Energy*, *47*(79), 33664-33676. https://doi.org/https://doi.org/10.1016/j.ijhydene.2022.07.241

Wang, Y., Niu, P., & Zhao, H. (2019). Chemical looping gasification of coal using calcium ferrites as oxygen carrier. *Fuel Processing Technology*, *192*, 75-86. https://doi.org/https://doi.org/10.1016/j.fuproc.2019.04.009

Whitfield, P. S., Herron, N., Guise, W. E., Page, K., Cheng, Y. Q., Milas, I., & Crawford, M. K. (2016). Structures, Phase Transitions and Tricritical Behavior of the Hybrid Perovskite Methyl Ammonium Lead Iodide. *Scientific Reports*, *6*(1), 35685. https://doi.org/10.1038/srep35685

Xu, T., Wang, X., Zhao, H., Xiao, B., Liu, D., & Liu, W. (2023). Modulating lattice oxygen activity of Ca2Fe2O5 brownmillerite for the co-production of syngas and high purity hydrogen via chemical looping steam reforming of toluene. *Applied Catalysis B: Environmental*, *320*, 122010. https://doi.org/https://doi.org/10.1016/j.apcatb.2022.122010

Yan, J., Jiang, S., Song, T., & Shen, L. (2021). Chemical looping catalytic steam gasification (CLCSG) of algae over La1-xBaxFeO3 perovskites for syngas production. *Biomass and Bioenergy*, *151*, 106154. https://doi.org/https://doi.org/10.1016/j.biombioe.2021.106154

Yan, J., Lai, J., Yin, K., Yan, Y., Shen, L., & Yang, L. (2023). Syngas production and gas-N evolution over heterogeneously doped La-Fe-O perovskite-type oxygen carriers in chemical looping gasification of microalgae. *Bioresource Technology*, *369*, 128507. https://doi.org/https://doi.org/10.1016/j.biortech.2022.128507

Yan, J., Sun, R., Shen, L., Bai, H., Jiang, S., Xiao, Y., & Song, T. (2020). Hydrogen-rich syngas production with tar elimination via biomass chemical looping gasification (BCLG) using BaFe2O4/Al2O3 as oxygen carrier. *Chemical Engineering Journal*, *387*, 124107. https://doi.org/https://doi.org/10.1016/j.cej.2020.124107

Yang, E.-h., Noh, Y.-s., Ramesh, S., Lim, S. S., & Moon, D. J. (2015). The effect of promoters in La0.9M0.1Ni0.5Fe0.5O3 (M=Sr, Ca) perovskite catalysts on dry reforming of methane. *Fuel Processing Technology*, *134*, 404-413. https://doi.org/https://doi.org/10.1016/j.fuproc.2015.02.023

Yang, J., Bjørgum, E., Chang, H., Zhu, K.-K., Sui, Z.-J., Zhou, X.-G., Holmen, A., Zhu, Y.-A., & Chen, D. (2022). On the ensemble requirement of fully selective chemical looping methane partial

oxidation over La-Fe-based perovskites. *Applied Catalysis B: Environmental*, *301*, 120788. https://doi.org/https://doi.org/10.1016/j.apcatb.2021.120788
Yang, J., Na, Y., Hu, Y., Zhu, P., Meng, F., Guo, Q., Yang, Z., Qu, W., & Li, H. (2023). Granulation of Mn-based perovskite adsorbent for cyclic Hg0 capture from coal combustion flue gas. *Chemical Engineering Journal*, *459*, 141679. https://doi.org/https://doi.org/10.1016/j.cej.2023.141679
Yang, Q., Chen, L., Jin, N., Zhu, Y., He, J., Zhao, P., Huang, C., Wei, L., Ma, X., & Wang, X. (2023). Boosted carbon resistance of ceria-hexaaluminate by in-situ formed CeFexAl1−xO3 as oxygen pool for chemical looping dry reforming of methane. *Applied Catalysis B: Environmental*, *330*, 122636. https://doi.org/https://doi.org/10.1016/j.apcatb.2023.122636
Yang, Z., Zheng, Y., Li, K., Wang, Y., Wang, Y., Wang, H., Wang, Y., Jiang, L., Zhu, X., & Wei, Y. (2021). Chemical-looping reforming of methane over La-Mn-Fe-O oxygen carriers: Effect of calcination temperature. *Chemical Engineering Science*, *229*, 116085. https://doi.org/https://doi.org/10.1016/j.ces.2020.116085
Yin, W.-J., Weng, B., Ge, J., Sun, Q., Li, Z., & Yan, Y. (2019). Oxide perovskites, double perovskites and derivatives for electrocatalysis, photocatalysis, and photovoltaics [10.1039/C8EE01574K]. *Energy & Environmental Science*, *12*(2), 442-462. https://doi.org/10.1039/C8EE01574K
Yin, X., Shen, L., Wang, S., Wang, B., & Shen, C. (2022). Double adjustment of Co and Sr in LaMnO3+δ perovskite oxygen carriers for chemical looping steam methane reforming. *Applied Catalysis B: Environmental*, *301*, 120816. https://doi.org/https://doi.org/10.1016/j.apcatb.2021.120816
Yin, X., Wang, S., Sun, R., Jiang, S., & Shen, L. (2020). A Ce–Fe Oxygen Carrier with a Core–Shell Structure for Chemical Looping Steam Methane Reforming. *Industrial & Engineering Chemistry Research*, *59*(21), 9775-9786. https://doi.org/10.1021/acs.iecr.0c00055
Yin, X., Wang, S., Wang, B., & Shen, L. (2021a). Chemical looping steam methane reforming using Al doped LaMnO3+δ perovskites as oxygen carriers. *International Journal of Hydrogen Energy*, *46*(67), 33375-33387. https://doi.org/https://doi.org/10.1016/j.ijhydene.2021.07.192
Yin, X., Wang, S., Wang, B., & Shen, L. (2021b). Perovskite-type LaMn1−xBxO3+δ (B = Fe, CO and Ni) as oxygen carriers for chemical looping steam methane reforming. *Chemical Engineering Journal*, *422*, 128751. https://doi.org/https://doi.org/10.1016/j.cej.2021.128751
Zeng, L., Cheng, Z., Fan, J. A., Fan, L.-S., & Gong, J. (2018). Metal oxide redox chemistry for chemical looping processes. *Nature Reviews Chemistry*, *2*(11), 349-364. https://doi.org/10.1038/s41570-018-0046-2
Zhang, H.-X., Huang, Z.-Q., Yang, B., & Chang, C.-R. (2022). Theoretical insights into the oxygen supply performance of α-Fe2O3 in the chemical-looping reforming of methane. *Chemical Engineering Science*, *262*, 118041. https://doi.org/https://doi.org/10.1016/j.ces.2022.118041
Zhang, J., He, T., Wang, Z., Zhu, M., Zhang, K., Li, B., & Wu, J. (2017). The search of proper oxygen carriers for chemical looping partial oxidation of carbon. *Applied Energy*, *190*, 1119-1125. https://doi.org/https://doi.org/10.1016/j.apenergy.2017.01.024
Zhang, M., Du, Z., Zhang, Y., & Zhao, H. (2022). Progress of Perovskites as Electrodes for Symmetrical Solid Oxide Fuel Cells. *ACS Applied Energy Materials*, *5*(11), 13081-13095. https://doi.org/10.1021/acsaem.2c02149
Zhang, R., Cao, Y., Li, H., Zhao, Z., Zhao, K., & Jiang, L. (2020). The role of CuO modified La0·7Sr0·3FeO3 perovskite on intermediate-temperature partial oxidation of methane via chemical looping scheme. *International Journal of Hydrogen Energy*, *45*(7), 4073-4083. https://doi.org/https://doi.org/10.1016/j.ijhydene.2019.12.082
Zhang, R., Villanueva, A., Alamdari, H., & Kaliaguine, S. (2006). SCR of NO by propene over nanoscale LaMn1−xCuxO3 perovskites. *Applied Catalysis A: General*, *307*(1), 85-97. https://doi.org/https://doi.org/10.1016/j.apcata.2006.03.019
Zhao, K., Chen, J., Li, H., Zheng, A., & He, F. (2019). Effects of Co-substitution on the reactivity of double perovskite oxides LaSrFe2-xCoxO6 for the chemical-looping steam methane reforming.

Journal of the Energy Institute, *92*(3), 594-603. https://doi.org/https://doi.org/10.1016/j.joei.2018.03.013

Zhao, K., Fang, X., Cui, C., Kang, S., Zheng, A., & Zhao, Z. (2022). Co-production of syngas and H2 from chemical looping steam reforming of methane over anti-coking CeO2/La0.9Sr0.1Fe1−xNixO3 composite oxides. *Fuel*, *317*, 123455. https://doi.org/https://doi.org/10.1016/j.fuel.2022.123455

Zhao, K., He, F., Huang, Z., Wei, G., Zheng, A., Li, H., & Zhao, Z. (2016a). Perovskite-type oxides LaFe1−xCoxO3 for chemical looping steam methane reforming to syngas and hydrogen co-production. *Applied Energy*, *168*, 193-203. https://doi.org/https://doi.org/10.1016/j.apenergy.2016.01.052

Zhao, K., He, F., Huang, Z., Wei, G.-q., Zheng, A.-q., Li, H.-b., & Zhao, Z.-l. (2016b). CaO/MgO modified perovskite type oxides for chemical-looping steam reforming of methane. *Journal of Fuel Chemistry and Technology*, *44*(6), 680-688. https://doi.org/https://doi.org/10.1016/S1872-5813(16)30032-9

Zhao, K., He, F., Huang, Z., Zheng, A., Li, H., & Zhao, Z. (2014). Three-dimensionally ordered macroporous LaFeO3 perovskites for chemical-looping steam reforming of methane. *International Journal of Hydrogen Energy*, *39*(7), 3243-3252. https://doi.org/https://doi.org/10.1016/j.ijhydene.2013.12.046

Zhao, K., Li, L., Zheng, A., Huang, Z., He, F., Shen, Y., Wei, G., Li, H., & Zhao, Z. (2017). Synergistic improvements in stability and performance of the double perovskite-type oxides La2−xSrxFeCoO6 for chemical looping steam methane reforming. *APPLIED ENERGY*, *197*, 393-404. https://doi.org/https://doi.org/10.1016/j.apenergy.2017.04.049

Zhao, K., Shen, Y., He, F., Huang, Z., Wei, G., Zheng, A., Li, H., & Zhao, Z. (2016). Preparation of double perovskite-type oxide LaSrFeCoO6 for chemical looping steam methane reforming to produce syngas and hydrogen. *Journal of Rare Earths*, *34*(10), 1032-1041. https://doi.org/https://doi.org/10.1016/S1002-0721(16)60131-X

Zhao, K., Shen, Y., Huang, Z., He, F., Wei, G., Zheng, A., Li, H., & Zhao, Z. (2017). Different oxidation routes for lattice oxygen recovery of double-perovskite type oxides LaSrFeCoO6 as oxygen carriers for chemical looping steam methane reforming. *Journal of Energy Chemistry*, *26*(3), 501-509. https://doi.org/https://doi.org/10.1016/j.jechem.2016.11.016

Zhao, K., Zhang, R., Gao, Y., Lin, Y., Liu, A., Wang, X., Zheng, A., Huang, Z., & Zhao, Z. (2022). High syngas selectivity and near pure hydrogen production in perovskite oxygen carriers for chemical looping steam methane reforming. *Fuel Processing Technology*, *236*, 107398. https://doi.org/https://doi.org/10.1016/j.fuproc.2022.107398

Zhao, K., Zheng, A., Li, H., He, F., Huang, Z., Wei, G., Shen, Y., & Zhao, Z. (2017). Exploration of the mechanism of chemical looping steam methane reforming using double perovskite-type oxides La1.6Sr0.4FeCoO6. *Applied Catalysis B: Environmental*, *219*, 672-682. https://doi.org/https://doi.org/10.1016/j.apcatb.2017.08.027

Zhao, X., Zhou, H., Sikarwar, V. S., Zhao, M., Park, A.-H. A., Fennell, P. S., Shen, L., & Fan, L.-S. (2017). Biomass-based chemical looping technologies: the good, the bad and the future [10.1039/C6EE03718F]. *Energy & Environmental Science*, *10*(9), 1885-1910. https://doi.org/10.1039/C6EE03718F

Zheng, H., Jiang, X., Gao, Y., Tong, A., & Zeng, L. (2022). Chemical looping reforming: process fundamentals and oxygen carriers. *Discover Chemical Engineering*, *2*(1), 5. https://doi.org/10.1007/s43938-022-00012-3

Zheng, Y., Li, K., Wang, H., Tian, D., Wang, Y., Zhu, X., Wei, Y., Zheng, M., & Luo, Y. (2017). Designed oxygen carriers from macroporous LaFeO3 supported CeO2 for chemical-looping reforming of methane. *Applied Catalysis B: Environmental*, *202*, 51-63. https://doi.org/https://doi.org/10.1016/j.apcatb.2016.08.024

Zheng, Y., Zhao, L., Wang, Y., Wang, Y., Wang, H., Wang, Y., Jiang, L., Zhu, X., Wei, Y., & Li, K. (2021). Enhanced activity of La1-xMnCuxO3 perovskite oxides for chemical looping steam methane reforming. *Fuel Processing Technology*, *215*, 106744. https://doi.org/https://doi.org/10.1016/j.fuproc.2021.106744

Zhu, X., Li, K., Neal, L., & Li, F. (2018). Perovskites as Geo-inspired Oxygen Storage Materials for Chemical Looping and Three-Way Catalysis: A Perspective. *ACS Catalysis*, *8*(9), 8213-8236. https://doi.org/10.1021/acscatal.8b01973

Appendix A: Error Analysis

This table summarizes error analysis for CO_2, H_2, and CH_4 GC measurements. Each compound shows three replicate surface area measurements at various standard concentrations.

The analysis calculates key parameters to assess the precision of the GC analyses:

- Mean surface area: This represents the average surface area measured across the three replicates for each standard concentration.
- Standard deviation: This quantifies the spread of the replicate measurements around the mean, indicating how much individual measurements deviate from the average value.
- RSD (Relative Standard Deviation): This expresses the standard deviation as a percentage of the mean, allowing for easier comparison across different concentration levels and compounds.

Lower RSD values indicate higher precision, meaning the replicate measurements are closer to each other within a concentration level. For example, CO_2 shows the highest RSD across all concentrations (4.96% to 7.90%), suggesting slightly lower precision compared to H_2 (2.68% to 13.29%) and CH4 (3.13% to 6.22%).

	Standard	SA1	SA 2	SA 3	Mean SA	STDEV	RSD
	1.00	568.00	650.00	569.00	595.67	47.06	7.90
	15.00	13678.00	13049.00	14409.00	13712.00	680.64	4.96
CO2	50.00	38608.00	35647.00	34088.00	36114.33	2295.95	6.36
	99.90		93682.00	84617.00	89149.50	6409.92	7.19
H2	1.00	11398.00	11318.00	10466.00	11060.67	516.55	4.67

	50.00	512644.00	395461.00	488464.00	465523.00	61868.26	13.29
	99.90	1033052.00	1085498.00	1079081.00	1065877.00	28607.78	2.68
CO	1.00	656.00	687.00	613.00	652.00	37.16	5.70
	7.00	8166.00	7726.00	8588.00	8160.00	431.03	5.28
CH4	1.00	2290.00	2434.00	2335.00	2353.00	73.67	3.13
	4.50	15540.00	14983.00	16401.00	15641.33	714.41	4.57
	50.00	102413.00	95708.00	97984.00	98701.67	3409.62	3.45
	99.90	284464.00	320618.00	294653.00	299911.67	18641.84	6.22

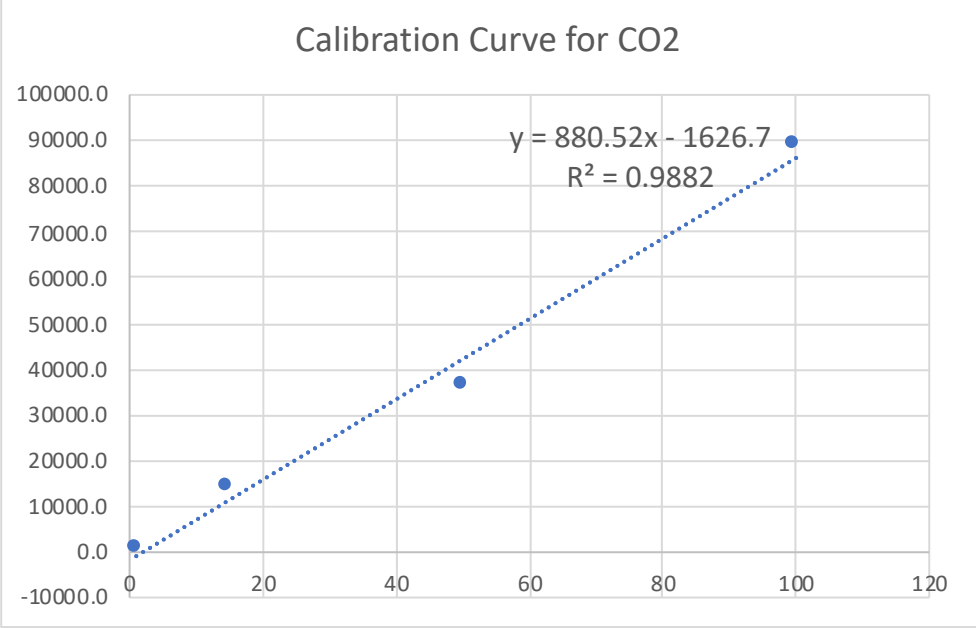

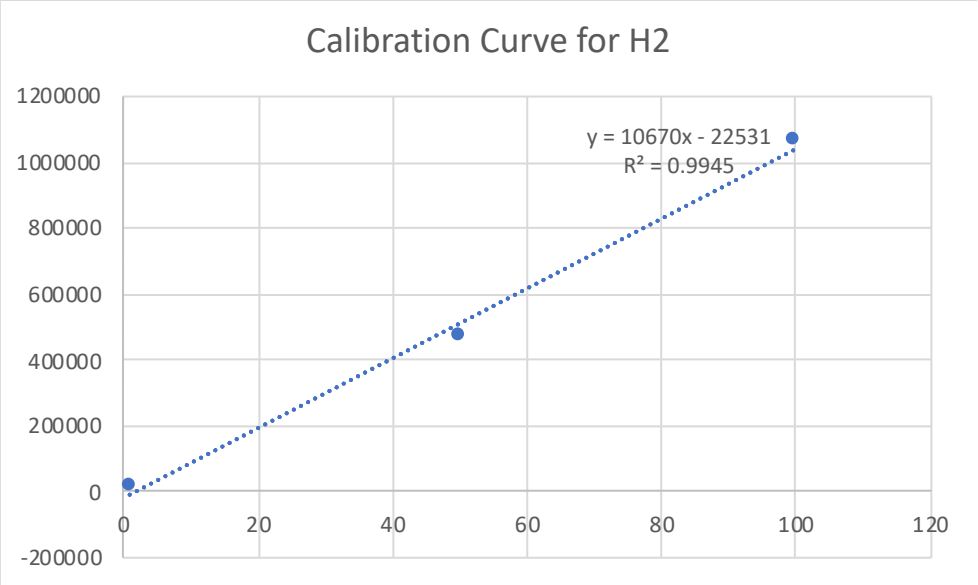
Calibration Curve for H2
y = 10670x - 22531
R² = 0.9945
1200000
1000000
800000
600000
400000
200000
0
-200000
0
20
40
60
80
100
120

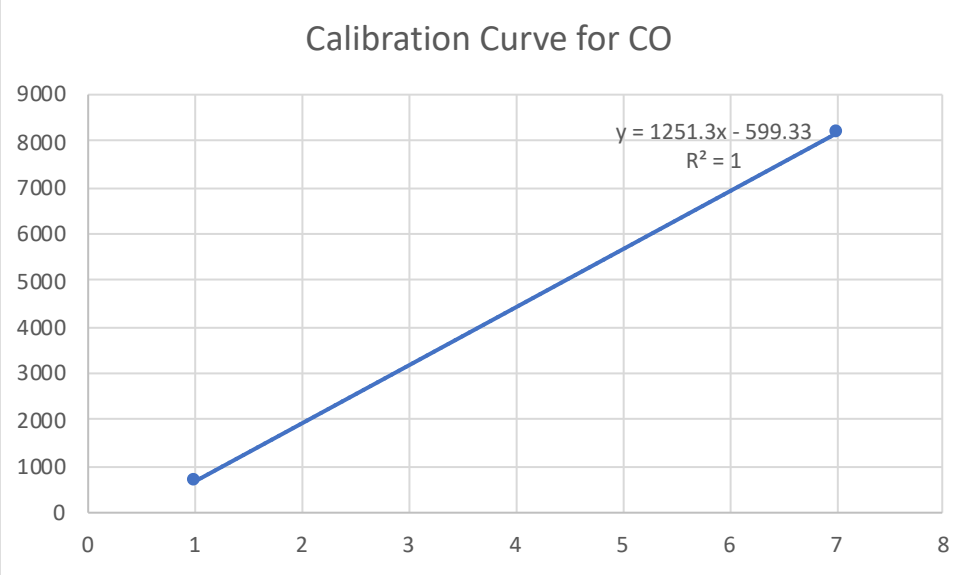
Calibration Curve for CO
y = 1251.3x - 599.33
R² = 1
9000
8000
7000
6000
5000
4000
3000
2000
1000
0
0
1
2
3
4
5
6
7
8

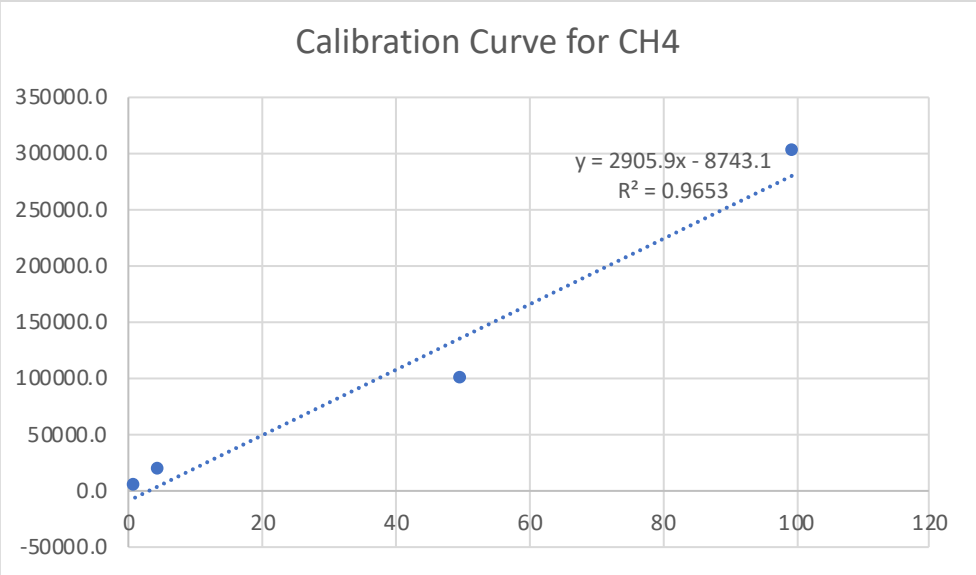
Calibration Curve for CH4
350000.0
300000.0
250000.0
200000.0
150000.0
100000.0
50000.0
0.0
-50000.0
0
20
40
60
80
100
120
y = 2905.9x - 8743.1
R² = 0.9653